Title
Time-dependent Characterization of Fluid Flow into the Intervertebral Disc

Permalink
https://escholarship.org/uc/item/8xd947t0

Author
Bezci, Semih Ege

Publication Date
2019

Time-dependent Characterization of Fluid Flow into the Intervertebral Disc

by

Semih Ege Bezci

A thesis submitted in partial satisfaction of the

requirements for the degree of

Doctor of Philosophy

in

Engineering – Mechanical Engineering

in the

Graduate Division

of the

University of California, Berkeley

Committee in charge:

Professor Grace D. O'Connell, Chair
Professor Lisa Pruitt
Professor Haiyan Huang

Fall 2019

Time-dependent Characterization of Fluid Flow into the
Intervertebral Disc

Abstract

Time-dependent Characterization of Fluid Flow into the
Intervertebral Disc

by

Semih Ege Bezci

Doctor of Philosophy in Engineering – Mechanical Engineering

University of California, Berkeley

Professor Grace D. O'Connell, Chair

The primary function of the intervertebral disc is to support large, multi-directional loads acting on the spine. The intervertebral disc has a heterogeneous structure, comprised of a gel-like nucleus pulposus (NP) and the annulus fibrosus (AF). The AF has a highly organized structure consisting of collagen fibers oriented in a criss-cross pattern in the alternating layers. Despite differences in composition and structure, water is the primary biochemical constituent of both tissues, accounting for greater than 65% of tissue's wet weight. The water content of the intervertebral disc fluctuates throughout the day as the magnitude of compressive stress acting on the spine varies with changes in body posture, muscle activity, and external loads. The disc loses water during the day and absorbs water at night when loads are reduced.

Due to the avascular nature of the intervertebral disc, cell viability and metabolism rely on the exchange of nutrients and metabolic by-products via diffusion under biochemical gradients and fluid flow modulated by diurnal loading patterns. Hence, investigating fluid flow kinematics under simulated physiological loading conditions is important for understanding healthy disc function and mechanobiology. However, there is a lack of knowledge of fluid flow behavior and recovery mechanics during low loading conditions when disc absorbs water and increases its height. Hence, this dissertation aims to fill in this gap in the literature by evaluating the time-dependent recovery mechanics and fluid flow kinematics of the healthy intervertebral disc during low loading conditions that simulate bed-rest. To achieve this, this study tested bovine bone-disc-bone motion segments under a series of creep and recovery loading conditions. Results showed that time-dependent disc recovery behavior has contributions from both inherent fluid-independent viscoelasticity and fluid-dependent poroelasticity. Intrinsic viscoelastic effects are present at short time scales, providing partial recovery of disc height within minutes of unloading before poroelastic effects come into play. Poroelastic fluid flow dominates recovery at long time scales and is largely driven by the osmotic differential between tissue and its surrounding environment.

In vitro biomechanical tests on disc joints monitor changes in disc height to understand the direction, magnitude, and rate of fluid flow through the disc. However, these studies report displacements for the entire bone-disc-bone joint without the ability to identify the region-specific changes during swelling due to fluid flow. To improve our understanding of the complex fluid redistribution within the disc, the second part of this work characterized the time-dependent swelling behavior of the intervertebral disc *ex situ.* The first experiment monitored time-dependent changes in tissue mass to compare differences in the swelling capacities of the NP and AF explants under free swelling conditions. NP explants experienced a higher swelling rate and equilibrium swelling capacity than AF explants. Specifically, there was a 200% increase in the NP tissue mass and a 70% increase in the AF tissue mass under free swelling conditions. The second experiment used an optical, non-contact measurement method to evaluate the distribution of swelling-induced strains throughout intact discs and AF rings. Axial deformations were fixed to prevent out-of-plane motion during swelling. The first group consisted of AF rings in contact with saline at the outer periphery and the center of the annular ring. The second group included AF rings in contact with saline solution only at the outer periphery. The third group included intact discs in contact with saline at the outer periphery. Tissue swelling due to fluid flow was observed to be a slow process that strongly depends on tissue-specific biochemical properties and physical boundary constraints. For AF rings, negative circumferential strains were observed in the inner AF, while positive circumferential strains were observed in the outer AF. However, restricting fluid flow only to the outer periphery during swelling reduced the swelling capacity of the inner AF. The largest absolute radial strain was observed to be in the outer AF for Group 1 and the outer AF for Group 2. The swelling capacity of the NP was largely reduced when swelling was restricted to occur only in the radial direction or constrained by the surrounding AF. Results from intact discs showed that NP pressurization during swelling reduces peak radial strains in the AF and results in uniform strain distribution throughout the AF.

Together these findings provide a better understanding of intervertebral disc mechanics and function, particularly during low loading periods when disc absorbs water and increases its volume due to swelling. In conclusion, fluid flow is a slow, time-dependent process that depends on many factors, including biochemical properties, external osmotic pressure, loading history, and boundary constraints.

Contents

List of Figures iii

List of Tables vii

Acknowledgements viii

1. Introduction 1

2. Background 3

  2.1. Intervertebral disc anatomy and structure 3

  2.2. Disc composition 4

  2.3. Mechanical function 5

  2.4. Disc degeneration 6

  2.5. Fluid flow 7

3. Radial variation in biochemical composition of the bovine caudal intervertebral disc 9

  3.1. Introduction 9

  3.2. Materials and Methods 10

    3.2.1. Sample preparation 10

    3.2.2. Biochemical analysis 10

    3.2.3. Swelling ratio 11

    3.2.4. Raman spectroscopy 12

    3.2.5. Differential scanning calorimetry analysis 12

    3.2.6. Multimodal nonlinear optical imaging 13

    3.2.7. Statistical analysis 14

  3.3. Results 14

    3.3.1. Traditional biochemical assays 14

    3.3.2. Swelling ratio 16

    3.3.3. Raman spectroscopy 16

    3.3.4. DSC analysis 19

    3.3.5. Multimodal nonlinear optical imaging 19

  3.4. Discussion 20

4. Osmotic pressure alters time-dependent recovery behavior of the intervertebral disc 24

  4.1. Introduction 24

4.2. Materials and methods 25
  4.2.1. Sample preparation 25
  4.2.2. Mechanical testing 26
  4.2.3. Data analysis 27
  4.2.4. Statistical analysis 27
4.3. Results 28
4.4. Discussion 31
5. Nonlinear stress-dependent recovery behavior of the intervertebral disc 34
5.1. Introduction 34
5.2. Materials and methods 35
  5.2.1. Sample preparation 35
  5.2.2. Mechanical testing 36
  5.2.3. Data analysis 37
  5.2.4. Statistics 38
5.3. Results 38
5.4. Discussion 41
5.5. Supplemental material 44
6. Time-dependent swelling behavior of the bovine caudal disc 45
6.1. Introduction 45
6.2. Materials and methods 46
  6.2.1. Free-swelling Experiment 46
  6.2.2. In-plane (2D) Swelling Experiment 47
  6.2.3. Water content analysis 49
    6.2.3.1. Gravimetric water content measurement 49
    6.2.3.2. Raman-based water content measurement 49
  6.2.4. Statistics 50
6.3. Results 50
  6.3.1. Free-swelling experiment 50
  6.3.2. In-plane (2D) Swelling Experiment 52
6.4. Discussion 55
7. Conclusions and future work 59
8. References 61

List of Figures

Figure 1: (A) Transverse section of adult human lumbar disc (level = L4-L5, age = 44, Thompson grade = 1) with the nucleus pulposus (NP) and the annulus fibrosus (AF) marked. (B) Schematic of the AF structure, showing alternating collagen fiber architecture.3

Figure 2: Schematic of (A) a proteoglycan aggregate and (B) collagen fiber architecture. The image showing the collagen fiber architecture was adapted from (Fratzl and Weinkamer, 2007). 4

Figure 3: Cross-section of healthy, moderately degenerate and severely degenerate human lumbar discs (from left to right). Donor ages for discs are 44, 71, and 78 years, respectively. 7

Figure 4: Schematic of sample preparation. A 4 mm cylindrical tissue was removed from the center of the disc (Layer 1). Then, concentric layers of equal thickness were obtained (Layers 2-10). A ~90 mg tissue strip was collected from each layer for analysis. 11

Figure 5: (A) Representative DSC curve. Negative heat flow values represent an endothermic response, while positive heat flow values represent an exothermic response. (B) Detail from dashed boxed in Figure 5A showing onset temperature of melting ($T_{m,onset}$), maximum temperature of melting ($T_{m,max}$), and latent heat of melting (ΔH_m), which was calculated as the area under the curve between -20 °C and +15 °C. 13

Figure 6: Radial distribution of water content normalized by (A) dry weight (DW) and (B) wet weight (WW). Radial distribution of sulfated GAG content normalized by (C) dry weight and (D) wet weight. Circles indicate individual data and red dashes indicate median values for each layer. NP and AF biochemical properties were compared using a Mann-Whitney U test on pooled data from Layers 1-4 (NP) and Layers 7-10 (AF; * represents $p < 0.05$). Differences in biochemical composition within each region (*i.e.*, shaded areas) were assessed using a Mann-Whitney U test with Bonferroni correction. Layers that do not share the same letter are significantly different ($p < 0.05$). 15

Figure 7: Radial distribution of water content normalized by sulfated GAG content. Circles indicate the individual data and red dashes indicate the median values. Values >100 in the last layer were omitted for clarity (n = 2 omitted values). NP and AF biochemical properties were compared using a Mann-Whitney U test on pooled data from Layers 1-4 (NP) and Layers 7-10 (AF; * represents $p < 0.05$). Differences in biochemical composition within each region (*i.e.*, shaded areas) were assessed using a Mann-Whitney U test with Bonferroni correction. Layers that do not share the same letter are significantly different ($p < 0.05$). .. 16

Figure 8: Radial distribution of collagen content normalized by (A) dry weight and (B) wet weight. Radial distribution of DNA content normalized by (C) dry weight and (D) wet weight. Circles indicate the individual data and red dashes indicate the median values. NP and AF biochemical properties were compared using a Mann-Whitney U test on pooled data from Layers 1-4 (NP) and Layers 7-10 (AF; * represents $p < 0.05$). Differences in biochemical composition within each region (*i.e.*, shaded areas) were assessed using a Mann-Whitney U test with Bonferroni correction. Layers that do not share the same letter are significantly different ($p < 0.05$). 17

Figure 9: Radial distribution of (A) swelling ratio, (B) s-GAGs leached into the swelling solution normalized by dry weight, (C) total s-GAG normalized by dry weight, and (D) leached s-GAG normalized by total s-GAG. Circles indicate individual data and red dashes indicate

median values. NP and AF biochemical properties were compared using a Mann-Whitney U test on pooled data from Layers 1-4 (NP) and Layers 7-10 (AF; * represents $p < 0.05$). Differences in biochemical composition within each region (*i.e.*, shaded areas) were assessed using a Mann-Whitney U test with Bonferroni correction. Layers that do not share the same letter are significantly different ($p < 0.05$).. 18

Figure 10: (A) Representative Raman spectra for nucleus pulposus (NP) and annulus fibrosus (AF) specimens. (B) Spectra from four regions within the disc to assess water content distribution, and (C) comparison of water-to-protein ratios collected from Raman spectroscopy (dark bars) and traditional biochemical analysis (light bars; two-way ANOVA – $p = 0.09$ for measurement method and $p = 0.001$ for disc region). Pairwise comparisons were performed using t-tests with Holm-Bonferroni correction. Layers that do not share the same letter are significantly different ($p < 0.05$). 18

Figure 11: (A) Bound water content normalized by total protein content, and (B) percentage of bound water content with respect to total water content. Circles indicate the individual data and black dashes indicate the median values. Changes in biochemical composition were determined by performing Kruskal-Wallis test followed by pairwise comparisons using Mann-Whitney U test with Bonferroni correction. Layers that do not share a letter are significantly different ($p < 0.05$)... 19

Figure 12: (A) Combined image from SHG (purple) and CARS (green, 2850 cm^{-1}) imaging. (B) Collagen content at the inner NP (i-NP), outer NP (o-NP), and inner AF (i-AF) normalized by collagen content of the outer AF (o-AF). Red circles represent SHG measurements, while black error bars represent mean ± standard deviation from the OHP assay. (C) Distribution of lipid droplet area throughout the disc obtained using the pooled data from the NP and AF. Data from lipids with areas greater than 20 mm^2 (~2%) are not shown for clarity. 20

Figure 13: (A) Samples were hydrated in a saline bath (0.15 M PBS) before testing. (B) Samples were tested under axial compression for 2 hours, followed by unloaded recovery for 12 hours. (C) Schematic of changes in disc height during. A reference disc height (dashed line) was defined as the maximum disc height recovered under hyperosmotic pressure (1.5 M PBS) and was used as a reference displacement. The difference between the reference displacement and final displacement after recovery was measured for the other experimental groups (blue line) (*i.e.*, 0.015 M, 0.15 M, and 0.75 M PBS). This difference in disc height recovery was used to estimate the osmotic condition that would result in elastic-only recovery behavior, and this osmotic condition was referred to as the balance concentration. 26

Figure 14: (A) Disc height change during recovery for a representative sample. Dashed vertical lines represent time points used to calculate "percent-recovery", which was defined as the displacement during recovery divided by the displacement during loading. (B) Percent-recovery after 4, 8, and 12 hours of recovery. The percent-recovery increased over time for the control group (0.15 M PBS; $p < 0.05$, black lines). *Represents differences between the osmotic loading group and the control.. 28

Figure 15: Disc height change from a representative sample. Circles represent experimental data, the grey line represents the model fit, and the dashed black line indicates equilibrium disc height. Inset – A small subset of specimens was allowed to recover for 48 hours, rather than 12 hours, to validate the predicted equilibrium time. 29

Figure 16: (A-B) Fast response and (C-D) slow response model parameters. τ represents the time constant, which is a function of the dashpot and spring stiffness in the Voigt models, and S_i represents the spring stiffness. *Represents $p \leq 0.05$ with respect to 0.15 M PBS control group. 29
Figure 17: (A) Equilibrium time (t_{eq}) for each osmotic group. (B) Percent recovery at equilibrium (t_{eq}). (C) Contributions of elastic, fast viscous and slow viscous responses shown as a percentage of the total recovery for each group. *Represents $p < 0.05$ with respect to 0.15 M PBS control group. 30
Figure 18: Balance concentration (red dot) for a representative sample. The balance concentration was defined as the x-intercept of a linear regression between the maximum disc height change during recovery and saline osmolarity (see Figure 14). 30
Figure 19: Schematic of experimental study design to evaluate (A) recovery behavior and (B) load-dependent recovery mechanics. Black arrows indicate compression applied to the motion segment. Blue arrows indicate expected fluid flow during each phase. 36
Figure 20: (A) Representative sample showing displacement during two cycles of creep and recovery. (B) Representative sample of axial displacement (or disc height) during recovery. Note that displacement was re-zeroed at the beginning of each loading period. Blue circles represent experimental data (every 50th point shown for clarity), the black line represents the model fit, and the dashed red line indicates equilibrium displacement. Recovery was measured for 18 hours, because preliminary work showed that 18-hour test was sufficient for predicting equilibrium displacement within 10 %. 39
Figure 21: (A) Comparison of experimental recovery data and model predictions for different stress levels. Circles represent experimental data, and curves represent model predictions. Recovery rates at the (B) beginning and (C) end of the recovery period. Recovery displacement (D) measured immediately after unloading (*i.e.* elastic recovery), (E) during the length of the recovery period (*i.e.,* time-dependent recovery displacement), and (F) predicted recovery displacement at equilibrium. Note that the equilibrium recovery displacement is a summation of the elastic and time-dependent recovery displacements. Circles represent experimental data and red lines indicate nonlinear best-fit lines. 39
Figure 22: (A-B) Asymptotic limits of displacement due to (A) fast and (B) slow recovery behaviors. (C-D) Time-constants associated with (C) fast and (D) slow recovery behavior. Circles represent experimental data and red lines indicate logarithmic or linear best-fit lines. 40
Figure 23: Percent contribution of (A) elastic, (B) fast, and (C) slow responses to equilibrium recovery displacement. Circles represent experimental data and red lines indicate linear best-fit lines. 41
Figure 24: Study design for (A) free (3D) and (B) in-plane (2D) swelling experiments. Blue arrows represent expected fluid flow due to contact from saline solution. 47
Figure 25: Schematic of experimental set-up for in-plane (2D) swelling experiments. A speckle pattern was applied to the top surface of the whole discs and AF rings before submerging them in saline for 16 hours. Disc height was fixed to avoid out-of-plane motion. 48
Figure 26: (A) AF (red) and NP (blue) swelling ratio throughout the 16-hour free swelling period. Shaded area represents the range (minimum to maximum) of experimental data. (B) Representative images of a swollen AF ring and intact disc. (C) Parameters for the stretched exponential function. Comparisons are made between the NP and the AF, and between the AF and whole disc. * Represents $p < 0.05$. Error bars represent one standard deviation. 51

Figure 27: Comparison of Raman specta pre- (dashed lines) and post-swelling (solid lines) for the nucleus pulposus (NP; red lines) and annulus fibrosus (AF; black lines). 51
Figure 28: Results for AF rings with fluid flow from the periphery and center. (A) Radial and (B) circumferential strains during the 16-hour swelling period shown for a representative test specimen. (C) Radial and (D) circumferential direction strains after 2, 8, and 16 hours of swelling (n = 8 per group). Red, green, and blue dots represent data for the inner (IAF), middle (MAF), and outer (OAF) annulus fibrosus, respectively. Black lines indicate mean values and dashed lines represent zero strain. 53
Figure 29: (A) Radial and (B) circumferential strain measurements for AF rings without fluid flow from the center. Data was collected throughout the 16 hour swelling period and analyzed at 2, 8 and 16 hours (n = 9 per group). Red, green and blue colors represent data from the inner (IAF), middle (MAF) and outer (OAF) annulus fibrosus, respectively. Black lines indicate the mean values, and the dashed line represents zero strain.......................... 54
Figure 30: (A) Radial and (B) circumferential strain measurements for intact discs. Data was collected throughout the 16 hour swelling period, and analyzed at 2, 8 and 16 hours (n = 8 per group). Red dots represent data from the nucleus pulposus (NP) and blue dots represents data from the annulus fibrosus (AF). Black lines indicate the mean values and the dashed line represents zero strain.. 54
Figure 31: Mean and standard deviation of pre- and post-swelling water content normalized by wet (left) and dry (right) weights. Pre-swelling measurements (green bars) represent data from our previous work (Bezci et al., 2019). Blue bars indicate the water content measurements for the AF rings with fluid flow from the center, and red bars represent water content measurements for the AF rings without fluid flow from the center. Yellow bars represent water content measurements for intact discs. * Represents $p < 0.05$. Error bars represent one standard deviation... 55

List of Tables

Table 1: NP and AF values from differential scanning calorimetry 20

Acknowledgements

I would like to thank my thesis advisor, Dr. Grace D. O'Connell, for her guidance and support throughout my graduate studies. This journey would not have been possible without her help. I would also like to express my gratitude and appreciation to the members of my thesis committee, Drs. Haiyan Huang and Lisa Pruitt for their great support and advice for my thesis. Dr. Haiyan Huang was one of my favorite professors in Statistics. Through her class, I had a much better understanding of experimental design and analysis. Dr. Lisa Pruitt has always been there for me when I needed advice from a faculty member. I have always looked up to her as a role model.

I feel fortunate to have collaborated with great scientists outside of my lab, including Katerina G. Mollari, Gabriel Dolhriac, Drs. Aaron Streets and Carlo Carraro. They have been very kind, patient, and helpful to me. Although we have been in two different branches of science, Katerina and I went through similar struggles, which formed the foundation of a friendship that will last a lifetime. I would also like to extend my special thanks to Carlo Carraro for his patience and support with Raman Spectroscopy. Our conversations made my time in his lab very fun. It was a great pleasure to have worked with him, and his feedback significantly improved the quality of my dissertation.

My hugs go to my friends at Berkeley Biomechanics Program for making the graduate school extremely fun. They were very supportive of me while I was sailing through the hardships of graduate school. I am very grateful for them, especially Saghi Sadoughi, Shannon Emerzian, Minhao Zhou, Nicole McMindes, Emily Lindberg, Nisha Subramanian, and Benjamin Werbner.

I have had the privilege of having amazing friends in my life. Feras el Zarwi has been a great friend and a mentor for me. He inspired me to follow my dreams and supported me emotionally on my rough journey to become a data scientist. Every time I was stressed out, I could hear him saying "Relaxxxxx!". Nick has been the best housemate I could ever ask for. He witnessed all my craziness at home, including my mock interviews with the bathroom mirror. Surprisingly, to this date, we are still roommates! I have been very lucky to have friends like Fazli Solak and Gamze Ucar, who always cared about me and wanted the best for me. They are definitely my guardian angels!

Most importantly, I owe this day to my family for their great support and unconditional love. This dissertation would be impossible without their sacrifices and motivation when I felt like my life was falling apart. I greatly appreciate how they have always been proud of me and supportive of my decisions.

1. Introduction

The primary function of the intervertebral disc is to support large, multi-directional loads acting on the spine. Activities of daily living cause diurnal variations in applied loads, which subsequently affect disc hydration (Kraemer, 1985; Malko et al., 2002, 1999; McMillan et al., 1996; Zhu et al., 2015). Discs lose water during the day due to mechanical loading and absorb water at night when loads are reduced. Due to the avascular nature of the intervertebral disc, cell viability and metabolism rely on the exchange of nutrients and metabolic by-products via diffusion under gradients set up by the cells' metabolic demands and fluid flow, which is modulated by diurnal loading patterns (Ferguson et al., 2004; Gullbrand et al., 2015; Urban et al., 1982; Yao and Gu, 2007). Hence, investigating fluid flow behavior under simulated physiological loading conditions is important for understanding healthy disc function and mechanobiology.

Disc degeneration is one of the most common sources of back pain, affecting almost 80% of the population by the age of 50 (Brinjikji et al., 2015). It is a multifactorial process with a cascade of changes occurring in disc structure, biochemistry, mechanics, and cellular metabolism; hence, it is often difficult to understand the etiology of disc degeneration (Adams and Roughley, 2006). Clinically, disc degeneration is commonly noted by the loss of disc height and hydration based on signal intensity of magnetic resonance images (Pfirrmann et al., 2001). While reduced hydration is a marker for disc degeneration, findings suggest that discs are at higher risk for herniation when fully or over-hydrated, such as early in the morning (Adams et al., 1987; Gunning et al., 2001). This observation is also supported by the increased risk of disc herniation reported for astronauts after returning from space, which is most likely due to excessive disc swelling under microgravity conditions (Johnston et al., 2010). The lack of understanding of disc degeneration etiology has hindered the development of biological repair strategies and has motivated experimental studies that are directed towards a better understanding of disc function and mechanics.

Spinal fusion surgery is the most commonly performed procedure for patients with severe back pain. However, it often includes complications, including higher rates of degeneration in the superior disc, due to increased loading following surgery (Chow et al., 1996; Ha et al., 1993; Lee, 1988; Lehmann et al., 1987; Nagata et al., 1993; Schlegel et al., 1996). This has led to new research aiming to develop tissue-engineered replacement discs that can mimic the characteristic function of a normal disc, including its time-dependent mechanical response under physiological loads. The time-dependent behavior of the intervertebral disc is predominantly associated with load-induced fluid flow (Costi et al., 2008; Vergroesen et al., 2018). However, there is a lack of knowledge of fluid flow behavior during low loading conditions, such as bed rest recovery. Hence, this dissertation aims to fill in this gap in the literature by studying fluid flow kinematics with controlled laboratory experiments.

The overall goal of this study was to evaluate the time-dependent fluid flow behavior of the healthy intervertebral disc under low loading conditions that simulate bed-rest. Chapter 2 will provide background information about disc structure and composition in healthy and degenerate human discs. For experiments described in Chapters 3-6, bovine caudal disc was used as an animal analog for the healthy human disc because of its large disc volume (area and height), increased availability, and similarities to healthy human discs in biomechanical and biochemical properties (Beckstein et al., 2008; Bezci et al., 2018b; O'Connell et al., 2007b; Showalter et al., 2012). Chapter 3 will explore the radial variation in the composition of the bovine caudal discs. Both traditional and novel measurement techniques were employed to provide a more comprehensive assessment of spatial variations in bovine disc composition. Additionally, this chapter explores the potential use of multimodal imaging and spectroscopy as less destructive measurement tools for measuring disc composition.

Chapter 4 examines fluid flow kinematics during unloaded recovery. Osmotic loading was used to alter disc hydration without changing disc composition and applied external loading. This chapter will explore the relative contribution of two concurrent mechanisms to the time-dependent recovery mechanics of bovine caudal discs. Disc joints were allowed to recover in saline solution with different salt concentrations, and disc height recovery was quantified using a rheological model that is capable of describing the changes at early and late stages of recovery. Furthermore, the magnitude of loading on each disc varies throughout the day (Nachemson, 1981; Wilke et al., 1999). Hence, Chapter 5 evaluates the time-dependent recovery behavior of the intervertebral disc under a wide range of compressive loads to characterize the impact of loading history on recovery mechanics. Disc height increases as the disc absorbs water and swells during low loading periods. In Chapters 4 and 5, changes in disc height were monitored to understand the direction, magnitude, and rate of fluid flow through the disc. However, these studies report displacements for the entire bone-disc-bone joint without the ability to identify the local changes in the disc. To understand region-specific changes during re-hydration and recovery, Chapter 6 reports local tissue strains measured using Digital Image Correlation (DIC) technique, a non-contact optical measurement method (Palanca et al., 2016). In addition, Chapter 6 compares the swelling behavior of the intervertebral under different boundary conditions.

Collectively, these chapters provide a better understanding of intervertebral disc mechanics and function, particularly during low loading periods when fluid flows into the disc. Finally, Chapter 7 discusses general conclusions from this work and potential future studies related to disc hydration.

2. Background

2.1. Intervertebral disc anatomy and structure

The spine performs the mechanical function of providing structural support, stability, and mobility to the body (Frost et al., 2019). It consists of five regions, including the cervical, thoracic, lumbar, sacral, and coccyx from top to bottom. The top three regions are composed of alternating vertebrae and intervertebral discs, which are the soft avascular tissues that have a heterogeneous, cartilaginous structure. Discs make up one third of the spine's height, and their morphology and size vary along the spine (Urban and Roberts, 2003). Cervical discs have a semielliptical cross-sectional area in the transverse plane whereas lumbar discs are similar in shape to a kidney bean (Pooni et al., 1986). Additionally, disc size tends to increase from the cervical region to the lumbar region. The height and diameter of healthy discs in the lumbar region are approximately 7 – 10 mm and 30 – 40 mm, respectively (Frost et al., 2019; Hong et al., 2010; O'Connell et al., 2007b; Twomey and Taylor, 1985).

The primary components of the intervertebral disc are the nucleus pulposus (NP) and annulus fibrosus (AF; Figure 1A). The NP is a hydrated gelatinous material, which represents 30 – 50% of the disc volume and is circumferentially encapsulated by the AF (Iatridis et al., 2007; Newell et al., 2017; O'Connell et al., 2007b). The AF has a highly organized fiber-reinforced structure consisting of concentric lamellae (layers). The AF layers are comprised of alternating collagen fibers that are oriented at an average of ±30° from the transverse plane (Figure 1B) (Cassidy et al., 1989).

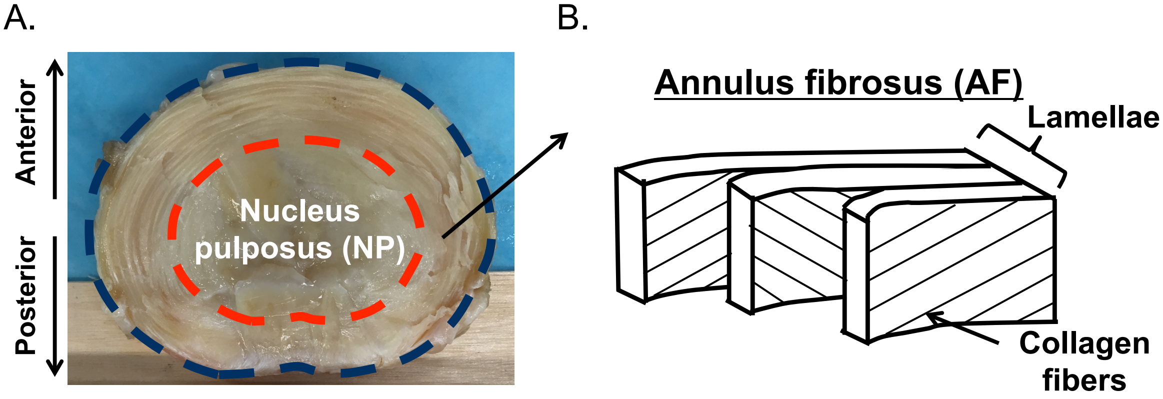

Figure 1: (A) Transverse section of adult human lumbar disc (level = L4-L5, age = 44, Thompson grade = 1) with the nucleus pulposus (NP) and the annulus fibrosus (AF) marked. (B) Schematic of the AF structure, showing alternating collagen fiber architecture.

While the NP is highly homogeneous and isotropic, a high spatial heterogeneity exists in the structure and anatomy of the AF (Holzapfel et al., 2005; Marchand and Ahmed, 1990). The AF is thinnest in the posterior region because of the fewer and more tightly packed collagen fibers (Galante, 1967; Inoue, 1981). In addition, lamellae thickness and collagen fiber angle follow a strong radial gradient (Cassidy et al., 1989). Specifically, lamellae thickness increases from the outer to the inner AF (i.e., 0.05 – 0.5 mm), while collagen fiber angle increases radially from ~30° in the outer AF to ~45° in the inner AF.

2.2. Disc composition

The extracellular matrix of the intervertebral disc is primarily composed of water, proteoglycans, and collagen; however, tissue composition varies spatially throughout the disc (Eyre and Muir, 1977). In healthy adult discs, water accounts for approximately 80 – 85% and 60 – 75% of the wet weight of the NP and AF, respectively (Antoniou et al., 1996; Jay Lipson and Muir, 1981). Similar to water content, proteoglycan content is highest in the NP (~50% of the dry weight) and decreases radially from the inner to the outer AF (~10 – 20%) (Antoniou et al., 1996). Collagen content follows a reverse spatial distribution, with collagen comprising of up to 50% of the dry weight in the AF and only 30% of the dry weight in the NP (Bezci et al., 2018a).

Proteoglycans are macromolecules consisting of a core protein with covalently attached glycosaminoglycan (GAG) side chains, such as keratan sulfate and chondroitin sulfate (Figure 2A). GAGs have fixed negatively charged carboxyl and sulfate groups, which attract positively charged inorganic ions, such as sodium and potassium, resulting in osmotic forces that attract water via osmosis (Urban and Roberts, 2003). The proteoglycans in the disc exist either as monomers or in large aggregates, which involve the associations of many proteoglycans with a single chain of hyaluronic acid, with the interactions stabilized by the presence of a link protein (Adams and Muir, 1976; Hardingham and Muir, 1972; Roughley et al., 2006; Stevens et al., 1979). The aggregates are mainly derived from aggrecan, which is the most abundant proteoglycan found in the intervertebral disc (Roughley et al., 2006). Other proteoglycans, such as decorin and biglycan, are also known to exist in the intervertebral disc, but they are smaller in size and not as well characterized as aggrecan (Johnstone and Bayliss, 1995; Melrose et al., 2001) .

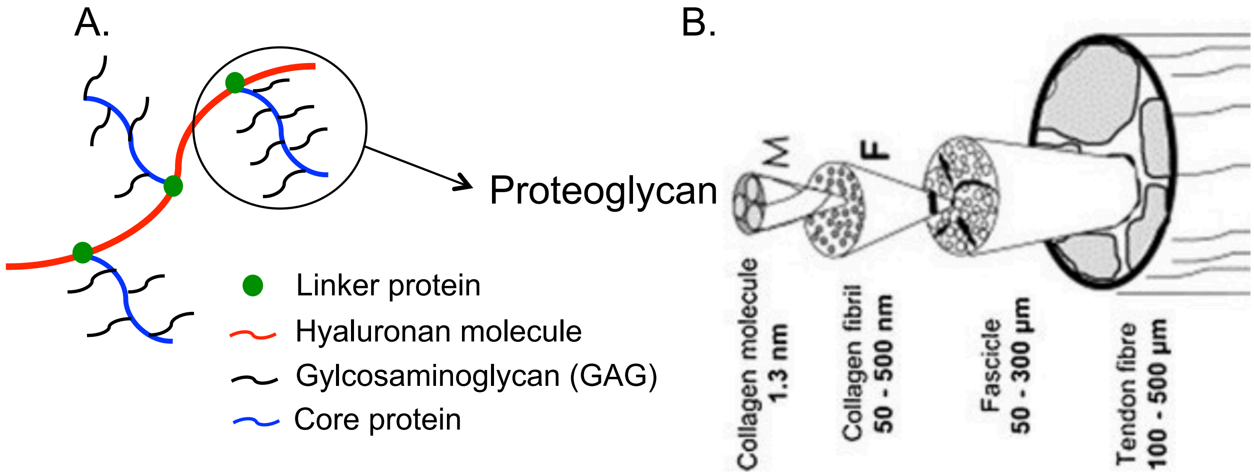

Figure 2: Schematic of (A) a proteoglycan aggregate and (B) collagen fiber architecture. The image showing the collagen fiber architecture was adapted from (Fratzl and Weinkamer, 2007).

Collagen fibers have a hierarchical structure, which provides structural stability to the biological tissues (Parenteau-Bareil et al., 2010). Collagen molecules are arranged in a triple-helix pattern to form individual fibrils, which then bundle to form collagen fibers (Figure 2B) (Shoulders and Raines, 2009). The majority of collagen in the intervertebral disc is collagen types I and II (Eyre and Muir, 1976). Type I collagen is most abundant in connective tissues that contain coarse fibers and experience high levels of tension, such as skin, bone, and tendon. Type II collagen is mostly found in tissues that are loaded in compression, such as cartilage. The amount of Types I and II collagen varies gradually across the disc, with Type II found almost exclusively in the NP and Type I at the outer edge of the AF (Eyre and Muir, 1977). Besides Types I and II collagen, intervertebral discs contain smaller amounts of other collagen types, including Types III, V, VI, IX, X, and XI (Ayad et al., 1982; Beard et al., 1981; Boos et al., 1997; Nerlich et al., 1997; Wu et al., 1987).

Other macromolecules, such as elastin and lipids, are also present in the intervertebral disc (Franklin and Hull, 1966; Mikawa et al., 1986). Their roles in disc mechanics and mechanobiology have not been as thoroughly investigated as collagen fibers and proteoglycans. There have been research efforts to understand the precise structural and mechanical roles of elastic fibers, which are composed of elastin (Michalek et al., 2009; Smith et al., 2008; Yu et al., 2007, 2002). The elastic fiber density was found to be significantly higher in disc regions that experience high tensile strains, such as the outer AF (Smith and Fazzalari, 2006). In addition, elastic fibers were observed in inter-lamellar space, suggesting a mechanical role both in maintaining the structural integrity of collagen fibers and in the recovery of the lamellar organization after loading (Yu et al., 2007, 2002).

2.3. Mechanical function

The complex structure of the spine allows it to undergo complex, three-dimensional motions during the activities of normal daily life, involving axial compression, tension, bending, and rotation. The primary loading modality on the intervertebral disc is axial compression, but loading on the disc fluctuates throughout the day (Kraemer, 1985; Malko et al., 2002, 1999; McMillan et al., 1996). The compressive stresses on the intervertebral disc range from 0.1 – 2.3 MPa, depending on the body posture and the activity (Nachemson, 1981; Wilke et al., 1999). That is, stresses are low (~0.1 – 0.2 MPa) when laying down, such as in bed rest; moderate (~0.50 MPa) when standing or sitting; and high (>0.5 MPa) while performing motions that involve lifting heavy objects or coupled loads (e.g. compression and bending). The physiological loading on the spine includes both short-term (e.g. flexion and extension) and long-term loads (e.g. sitting and standing). These loads can also be static or dynamic, applied at different rates. Biomechanical tests often use bone-disc-bone motion segments to evaluate the mechanical function of the intervertebral disc under simulated physiological loading conditions.

The mechanical behavior of the intervertebral disc has been extensively evaluated in compression, as the disc is a major compression-carrying component. Differences in the structure and composition of the NP and the AF grant them different functional roles under compression. The NP plays a critical role in supporting the intervertebral disc under low stresses, while the alternating fiber-reinforced structure of the AF is ideal for withstanding large and complex loads (Cannella et al., 2008). Axial compression causes a decrease in disc height and an increase in intradiscal pressure (Botsford et al., 1994; Malko et al., 1999; Nachemson, 1963; Sato et al., 1999). During compression, the NP behaves like a pressurized fluid, transferring forces vertically to the endplate and radially to the AF. Due to the NP pressurization, the AF experiences both radial compressive and circumferential (or hoop) tensile stresses (O’Connell et al., 2007a). This load transfer and uncrimping of collagen fibers at higher loads have been associated with the nonlinearity observed in disc compressive mechanics.

Along with compression, intervertebral discs experience large bending and torsional loads during activities of daily living. Magnetic resonance imaging has shown that healthy lumbar discs experience up to 6^{o} of torsion *in vivo*, with the amount of rotation increasing towards the sacrum (Haughton et al., 2002; Ochia et al., 2006). The applied loads are shared among the intervertebral discs and facet joints, which are the diarthrodial joints posterior to the vertebral column (Gellhorn et al., 2013). While the contribution of facet joints to compressive mechanics is small (~10%), they can contribute to 40 – 65% of the shear forces in healthy and degenerate discs (Bezci et al., 2018a; Farfan et al., 1970; Zimmerman et al., 1992). Disc torsion mechanics strongly depend on the magnitude of compressive loading (Bezci et al., 2018b, 2018a; Gardner-Morse and Stokes, 2003). Hence, evaluating mechanical properties under different compressive stresses is highly important for a broad understanding of intervertebral disc function and mechanics.

2.4. Disc degeneration

Back pain is a major public health concern and has been strongly associated with degeneration of the intervertebral disc (Luoma et al., 2000). Disc degeneration has a complex multifactorial etiology and involves irreversible changes in disc structure, morphology, biochemistry, and function. These changes are often associated with altered disc mechanics and mechanical instability, which in turn impact the progression of the degenerative disease (Galbusera et al., 2014; Sengupta and Fan, 2014; Stokes and Iatridis, 2004).

The degenerative process can be associated with different morphological changes in the intervertebral and the adjacent structures, including the facet joints (Vernon-roberts and Pirie, 1977). Macroscopic changes include disc height loss, tissue dehydration, irregular lamellae structure, formation of fissures in the AF, and an increase in the osteophytes on the vertebral bodies (Figure 3) (Boos et al., 2002; Haefeli et al., 2006; Murata et al., 1994; Thompson et al., 1990). With degeneration, the NP becomes more fibrotic and less gel-like, while the AF becomes more disorganized (Figure 3) (Haefeli et al., 2006). Due to morphological changes in the NP, the boundary between the NP and the AF also becomes less obvious.

The earliest and most marked biochemical change with disc degeneration is loss of proteoglycans (Lyons et al., 1981). During disc degeneration, proteoglycans break down and small fragments can leach from the tissue, causing a decrease in osmotic pressure and the ability of the intervertebral to maintain its hydration (Raj, 2008; Urban and Roberts, 2003). Consequently, degenerated discs have lower water content than normal discs, and they lose disc height and fluid more rapidly under compression (Keller et al., 1987; Pearce et al., 1987).

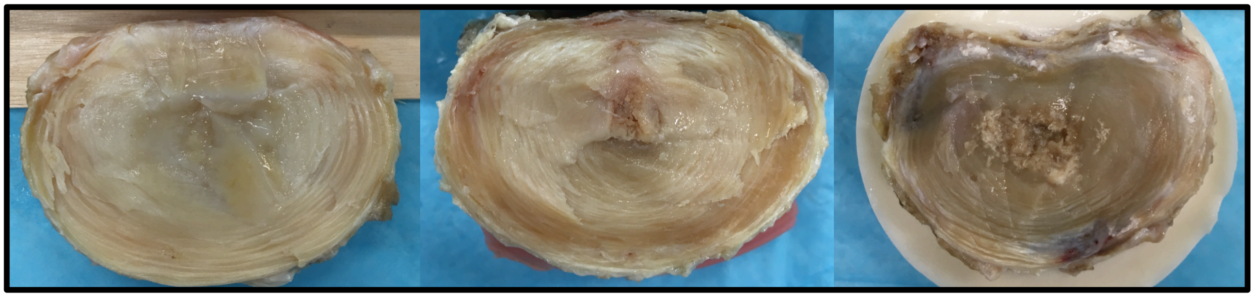

Figure 3: Cross-section of healthy, moderately degenerate and severely degenerate human lumbar discs (from left to right). Donor ages for discs are 44, 71, and 78 years, respectively.

Degeneration can cause abnormal loading within the disc and in the surrounding spinal structures (Adams et al., 1996; Park et al., 2015; Rohlmann et al., 2006; Tsantrizos et al., 2005). With disc degeneration, stress distributions within the disc become anisotropic and asymmetric, causing stress concentrations along the endplate or within the AF, which might predispose them to failure and injuries (McNally and Adams, 1992; Park et al., 2015; Rohlmann et al., 2006; Tsantrizos et al., 2005). In addition, contact forces in facet joints increase due to a decrease in disc height and altered disc mechanics with disc degeneration (Rohlmann et al., 2006). Because of the increased loads on the facet joints, they are prone to degenerate in parallel with the intervertebral disc (Fujiwara et al., 1999).

2.5. Fluid flow

Disc water content fluctuates daily due to changes in applied external loads (Malko et al., 2002; Zhu et al., 2015). That is, the intervertebral disc loses water due to high compressive loads applied during the day, whereas it reabsorbs water during low loading periods, such as bed rest. These *in vivo* observations have been replicated *in vitro* by testing motion segments in a physiological saline bath under a series of creep and recovery loading (MacLean et al., 2007; O'Connell et al., 2011; Schmidt et al., 2016a). These studies used disc height change as an indirect measure of fluid flow through the disc. Fluctuations in water content were found to alter disc height and mechanics, including stiffness, range of motion, and energy absorption (Bezci et al., 2015; Costi et al., 2002; Schmidt et al., 2016b).

Observed differences in disc mechanics during creep and recovery can be attributed to the differences in the underlying mechanisms during the two loading conditions. Fluid flow out of the disc during creep occurs through mechanical loading, like water being squeezed out of a sponge. The negatively charged sulfate and carboxyl groups in GAGs give rise to a high charge density within the tissue, which is commonly referred in the literature as the fixed charge density (Lu and Mow, 2008). Fluid flow out of the disc during loading increases the fixed charge density and internal osmotic pressure, causing a pressure gradient between the internal and external tissue environments (Gray et al., 1988). This osmotic pressure gradient is considered to be the driving force for fluid flow into the disc during recovery. However, the osmotic environment of the disc *in vivo* is not well known.

There is a discrepancy reported for the flow-dependent recovery behavior between *in vivo* and *in vitro* studies. While *in vivo* studies have observed complete recovery of disc height and water content upon unloading, many *in vitro* studies have reported incomplete disc height recovery within a time scale comparable to *in vivo* conditions (approximately 16 hours of loading and 8 hours of recovery) (Botsford et al., 1994; O'Connell et al., 2011; Reitmaier et al., 2012; Vergroesen et al., 2014). Despite discrepancies between *in vivo* and *in vitro* studies, *in vitro* studies are helpful to determine the effect of different factors (e.g. preload and disc hydration) on disc mechanics separately without confounding effects of multiple variants (Velísková et al., 2018).

3. Radial variation in biochemical composition of the bovine caudal intervertebral disc[1]

3.1. Introduction

Animal discs have been widely adapted to study relationships between intervertebral disc structure and function. In particular, bovine caudal discs have been excellent models for studying biomechanical behavior of healthy discs, because of increased tissue availability and larger disc size (O'Connell et al., 2007b). Despite some morphological differences, such as increased circularity, bovine discs exhibit biochemical and mechanical properties similar to healthy human discs (Beckstein et al., 2008; Bezci et al., 2018b; Demers et al., 2004; Showalter et al., 2012). Biochemically, bovine discs have similar water, proteoglycan, and collagen contents as young, healthy human discs. Mechanically, compressive and torsional properties of bovine caudal discs are comparable to human discs after accounting for differences in disc geometry (Beckstein et al., 2008; Showalter et al., 2012). Moreover, the quantity of notochordal cells in human and bovine discs declines rapidly with age, an observation not seen in smaller animals (*e.g.* rat, pig, cat, and rabbit) (McCann and Séguin, 2016).

Various analytical techniques have been used to characterize biological tissue structure and composition. Traditional techniques include spectrophotometric assays of tissue digests and immunohistochemical staining of fixed tissues (Boos et al., 2002; Farndale et al., 1982; Pattappa et al., 2012; Reddy and Enwemeka, 1996; Roberts et al., 2006). More recently, alternative imaging and spectroscopy techniques have garnered significant interest, due to less destructive protocols (Campagnola et al., 2002; Cheng and Xie, 2004). Such techniques include nonlinear optical imaging, such as Coherent anti-Stokes Raman spectroscopy (CARS) and second-harmonic generation (SHG) imaging (Reiser et al., 2007; Rodriguez et al., 2006). The combined use of CARS and SHG provides simultaneous, high-resolution images of collagen fibers and lipids (Evans et al., 2005). However, each measurement method has its own advantages and limitations; as such, a rigorous compositional analysis should apply a variety of analytical techniques.

It has long been known that biochemical and mechanical properties vary greatly throughout the human intervertebral disc (Antoniou et al., 1996; Holzapfel et al., 2005; Iatridis et al., 2007; Skaggs et al., 1994). However, comparisons are largely drawn between the nucleus pulposus (NP) and the annulus fibrosus (AF) or through the thickness of the AF. Work by Iatridis *et al.* highlighted spatial variations in biochemical composition of mild to moderately degenerate human discs (Iatridis et al., 2007). Specifically, a linear decrease in water and proteoglycan content was observed from the inner AF to the outer AF, and NP was reported as being more heterogeneous than previously thought. Similar analyses have been performed to quantify the spatial variation in bovine disc composition; however, these analyses have been

---

[1] Previously published as "Bezci, S.E., Werbner, B., Zhou, M., Malollari, K.G., Dorlhiac, G., Carraro, C., Streets, A., O'Connell, G.D., 2019. Radial variation in biochemical composition of the bovine caudal intervertebral disc. JOR SPINE. https://doi.org/10.1002/jsp2.1065"

limited in either spatial resolution or quantitative power. That is, only large, discreet disc regions have been considered, such as comparing the NP with the AF or the inner AF with the outer AF (Beckstein et al., 2008; Demers et al., 2004; Showalter et al., 2012). Other studies observed radial variations in tissue composition with high spatial resolution using histology and immunohistochemistry, but these techniques were limited in their ability to provide absolute, quantitative values (Boos et al., 2002; Pattappa et al., 2012). More recently, Emanuel *et al.* reported variations in disc composition with high spatial resolution using Fourier-transform infrared imaging (FTIR), but this method only reports relative compositional changes in arbitrary units (Emanuel et al., 2018).

Despite the extensive use of bovine caudal discs in spine research, the radial variations in bovine disc composition have not yet been rigorously quantified with high spatial resolution. Thus, the first objective of this study was to provide absolute quantitative measurements of biochemical composition of bovine caudal discs with significantly increased spatial resolution using traditional biochemical techniques. The second objective was to quantify the spatial distribution of free and bound water content in the disc using Raman spectroscopy with differential scanning calorimetry. The final objective was to simultaneously image collagen fibers and lipid droplets throughout the disc using multi-modal imaging techniques (CARS and SHG).

3.2. Materials and Methods

3.2.1. Sample preparation

Fresh bovine caudal spine sections were acquired from a local butcher and stored at -20°C (20 spines, age = 18-24 months). Caudal spines were thawed at room temperature and surrounding musculature and ligaments were removed with a scalpel. Tails were then hydrated in 0.15 M phosphate-buffered saline solution (PBS) for 18 hours at 4°C to ensure that each specimen and spine experience similar hydration histories prior to performing biochemical analyses. Once hydrated, intervertebral discs were removed from the top two levels with a scalpel (n = 38, Levels C1-C3), wrapped in PBS-soaked gauze, and stored at -20°C for biochemical analyses.

3.2.2. Biochemical analysis

Ten discs were randomly chosen and used for traditional biochemical analyses. Discs were removed from the freezer and placed on a freezing stage microtome (-16°C) to prepare specimens of concentric rings (Figure 4). First, the average disc diameter was measured with digital calipers to estimate the approximate thickness of each layer (10 total layers). The first layer was taken from the center of the NP, as a solid cylinder, using a biopsy punch (4 mm diameter). Subsequent layers were removed as hollow cylinders with wall thickness of ~1 mm. For inner layers, biopsy punches with diameters of 6 to 10 mm were used to create concentric cylinders. Then, a scalpel was used to create concentric cylinders for the outer layers (diameter ~12-20 mm). Each hollow cylinder was cut and laid flat. Then, a rectangular tissue sample with a wet weight (WW) of approximately 90 mg was cut from the tissue strip (Figure 4). We assumed that bovine disc composition along the circumference was consistent. Samples were then freeze-dried in a lyophilizer for 48 hours and re-weighed to obtain dry tissue weight (DW). Water content was calculated as the difference between wet and dry weights divided by wet weight (*i.e.*, [WW – DW]/WW). Each freeze-dried sample was digested in 1 mL of 2 mg/mL proteinase-K solution at 56 °C for 24 hours.

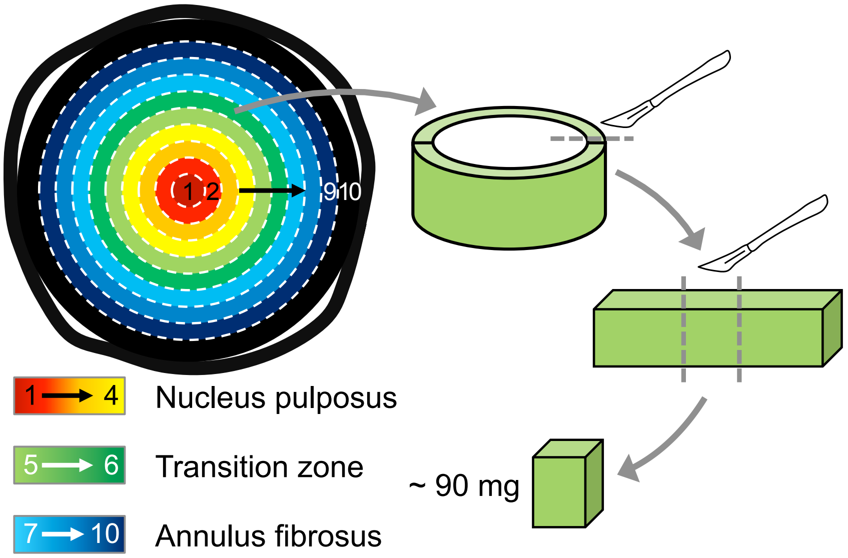

Figure 4: Schematic of sample preparation. A 4 mm cylindrical tissue was removed from the center of the disc (Layer 1). Then, concentric layers of equal thickness were obtained (Layers 2-10). A ~90 mg tissue strip was collected from each layer for analysis.

Proteinase-K tissue-digests were used to measure sulphated glycosaminoglycan (s-GAG), collagen, and DNA contents. s-GAG content was measured using the 1,9-dimethylene blue dye-binding (DMMB) assay (Farndale et al., 1986). Total collagen content was measured using the orthohydroxyproline (OHP) colorimetric assay and assuming a 1:7.5 OHP-to-collagen mass ratio (Hollander et al., 1994). DNA content was determined using the PicoGreen fluorescence assay (Molecular Probes, Eugene, Oregon). Collagen, s-GAG, and DNA measurements were normalized to wet and dry tissue weights to account for variations in initial tissue hydration and to compare results across data reported in the literature.

3.2.3. Swelling ratio

Eight additional discs were used to evaluate bovine disc swelling properties. Tissue samples were prepared and weighed as described above (*i.e.,* ~90 mg specimens). Each sample was immersed in 10.0 mL of 0.15 M PBS and allowed to freely swell for 16 hours at room temperature (~23^{o}C). After free swelling, samples were gently blotted and re-weighed to obtain the tissue's swollen weight (SW). The swelling ratio was calculated as the difference between the swollen weight and initial wet weight normalized by the initial wet weight (*i.e.*, [SW-WW]/WW). A 1 mL aliquot of swelling solution was saved to determine whether s-GAGs leached into the PBS solution during swelling. Swollen samples were digested using proteinase-

K, and s-GAG contents of tissue digests and swelling solutions were measured using the DMMB assay.

3.2.4. Raman spectroscopy

All Raman spectroscopic measurements were collected at room temperature (excitation at 632.8 nm; Horiba Jobin Yvon Labram spectrometer with Olympus BX41 confocal microscope). Spectra were recorded over a wide frequency range (0 – 3800 cm^{-1}) for points located in the NP and AF (n = 3 discs). Raman data were post-processed by performing a baseline correction using a piecewise linear fitting and smoothed using a Savitzky-Golay filter. To compare across different regions, spectra were normalized to have the same intensity signal at 2945 cm^{-1}, which corresponded to the strongest CH vibrational line. Representative spectra for the NP and the AF were obtained by averaging twelve spectra taken from each region. The low frequency region (< 300 cm^{-1}) was excluded from the spectra, due to the high signal intensity from the Rayleigh line (Gniadecka et al., 1998a).

A narrower range of spectra data (2700 – 3800 cm^{-1} range) was collected for 10 bovine discs to measure radial distribution of water-to-protein content. Measurements were taken at inner NP (i-NP), outer NP (o-NP), inner AF (i-AF), and outer AF (o-AF). Discs were freeze-dried for 72 hours, and measurements were repeated on dry discs to measure the decrease in water content associated with removal of free water molecules (Unal and Akkus, 2018). Specifically, water-to-protein content of wet and dry discs was determined by taking the ratio of integrated areas of OH and CH bands (3050 – 3800 cm^{-1} and 2800 – 3050 cm^{-1}, respectively), which is directly proportional to the relationship between water and protein/lipid molecules (Parkes et al., 2017). Raman-based water-to-protein ratios were compared to data collected from traditional biochemical analysis (*i.e.*, water content / (collagen + s-GAG content) with respect to the tissue's wet weight). The average of two adjacent layers from the biochemical analysis was used to estimate water-to-protein ratios for each region (*i.e.*, i-NP: layers 1-2, o-NP: layers 3-4, i-AF: layers 7-8, and o-AF: layers 9-10). The percentage of bound water with respect to total water content was estimated by comparing water-to-protein ratios from dry and wet samples.

3.2.5. Differential scanning calorimetry analysis

Differential Scanning Calorimetry (DSC) measurements were acquired on inner NP and outer AF tissue samples collected from seven bovine caudal discs (Mettler Toledo Model DSC 1, Star^{e} system). Specifically, wet tissue samples, 5 to 15 mg, were obtained with a scalpel and hermetically sealed in aluminum pans. Weights of tissue samples and sealed pans were measured before and after the test (NewClassic MS, Mettler Toledo; accuracy resolution = ±0.0001 mg). Prior to DSC measurements, pans were pierced to allow water evaporation during testing. Samples were cooled to -30°C and held at -30°C for 15 minutes to allow water in the tissue to freeze (heating/cooling rate = 10 °C/min). Then, the samples were heated to 180 °C, and dried at 180 °C for 30 minutes to determine mass lost during heating (m_{loss}; Figure 5A). Mass loss was reported as a percentage of initial tissue mass.

Crystallization temperature (T_c) was defined as the peak exothermic temperature (e.g.,

Figure 5 - peak near –10^{o}C). Crystallization enthalpy (ΔH_c) was calculated as the area under the exothermic peak. The onset temperature of melting ($T_{m,onset}$) was defined as the temperature at which the extrapolated baseline intersected with the tangent line of the linear region from the melting curve during endothermic reaction (Figure 5B – dashed red lines) (Roos, 1986). Maximum melting temperature ($T_{m,max}$) was defined as the peak temperature during melting. The latent heat of melting (ΔH_m) was calculated by finding the area under the melting peak (between temperatures –20 to +15 °C; Figure 5B – shaded area). The amount of freezable water was calculated by dividing the latent heat of melting (*i.e.,* ΔH_m) by the melting enthalpy of pure ice (330 J/g). The presence of a second endothermic phenomenon (temperatures > 60 °C) has been associated with collagen denaturation (Samouillan et al., 2011). The onset ($T_{d,onset}$) and maximum temperature ($T_{d,max}$) of the denaturation curve were determined using the methods described above for melting parameters.

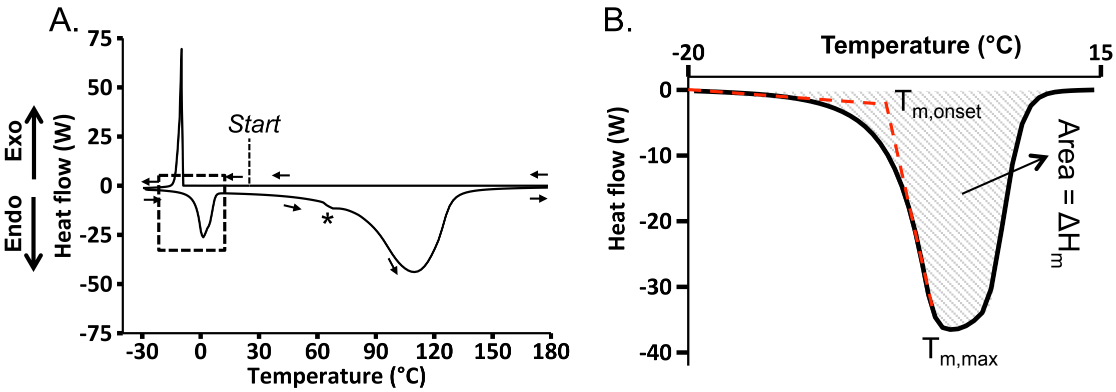

Figure 5: (A) Representative DSC curve. Negative heat flow values represent an endothermic response, while positive heat flow values represent an exothermic response. (B) Detail from dashed boxed in Figure 5A showing onset temperature of melting ($T_{m,onset}$), maximum temperature of melting ($T_{m,max}$), and latent heat of melting (ΔH_m), which was calculated as the area under the curve between -20 °C and +15 °C.

3.2.6. Multimodal nonlinear optical imaging

Collagen fibers and lipid droplets were simultaneously imaged using a multimodal CARS and Second Harmonic Generation (SHG) microscopy system. A femtosecond optical parametric oscillator (OPO), with dual output (Insight DS+, Spectra-Physics, Santa Clara, California) was used as the excitation source and coupled into the inverted laser-scanning microscope chassis (FV1200, Olympus, Waltham, MA). One output was tunable, and the other was fixed at 1040 nm. Imaging was performed using a 60x water immersion objective lens (UPLSAPO60XWIR, Olympus). Lipid droplets were imaged with CARS by tuning the pump beam to 802 nm, such that the beat frequency between the pump line and the fixed Stokes line at 1040 nm matched the CH_2 stretching vibration of ~2850 cm^{-1}. Collagen fibers were visualized using the SHG and sum-frequency generation (SFG) signals. Both signals were collected in the epi-direction and separated from the excitation lasers by a shortpass 690 nm dichroic mirror. The CARS and SHG/SFG signals were further separated by a shortpass 570 nm dichroic mirror, and both signals were collected simultaneously by two external photomultiplier tubes. The SHG signal comprised the combined contribution of the second harmonics of the pump and Stokes beams respectively, as well as their sum-frequency signal.

Bovine caudal discs (n = 3 discs from C1C2 or C2C3) were isolated from freshly acquired tails, and used for multimodal imaging. A mid-sagittal slice was cut from each disc and placed onto a glass coverslip (0.17 mm thickness) for imaging. Multiple images (image resolution: 212 x 212 μm) were collected on the same sample at inner NP (i-NP), outer NP (o-NP), inner AF (i-AF), and outer AF (o-AF). Two-color images were produced using Matlab (Mathworks, Inc.) to highlight collagen fibers (purple) and lipid droplets (green). The area and count of lipid droplets were estimated from 2D binary images using ImageJ. The relative change in SHG signal intensity was used as a marker for characterizing radial distribution of collagen in bovine discs. To quantify collagen content for each tissue region, the mean signal intensity was calculated and normalized by the applied voltage from the photomultiplier tube. Collagen content of the inner NP, outer NP, and inner AF were reported relative to collagen content of the outer AF.

3.2.7. Statistical analysis

All statistical analyses were performed in R (R Project for Statistical Computing, Vienna, Austria). Exploratory data analysis indicated the presence of non-normal distributions; hence, data were reported with median values, unless stated otherwise, and non-parametric statistical analyses were preferred over parametric analyses. Significance was assumed at $p < 0.05$ for all statistical analyses.

For traditional biochemical analyses, disc regions were defined a priori based on visual inspection of the NP and AF boundary, where layers 1 to 4 represented the NP, layers 5 to 6 were in the transition region between the NP and AF, and layers 7 to 10 represented the AF (Figure 4). The Kruskal-Wallis test, followed by Mann-Whitney U pairwise comparison tests, was conducted to determine within-region differences in properties. Pairwise comparisons were only conducted to detect differences within each tissue region (*i.e.,* within NP or AF layers). Additionally, a Mann-Whitney U test was performed to compare biochemical properties between the NP and AF by pooling data from each region (layers 1-4 for NP and layers 7-10 for AF). A Bonferroni correction was used to account for multiple comparisons.

A two-way analysis of variance (ANOVA), followed by post-hoc analysis with Holm-Bonferroni correction, was performed to evaluate differences in water-to-protein ratios measured by the traditional biochemical analysis and Raman spectroscopy (factors = disc region and measurement method). A similar analysis was conducted to compare relative collagen content distribution from the normalized SHG signal and traditional biochemical analysis. For DSC data, a Mann-Whitney U test was performed to compare NP and AF thermal properties. Median and interquartile range (IQR) were reported for each thermal property.

3.3. Results

3.3.1. Traditional biochemical assays

Water and s-GAG contents were relatively constant throughout the NP (*i.e.,* layers 1-4), except the water content of layer 1, which was significantly greater than the water content of layers 3 and 4 ($p < 0.05$; Figure 6A-B). No other differences in NP water content ($p \geq 0.3$) or NP s-GAG content were observed ($p \geq 0.8$; Figure 6C-D). In contrast, both water and s-GAG contents decreased from the inner AF to the outer AF (*i.e.,* layer 7-10; Figure 6). Overall, NP s-GAGs accounted for 30% to 36% of the tissue's dry weight (*i.e.,* 300-360 mg/g) or 6% by wet weight (*i.e.,* 60 mg/g). In the AF, s-GAGs accounted for 5% to 20% of the tissue's dry weight (*i.e.,* 50-200 mg/g) or 1% to 5% by wet weight (*i.e.,* 10-50 mg/g; Figure 6C-D). The water to s-GAG ratio did not change significantly within the NP; however, the water to s-GAG ratio of layer 10 was significantly greater than that of the inner AF layers (i.e., layers 7-8, $p < 0.05$; Figure 7).

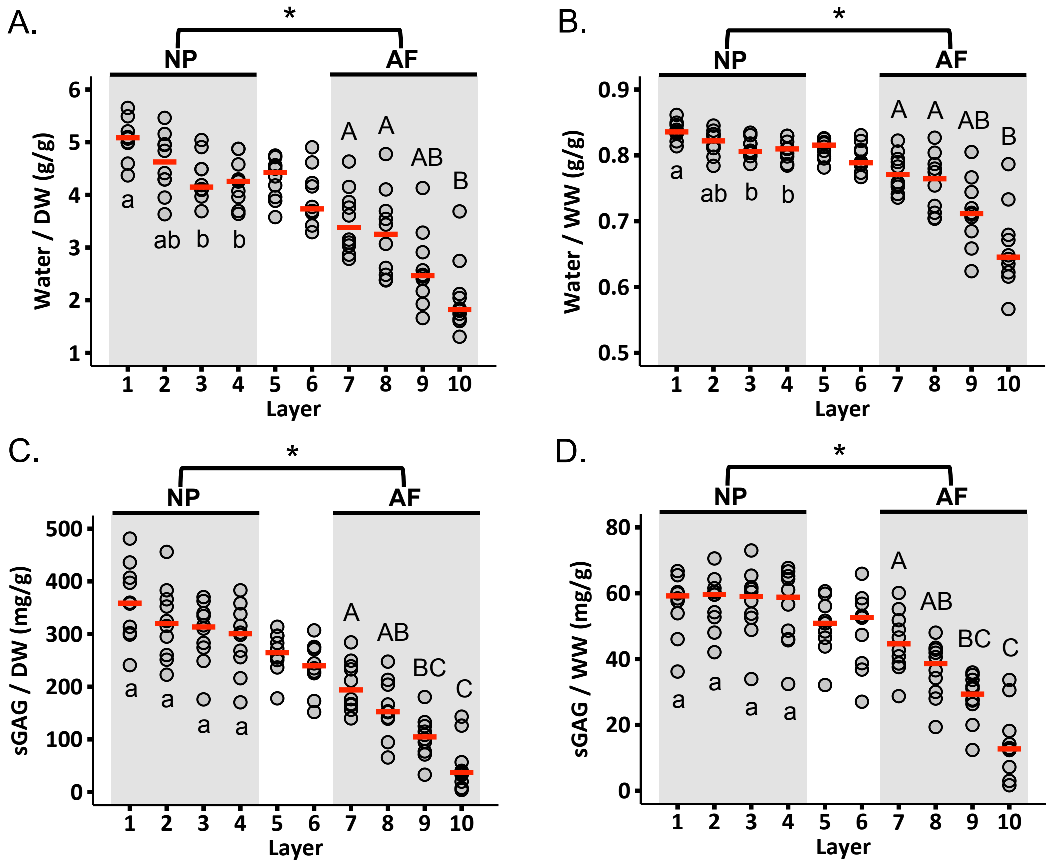

Figure 6: Radial distribution of water content normalized by (A) dry weight (DW) and (B) wet weight (WW). Radial distribution of sulfated GAG content normalized by (C) dry weight and (D) wet weight. Circles indicate individual data and red dashes indicate median values for each layer. NP and AF biochemical properties were compared using a Mann-Whitney U test on pooled data from Layers 1-4 (NP) and Layers 7-10 (AF; * represents $p < 0.05$). Differences in biochemical composition within each region (*i.e.*, shaded areas) were assessed using a Mann-Whitney U test with Bonferroni correction. Layers that do not share the same letter are significantly different ($p < 0.05$).

Collagen accounted for 28% to 47% of the NP's dry weight (*i.e.,* 280-470 mg/g) or 4% to 9% by wet weight (*i.e.,* 40-90 mg/g). In the AF, collagen accounted for 58% to 80% of the tissue's dry weight (*i.e.,* 580-800 mg/g) or 14% to 29% by wet weight (*i.e.,* 140-290 mg/g - Figure 8A-B). Collagen content normalized by dry weight in the outer AF was 2.5-fold greater than the collagen content at the disc center (6.6-fold difference when normalized by wet weight;

Figure 8A-B). However, no statistically significant differences were detected between layers in the NP or AF when collagen content was normalized by dry tissue weight (Figure 8A). Conversely, normalizing collagen content by wet weight indicated a statistically significant difference between layers 7 and 10 (p = 0.01; Figure 8B).

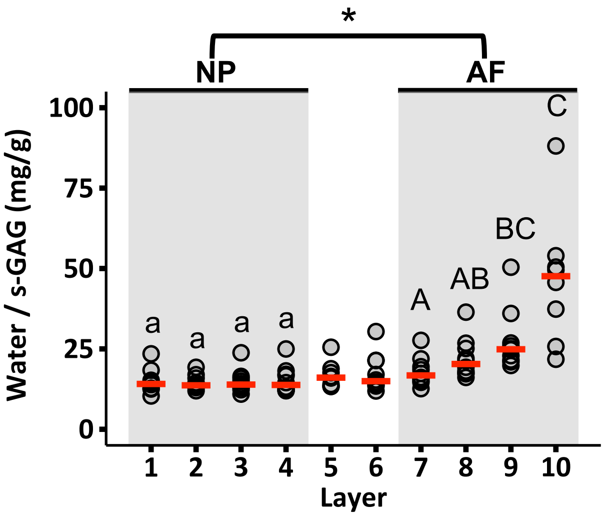

Figure 7: Radial distribution of water content normalized by sulfated GAG content. Circles indicate the individual data and red dashes indicate the median values. Values >100 in the last layer were omitted for clarity (n = 2 omitted values). NP and AF biochemical properties were compared using a Mann-Whitney U test on pooled data from Layers 1-4 (NP) and Layers 7-10 (AF; * represents $p < 0.05$). Differences in biochemical composition within each region (*i.e.*, shaded areas) were assessed using a Mann-Whitney U test with Bonferroni correction. Layers that do not share the same letter are significantly different ($p < 0.05$).

DNA content normalized by both dry and wet tissue weight was relatively consistent from the NP to the inner AF (Figure 8C-D). The median NP DNA content was 270 µg/g DW or 48 µg/g WW. Although DNA content was relatively constant from the NP to the inner AF, the median DNA content was higher in the outermost layer (Layer 10 – 607 µg/g DW or 209 ug/g WW; Figure 8C-D).

3.3.2. Swelling ratio

The swelling ratio decreased from 1.85 at the disc center to 0.5 in the outer AF, which represents a 185% increase in NP tissue mass and a 50% increase in outer AF tissue mass with swelling (Figure 9A). s-GAG leaching from tissue specimens was observed during free-swelling and the amount of leached s-GAGs was greater for the NP compared to the AF ($p < 0.001$ for NP *versus* AF; Figure 9B). s-GAG leakage corresponded to ~50% of the total s-GAG in the NP and ~30% of the total s-GAG in the AF (Figure 9D).

3.3.3. Raman spectroscopy

Raman spectra peaks were similar for the NP and AF, with sharp peaks at 863, 940, 1252, 1455 and 1661 cm^{-1}. Bands associated with amino acids and lipids dominated the spectral fingerprint for both regions (Figure 10A – < 1,800 cm^{-1}). Bands located at 2800 to 3020 cm^{-1}

were associated with stretching modes of CH_2 and CH_3, while bands at 3020 to 3800 cm^{-1} were associated with total water content (*i.e.,* free and bound water; Figure 11A). Moreover, the water spectrum was complex and exhibited contributions from multiple smaller peaks.

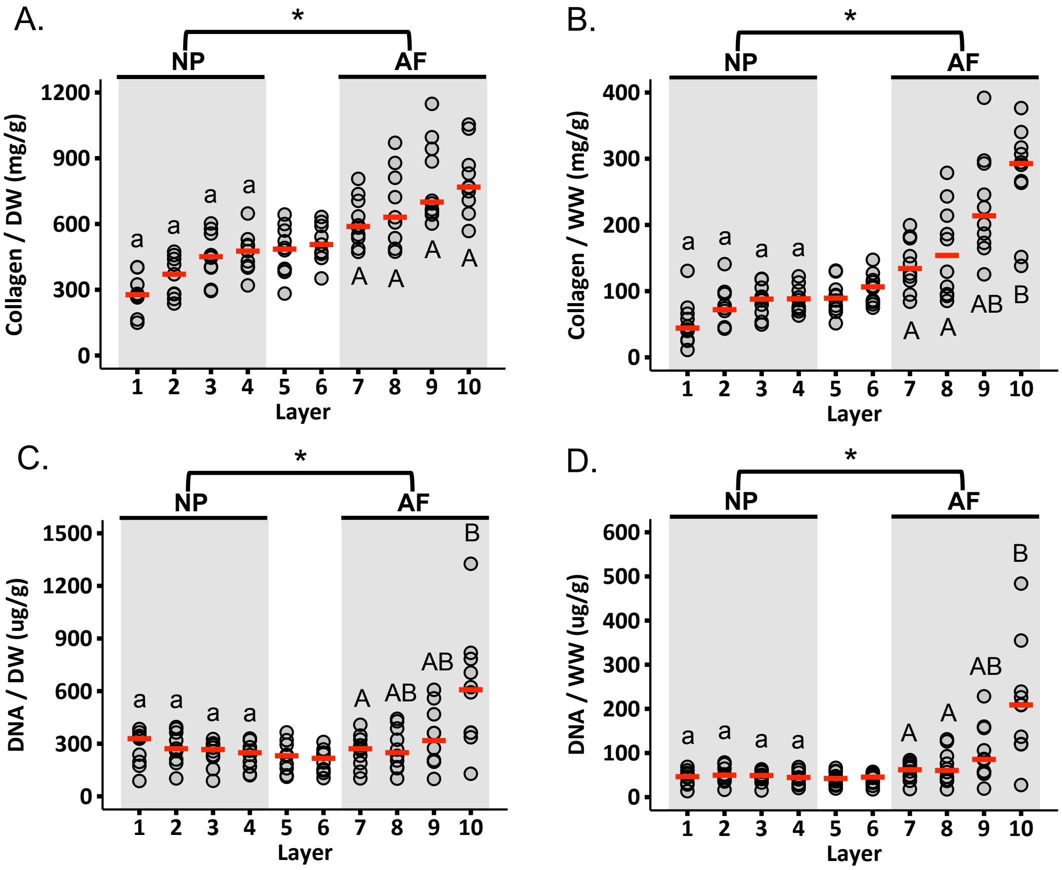

Figure 8: Radial distribution of collagen content normalized by (A) dry weight and (B) wet weight. Radial distribution of DNA content normalized by (C) dry weight and (D) wet weight. Circles indicate the individual data and red dashes indicate the median values. NP and AF biochemical properties were compared using a Mann-Whitney U test on pooled data from Layers 1-4 (NP) and Layers 7-10 (AF; * represents $p < 0.05$). Differences in biochemical composition within each region (*i.e.*, shaded areas) were assessed using a Mann-Whitney U test with Bonferroni correction. Layers that do not share the same letter are significantly different ($p < 0.05$).

The water-to-protein ratio was 7.5 at the disc center and decreased from the center of the disc to the outer AF ($p < 0.001$; Figure 10B-C). Importantly, the water-to-protein ratios of the inner NP and outer NP were significantly different ($p = 0.012$). Furthermore, the water-to-protein ratios obtained from Raman spectra agreed well with measurements from traditional biochemical assays (Figure 10C - solid *versus* light bars; two-way ANOVA: $p = 0.09$ for *measurement method* and $p = 0.001$ for *disc region*). The absolute amount of bound water content did not depend on disc region ($p = 1.0$; Figure 11A); however, bound water accounted for 3% of the total water content in the NP and 11% of the total water content in the outer AF (Figure 11B).

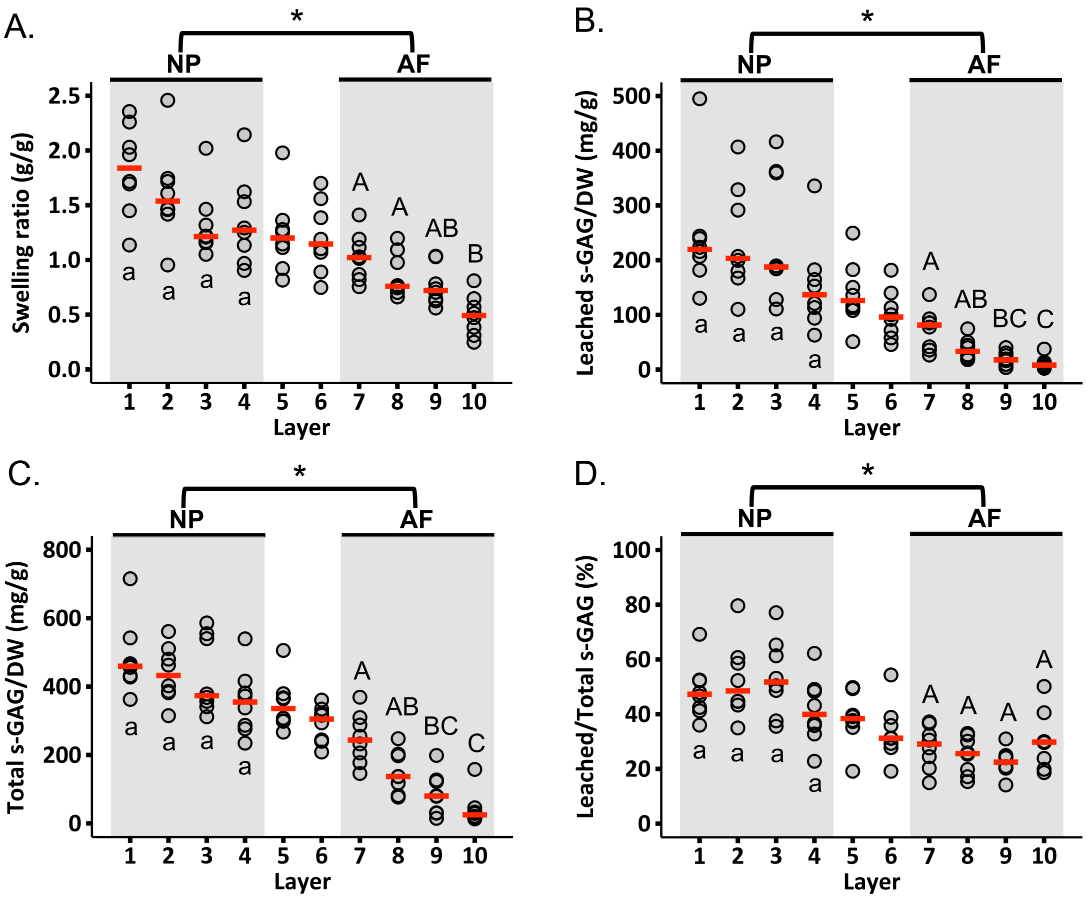

Figure 9: Radial distribution of (A) swelling ratio, (B) s-GAGs leached into the swelling solution normalized by dry weight, (C) total s-GAG normalized by dry weight, and (D) leached s-GAG normalized by total s-GAG. Circles indicate individual data and red dashes indicate median values. NP and AF biochemical properties were compared using a Mann-Whitney U test on pooled data from Layers 1-4 (NP) and Layers 7-10 (AF; * represents $p < 0.05$). Differences in biochemical composition within each region (*i.e.*, shaded areas) were assessed using a Mann-Whitney U test with Bonferroni correction. Layers that do not share the same letter are significantly different ($p < 0.05$).

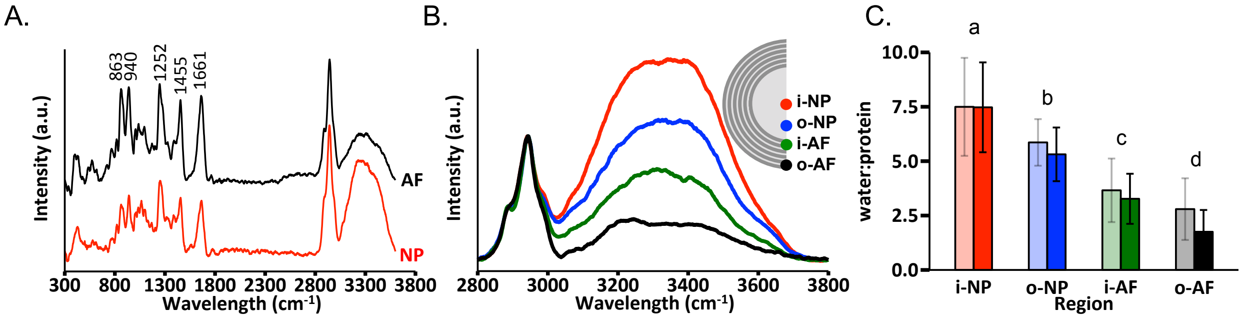

Figure 10: (A) Representative Raman spectra for nucleus pulposus (NP) and annulus fibrosus (AF) specimens. (B) Spectra from four regions within the disc to assess water content distribution, and (C) comparison of water-to-protein ratios collected from Raman spectroscopy (dark bars) and traditional biochemical analysis (light bars; two-way ANOVA – $p = 0.09$ for measurement method and $p = 0.001$ for disc region). Pairwise comparisons were performed using t-tests with Holm-Bonferroni correction. Layers that do not share the same letter are significantly different ($p < 0.05$).

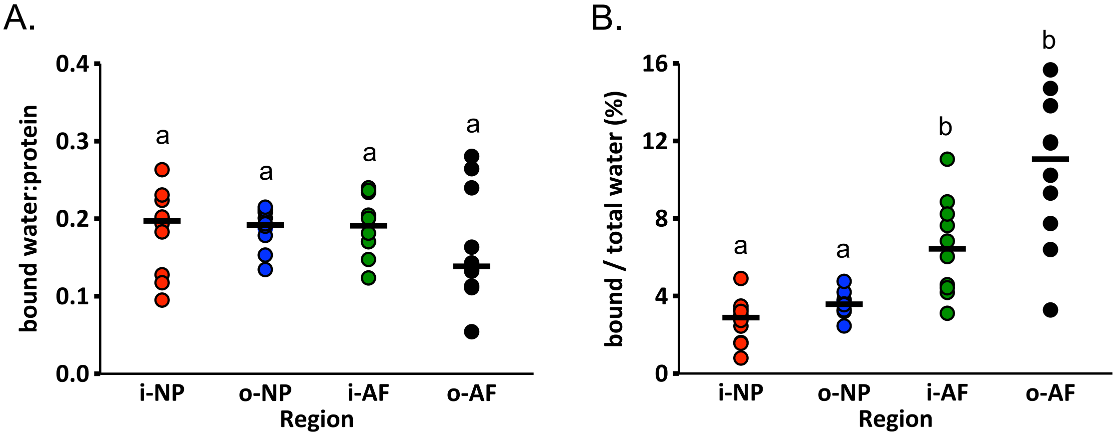

Figure 11: (A) Bound water content normalized by total protein content, and (B) percentage of bound water content with respect to total water content. Circles indicate the individual data and black dashes indicate the median values. Changes in biochemical composition were determined by performing Kruskal-Wallis test followed by pairwise comparisons using Mann-Whitney U test with Bonferroni correction. Layers that do not share a letter are significantly different ($p < 0.05$).

3.3.4. DSC analysis

The endothermic peak observed between -20°C and +10°C was associated with melting of ice, and the peak between 80°C and 150°C was associated with possible denaturation of tissue collagen (Figure 5A). There were no obvious differences in crystallization temperature (T_c), onset temperature of melting ($T_{m,onset}$), maximum melting temperature ($T_{m,max}$), onset temperature of denaturation ($T_{d,onset}$), and maximum denaturation temperature ($T_{d,max}$) between the NP and AF ($p \geq 0.09$; Table 3.1). However, enthalpy of crystallization (ΔH_c) and latent heat of melting (ΔH_m) were greater in the NP than the AF (Table 1). The median latent heat of melting in the NP was 246 J/g, indicating that 75% of the water in the NP was freezable water (*i.e.,* $\Delta H_m / \Delta H_{, pure\ ice}$). In contrast, the average total amount of freezable water in the AF was 65%.

Collagen denaturation was observed at temperatures as low as 65 °C, while the maximum temperature of denaturation ($T_{d,max}$) occurred near 110 °C (Figure 5A). The denaturation curve of the samples exhibited a small kink at lower temperatures (65°C-70 °C; * in Figure 5A). Heating specimens above T_d resulted in more than 70% tissue mass loss (0.82 g/g WW loss in the NP and 0.71 g/g WW loss in the AF – Table 1).

3.3.5. Multimodal nonlinear optical imaging

Multimodal images showed fiber architecture and the presence of lipid deposits in the disc (Figure 12A). The relative change in the SHG signal intensity throughout the disc was similar to the relative change in collagen content observed from the OHP assay (Figure 12B; two-way ANOVA: $p > 0.9$ for measurement method and $p < 0.001$ for disc region). Lipid deposits were distributed equally throughout the disc and appeared either as a single droplet or as clusters of small droplets (Figure 12C). However, there were noticeable differences between discs used for imaging lipids. That is, two of the three discs had a large amount of lipid droplets, while one disc had few to no lipid droplets. The distribution of lipid droplet area was highly skewed, such that 80% of lipid droplets were smaller than 5 μm^2 (diameter ≈ 2.5 μm), while the largest droplets had an area of ~230 μm^2 (diameter ≈ 17 μm).

Table 1: NP and AF values from differential scanning calorimetry

Region	T_c (°C)	ΔH_c (J/g)	$T_{m,onset}$ (°C)	$T_{m,max}$ (°C)	ΔH_m (J/g)	$T_{d,onset}$ (°C)	$T_{d,max}$ (°C)	m_{loss} (g/g)	WC (g/g)
NP	-12.8 (-13.8, -11)	303* (284, 319)	-4.0 (-4.2, -3.1)	1.7 (1.4, 2.8)	246* (236, 255)	97 (87, 99)	106 (104, 107)	0.82* (0.80, 0.83)	0.75* (0.71, 0.77)
AF	-12.7 (-16.9, -9.2)	205* (181, 266)	-3.7 (-3.8, -3.1)	4.2 (3.2, 5.0)	214* (193, 218)	89 (81, 97)	110 (107, 119)	0.71* (0.68, 0.73)	0.65* (0.59, 0.66)

Note: Data are expressed as median (interquartile range).
Abbreviations: AF, annulus fibrosus; m_{loss}, mass loss; NP, nucleus pulposus; T_c, crystallization temperature; $T_{d,max}$, maximum denaturation temperature; $T_{d,onset}$, onset temperature of denaturation; $T_{m,max}$, maximum melting temperature; $T_{m,onset}$, onset temperature of melting; WC, water content; ΔH_c, crystallization enthalpy; ΔH_m, latent heat of melting.
*Significant differences between NP and AF(Mann-Whitney U test, $P < 0.05$).

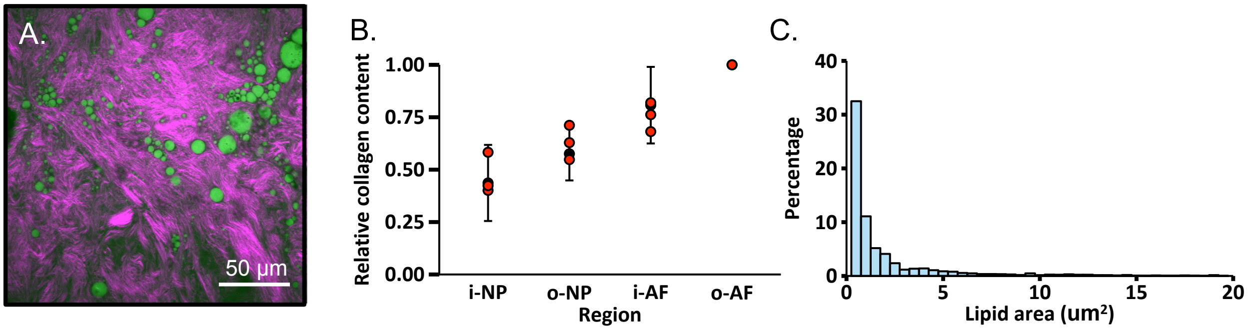

Figure 12: (A) Combined image from SHG (purple) and CARS (green, 2850 cm^{-1}) imaging. (B) Collagen content at the inner NP (i-NP), outer NP (o-NP), and inner AF (i-AF) normalized by collagen content of the outer AF (o-AF). Red circles represent SHG measurements, while black error bars represent mean ± standard deviation from the OHP assay. (C) Distribution of lipid droplet area throughout the disc obtained using the pooled data from the NP and AF. Data from lipids with areas greater than 20 mm^2 (~2%) are not shown for clarity.

3.4. Discussion

In this study, several measurement techniques were used to characterize radial variations in biochemical composition of bovine caudal discs. Specifically, water, sulfated GAGs, collagen, and DNA contents were measured with traditional biochemical assays to obtain quantitative measurements. Gravimetric water content was compared to measurements from Raman spectroscopy and DSC. Combined CARS and SHG microscopy was used to visualize lipids within the collagen fiber network, and explore the potential use of SHG imaging for measuring relative collagen content in the disc.

Most numerical studies describe the NP as a homogeneous isotropic material, whereas the AF is often described as a heterogeneous material (Sharabi et al., 2019; Williams et al., 2007). The results of the current study showed that the water content and water-to-protein ratio of the inner NP were greater than the values measured for the outer NP. Meanwhile, the swelling capacity (i.e., swelling ratio), collagen content, and DNA content were constant throughout the NP. In contrast, the AF exhibited radial variations in all biochemical properties. Water and s-GAG contents decreased, while collagen content increased from the inner AF to the outer AF, and our findings agreed well with previous studies (Beckstein et al., 2008; Liu et al., 2018; Showalter et al., 2012; van den Akker et al., 2017). Lastly, swelling capacity throughout the disc depended on the initial s-GAG content, where NP explants experienced higher swelling ratios than AF explants (Bezci et al., 2015; Urban and Maroudas, 1981).

Knowledge of cell density in healthy native tissues is important for regenerative medicine strategies that aim to inject stem cells or implant cell-based engineered tissues for disc repair (Sharma et al., 2014). The DNA content was constant throughout the NP, but increased nonlinearly across the AF. DNA content throughout the majority of the AF (*i.e.*, layers 7-9) was comparable to NP DNA content (<100 µg/g WW). However, there was a 2-fold increase in DNA content in the outermost AF layer. The increase in DNA content at the outer AF was most likely due to greater access to nutrients from surrounding blood vessels and connective tissues (Nerlich et al., 2007).

Similar to human disc tissue explants, bovine tissue explants released s-GAGs into the solution during swelling, where a greater percentage of s-GAGs were released by tissues with a greater initial s-GAG concentration (*i.e.,* the NP) (Urban and Maroudas, 1981). Region-specific differences in tissue properties, such as permeability, collagen architecture, and the size and distribution of proteoglycan molecules, likely account for differences in swelling properties between the NP and AF, as well as throughout the AF (Melrose et al., 1994; Périé et al., 2005; Urban and Maroudas, 1981). Furthermore, s-GAG leakage may increase as effective pore size increases with swelling (Périé et al., 2005). Importantly, GAGs are thought to primarily contribute to compressive mechanical behavior, but recent work has highlighted the importance of GAGs in AF tensile mechanics (Perie et al., 2006; Werbner et al., 2019). Thus, GAG loss during long duration tests may affect tissue mechanics, particularly during tests that may include partial or full recovery in an aqueous solution.

To the best of our knowledge, the spatial distribution of lipids within the disc collagen network has not been presented. Hence, multimodal microscopy was used to obtain a quick simultaneous imaging of collagen fibers and lipid droplets without the need of external dyes or fixatives, as used for histology. Images confirmed the presence of lipid droplets (Franklin and Hull, 1966). Lipids appeared throughout the disc, either as isolated spheres or as clusters, and the majority of droplets were smaller than ~1.5 µm in diameter. Lipids have also been observed in other collagen-rich connective tissues, and various factors, such as age, degeneration, diet, and exercise, have been reported to influence lipid concentration (Bonner et al., 1975; Daemen et al., 2018; Finlayson and Woods, 1975; Rabinowitz et al., 1979). This study only evaluated lipid content in healthy discs, but it is possible that age and disease will affect the lipid concentration in the disc, based on observations in cartilage and tendon (Bonner et al., 1975; Kannus and Jozsa, 1991). Additional work is needed to understand the role and concentration of lipids throughout the disc with aging, degeneration, and diseases.

Raman spectroscopy has been used to investigate biochemical composition of various tissues, including cartilage, bone, skin, and brain (Albro et al., 2018; Lim et al., 2011; Pezzotti et al., 2015; Unal et al., 2014; Wolthuis et al., 2001), but there has been little to no work on the intervertebral disc. Similar to observations in other tissues, Raman spectra of bovine discs were dominated by vibrational bands from structural proteins and lipids. As expected, there were similarities between NP and AF spectra, due to similarities in tissue composition (*i.e.*, water, s-GAG, and collagen content). Raman spectra of the bovine disc exhibited sharp peaks at 863, 940, 1252, 1455, and 1661 cm^{-1}. Peaks at ~860 and ~940 cm^{-1} have been previously identified as a marker for C-C stretching vibrational mode of proline and hydroxyproline residues in collagen (Bonifacio and Sergo, 2010; Flach and Moore, 2013). Bands with a peak at 1252 cm^{-1} and 1661 cm^{-1} have been associated with amide III and amide I, respectively, where amide I mainly reflects the C=O stretching vibration and the amide III band has contributions from several chemical bonds (Gniadecka et al., 1998b; Talari et al., 2015). In biological tissues, amide bands have been primarily used to study age- and disease-related alterations in protein secondary structure and conformation (Gniadecka et al., 1998b; Manoharan et al., 1996; Téllez Soto et al., 2018). The peak at ~1455 cm^{-1} corresponds to deformation vibrations of CH_2 and CH_3 amino acid side chains and lipids (Gniadecka et al., 1998a). It should be noted that Raman vibrations have been related to more than one amino acid or chemical group, making it difficult to identify differences in the fingerprint region. Hence, only predominant peak locations were reported and compared between disc regions.

In contrast, differences in the high-frequency region (*i.e.,* > 2800 cm^{-1}) were easily identifiable and used to determine radial distributions of bound and free water (sometimes referred to as 'mobile' or 'freezable' water) (Brooks, 1934; Tang et al., 2017; Unal and Akkus, 2018; Q. Zhang et al., 2011). While freeze- or air-drying tissue specimens is frequently used to remove free water molecules, removal of bound water is more difficult, requiring drying under very low pressures and high temperatures or chemical treatments (*e.g.*, acetone or ethanol) (Agee et al., 2015; Unal and Akkus, 2018). Hence, water content values commonly reported only refer to the amount of free water in the tissue (Antoniou et al., 1996; Cortes et al., 2014; Iatridis et al., 2007). We measured the contribution of bound water to the total water content by evaluating changes in Raman spectra after freeze-drying. Our finding suggests that only a small portion of the total water content is bound to macromolecules in the matrix (*i.e.,* proteoglycans and collagen; 3% in the NP and 11% in the AF, Figure 11B). Thus, the majority of water molecules are mobile and free to diffuse out of the disc during loading or dehydration. The relative bound water content in the NP agreed well with reported values (~4%) for cartilage (Padalkar et al., 2013; Unal and Akkus, 2018), but the concentration of bound water in the NP and AF was lower than the concentration measured for bovine pericardium, skin, and muscle (25%-40%) (Aktaş et al., 1997; Samouillan et al., 2011; Tang et al., 2017).

Thermal properties of the bovine disc were determined to identify temperatures associated with water freezing and melting, and collagen stability. The second endothermic peak, observed to start at temperatures as low as 65°C, is associated with collagen denaturation, where interchain hydrogen bonds rupture, causing irreversible damage to the collagen structure (Huang et al., 2019; Samouillan et al., 2011). Denaturation temperatures for AF and NP were similar to each other and to other biological tissues, such as bovine pericardium, rat-tail tendon, and human skin (Miles and Ghelashvili, 1999; Samouillan et al., 2011; Tang et al., 2017). The small kink observed between 65°C and 70°C (Figure 5 – '*') has been associated with cleavage of weak bonds between water and matrix macromolecules or conformational changes within fibrils (*e.g.*, partial fibril shrinkage), rather than breaking of stronger bonds, which occurs at a slightly higher temperature (~80°C) (Bozec and Odlyha, 2011; Chae et al., 2009).

This study is not without its limitations. First, there was high variability in measured properties despite our attempts to minimize potential sources for variation (*e.g.*, pre-hydrating tails to provide similar hydration history for each specimen). Second, we only measured major proteins found in the disc. For example, the NP and inner AF are comprised of mostly type II collagen, while the outer AF contains predominantly type I collagen (Antoniou et al., 1996). It is also known that other types of collagen exist, as well as elastin and non-collagenous proteins (Ghosh et al., 1977). Despite the wide use of SHG microscopy for label-free imaging of collagen fibers, this technique cannot be used to visualize all types of collagens, such as collagen type III, which emits a weak SHG signal (Ranjit et al., 2015). Third, Raman spectroscopy and multimodal imaging can be used to investigate biochemical composition at a molecular level, but assessing protein structures at that scale was not the primary focus of this work. Lastly, water was mainly referred to as being bound or free; however, the complex water spectra suggest the presence of multiple distinct water fractions as suggested in previous studies (*e.g.,* weak versus strong hydrogen bonds, free, or bulk water) (Kudo et al., 2014; Unal and Akkus, 2018). Further analyses of the complex water spectra may provide insights into the structure of different water-protein interactions in biological tissues, particularly with respect to age- or disease-related changes.

In summary, a variety of measurement techniques were employed to characterize radial variations in bovine caudal disc biochemical composition. Traditional biochemical analyses were used to provide absolute, quantitative measurements. Furthermore, Raman spectroscopy was used to obtain radial distributions of bound water content. Some heterogeneity was observed in the NP, where the water content and water-to-protein ratio of the inner NP were greater than the outer NP. In contrast, the bovine AF exhibited a more heterogeneous distribution of biochemical properties. To better capture native tissue mechanics, computational studies should incorporate both compositional and structural heterogeneities. Furthermore, this study highlighted the potential use of less destructive techniques, such as multimodal imaging and Raman spectroscopy, to characterize biochemical composition. Comparable results between OHP assay and SHG imaging highlight the potential benefit of using SHG microscopy as a less destructive method for measuring collagen content, particularly when relative changes are of interest. Future work will use non-destructive, label-free measurement techniques to investigate the effect of age and disease on the distribution of biochemical composition in animal and human discs.

4. Osmotic pressure alters time-dependent recovery behavior of the intervertebral disc[2]

4.1. Introduction

The intervertebral disc is subject to a wide range of compressive loads that cause fluctuations in mechanics, water content, and disc height (Costi et al., 2002; Wilke et al., 1999). The water contents of the nucleus pulposus and annulus fibrosus are altered by proteoglycan composition and osmotic pressure (Bezci et al., 2015; Malko et al., 2002; McMillan et al., 1996; Sivan et al., 2006). A decrease in proteoglycan content with injury or degeneration decreases the tissue's swelling capacity, altering fluid flow behavior into and out of the disc (Pearce et al., 1987; Roughley, 2004; Urban and McMullin, 1988). Fluid flow out of the disc occurs through mechanical loading, while fluid flow into the disc occurs through passive diffusion due to an imbalance of ions between the disc and its surrounding environment (Ayotte et al., 2001; O'Connell et al., 2011; Schroeder et al., 2007; Vergroesen et al., 2016). However, the role of osmotic pressure in fluid flow into the disc has not been well studied and is important for understanding disc recovery mechanisms.

The intervertebral disc is a poroviscoelastic material that experiences large fluctuations in water composition throughout a diurnal loading cycle. Mechanical loading on the disc results in an initial elastic response, followed by a time-dependent response. The viscoelastic response is influenced by intrinsic and extrinsic factors. Intrinsic factors include disc composition and geometry, whereas extrinsic factors include load magnitude and duration (Gardner-Morse and Stokes, 2003; Lu et al., 1996; O'Connell et al., 2011; Urban and Roberts, 2003). For example, the porosity of the solid matrix contributes to the time-dependent response because of fluid moving through pores with loading, providing the disc with its excellent resistance to compression (Urban and Maroudas, 1981). Rheological models have been used to understand the role of these factors on the disc's time-dependent behavior, by monitoring disc height changes during creep, or unloaded recovery (Vergroesen et al., 2016; Wilson et al., 2005). These models have been valuable in demonstrating significant differences in material properties with loading response, recovery behavior, injury, and degeneration (Hwang et al., 2012; Johannessen et al., 2006; MacLean et al., 2007; O'Connell et al., 2011; Vergroesen et al., 2015).

A diurnal loading cycle includes large compressive loads that are sustained throughout the day and reduced during bed-rest recovery. Previous studies demonstrated that the rate of disc height recovery during unloading is 3 to 4 times slower than the rate of disc height loss during loading, suggesting that passive diffusion of water molecules is not sufficient for full recovery within 8 hours. Incomplete disc height recovery also results in additional disc height loss during subsequent loading cycles (Schmidt et al., 2016b; Vergroesen et al., 2014). More recent work has focused on the strong relationship between disc hydration and mechanical properties by using osmotic pressure to alter water absorption and intradiscal pressure during loading (Bezci et al.,

---

[2] Previously published as "Bezci, S.E., O'Connell, G.D., 2018. Osmotic Pressure Alters Time dependent Recovery Behavior of the Intervertebral Disc. Spine (Phila. Pa. 1976). https://doi.org/10.1097/BRS.0000000000002354"

2015; Charnley, 1952; Drost et al., 1995; Schmidt et al., 2016b; Stokes et al., 2011). Stokes and coworkers observed a decrease in joint stiffness with an increase in water uptake during stress-relaxation (constant applied displacement) (Stokes et al., 2011). Vergroesen *et al.* demonstrated that the effect of osmotic pressure on water absorption is highly dependent on magnitude of the applied load (Vergroesen et al., 2014). However, it is not clear how osmotic pressure affects disc recovery behavior under low loading conditions that simulate bed-rest conditions (Wilke et al., 1999).

The intervertebral disc needs to maintain adequate hydration to absorb and transmit loads to surrounding tissues (Chan et al., 2011; O'Connell et al., 2015). Our previous work used osmotic pressure to evaluate the effect of disc hydration on mechanical behavior during loading. We observed that hyperosmotic loading altered the time-dependent behavior by increasing the apparent compression stiffness (Bezci et al., 2015). Although previous studies have investigated the effect of osmotic swelling on water uptake during loading, it is still unclear how osmotic swelling, decoupled from mechanical loading, alters recovery response, and nutrient transport. Therefore, the objective of this study was to evaluate the effect of osmotic pressure on the unloaded recovery response of healthy discs.

4.2. Materials and methods

4.2.1. Sample preparation

Five caudal spine sections from skeletally mature bovines were acquired from the local abattoir (age ~18 months), and were selected based on their similarities to young and healthy human discs in disc height, matrix composition, and mechanical properties (Alini et al., 2008; Demers et al., 2004; O'Connell et al., 2007b; Showalter et al., 2012). As mechanical and biochemical properties of the disc vary through the length of the spine, only the first three levels of the bovine caudal spine were used in this study (Demers et al., 2004). Motion segments (n = 15) were prepared from the top three levels by removing the surrounding soft tissues and cutting through the mid-transverse plane of the superior and inferior vertebral bodies with a band saw. The inferior and superior vertebrae were embedded in polymetheylmethacrylate (PMMA) dental cement to ensure parallel loading surfaces and parallel alignment of the disc's mid-transverse plane with the loading platens. Potted motion segments were wrapped with saline-soaked gauze (0.15 M phosphate buffered saline, PBS) and frozen until testing.

Experiments were performed in a saline bath to provide continuous tissue hydration during testing. PBS solutions were prepared at a concentration of 3.0 M, and then diluted with de-ionized water to make 1.5, 0.75, 0.15, and 0.015 M PBS solutions (0.15 M PBS: 137 mM NaCl, 2.7 mM KCl, 5.4 mM Na_2HPO_4, and 0.6 mM KH_2PO_4). In addition, 1 N HCl or 2 N NaOH was used to adjust the solution pH to 7.4. The osmotic pressure of the saline solutions was calculated by the Van't Hoff equation, $\pi = MRT$, where M is the solution molarity (mol/L), R is the gas constant (8.3 J/mol-K), and T is the temperature (298 K).

4.2.2. Mechanical testing

Samples were thawed in a refrigerated PBS bath for 24 hours to allow discs to reach steady-state hydration, and then allowed to equilibrate to room temperature before testing (Figure 13A). Motion segments were attached to custom grips in a water bath designed for an 858 Bionix hydraulic material testing machine (MTS Systems Corp., Eden Prairie, MN). A nominal preload (20 N) was applied and held for 10 minutes to ensure that the loading platen was engaged with the sample. Then, a 300 N axial compressive load (~0.5 MPa compressive stress) (O'Connell et al., 2007b) was applied and maintained for 2 hours (Figure 13B). At the end of creep, the PBS solution was replaced with fresh PBS using a water pump and samples were allowed to recover for 12 hours at 20 N. All samples were tested in 0.15 M PBS during creep; however, the PBS concentration was varied during recovery (0.015, 0.15, 0.75, or 1.5 M) (Figure 13C), with the 0.15 M PBS serving as the control. Force and displacement were recorded throughout the test.

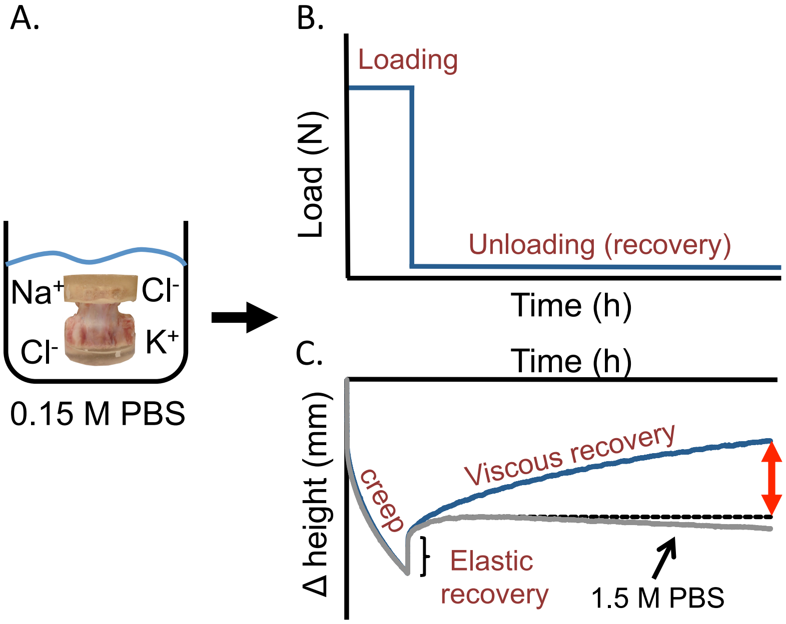

Figure 13: (A) Samples were hydrated in a saline bath (0.15 M PBS) before testing. (B) Samples were tested under axial compression for 2 hours, followed by unloaded recovery for 12 hours. (C) Schematic of changes in disc height during. A reference disc height (dashed line) was defined as the maximum disc height recovered under hyperosmotic pressure (1.5 M PBS) and was used as a reference displacement. The difference between the reference displacement and final displacement after recovery was measured for the other experimental groups (blue line) (*i.e.*, 0.015 M, 0.15 M, and 0.75 M PBS). This difference in disc height recovery was used to estimate the osmotic condition that would result in elastic-only recovery behavior, and this osmotic condition was referred to as the balance concentration.

Each sample was tested five times to perform a paired statistical analysis, and the testing order was randomized with a 24-hour recovery in 0.15 M PBS between tests. Upon completion of all saline recovery groups, the first test was repeated to confirm repeatability and to ensure that the disc was not damaged or altered during testing. A paired Student's t-test confirmed that there were no significant differences between the first and last tests ($p > 0.2$). After mechanical testing, discs were removed from the surrounding vertebrae and visually examined to confirm that they did not have any damage or degeneration.

4.2.3. Data analysis

Experimental data were analyzed using a custom-written Matlab algorithm (Mathworks, Inc., Natick, MA). The time-dependent recovery response was curve-fit to a 5-parameter rheological model that included two Voigt solids with a spring in series (lsqcurvefit function, Equation 1). Each Voigt solid consists of a spring (S_i, N/mm) and a dashpot (η_i, N-s/mm) in parallel, and describes the slow and fast time-dependent responses under an applied stress (time constant $\tau_i = \eta_i/S_i$) (Johannessen et al., 2006; Keller et al., 1988; O'Connell et al., 2011). To simplify the model to four parameters, the elastic response parameter ($1/S_E$) was fixed based on the elastic displacement measured during recovery. Curve fits with a coefficient of determination (R^2) greater than 0.95 was considered a good fit.

$$d = L * \left[\left(\frac{1}{S_1}\left(1 - e^{-\frac{t}{\tau_1}}\right)\right) + \left(\frac{1}{S_2}\left(1 - e^{-\frac{t}{\tau_2}}\right)\right) + \frac{1}{S_E}\right] \tag{1}$$

As the equilibrium time is known to take longer than 12 hours (O'Connell et al., 2011; van der Veen et al., 2007), five additional samples were used to evaluate long-duration recovery (48 hours) in 0.15 M PBS. Data from the long-duration recovery tests were used to confirm model parameters determined from the 12-hour dataset. Once validated, the rheological model was used to predict equilibrium displacement (d_{eq}) and time (t_{eq}) for recovery. Equilibrium displacement was calculated at $t = \infty$, and equilibrium time was determined as the time where displacement was 99% of the equilibrium displacement. Total recovery at equilibrium was calculated as the displacement during recovery divided by the displacement during loading.

Finally, the saline concentration needed to yield a negligible viscous recovery response was estimated as a balance between external osmotic pressure and internal pressure during recovery. To calculate the ''balance concentration'', the disc height change at the end of recovery was measured with respect to a reference point (Figure 13C – red arrow), which was defined as the maximum disc height achieved during recovery in hyperosmotic loading (1.5 M PBS) (Figure 13C – dashed line). A linear regression was used to describe the data, and the x-intercept was defined as the balance concentration.

4.2.4. Statistical analysis

A one-way repeated measures analysis of variance (ANOVA) was performed on recovery parameters, with a factor of osmotic loading condition. A Tukey post-hoc analysis was performed to determine differences between groups. A two-way repeated measures ANOVA was performed on the percent recovery after 4, 8, and 12 hours of recovery (factors of time and osmolarity). All statistical analyses were performed using Matlab ($p \leq 0.05$ for significance). Values were reported as mean ± standard deviation, unless stated otherwise.

4.3. Results

The instantaneous elastic displacement in creep was 1.06 ± 0.28 mm and accounted for 40% of the total disc height loss during loading (2.74 ± 0.69 mm; $\Delta d/\Delta t$ at 2-hours = 0.41 ± 0.10 mm/h; pooled averages). Elastic displacement during recovery was not altered with osmotic pressure (0.53 ± 0.12 mm; $p > 0.7$) and accounted for approximately 30% of the total displacement during recovery in the control group (0.15 M PBS).

Viscoelastic recovery was highly dependent on saline bath concentration and recovery time ($p < 0.0001$) (Figure 14). Full disc height recovery was not observed within 12 hours for any test group (Figure 14A). Approximately 36% to 50% of disc height recovery occurred within the first 4 hours for all test groups. Recovery displacements for the 0.015, 0.15, and 0.75 M PBS groups were significantly different at 4, 8, and 12 hours of recovery ($p < 0.05$; Figure 14B). For the 0.015 and 0.15 M PBS groups, the disc height recovery increased over time (Figure 14B – white and black bars). However, recovery in a hyperosmotic solution (e.g., 1.5 M PBS) demonstrated a reverse trend in disc height recovery after ~4 hours of recovery, such that the disc exhibited features of loading rather than recovery (Figure 14B – diagonal stripped bar).

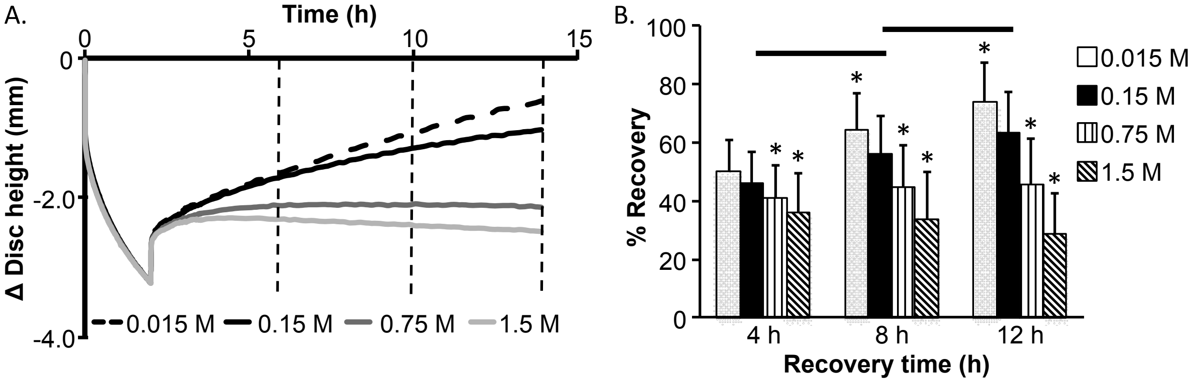

Figure 14: (A) Disc height change during recovery for a representative sample. Dashed vertical lines represent time points used to calculate "percent-recovery", which was defined as the displacement during recovery divided by the displacement during loading. (B) Percent-recovery after 4, 8, and 12 hours of recovery. The percent-recovery increased over time for the control group (0.15 M PBS; $p < 0.05$, black lines). *Represents differences between the osmotic loading group and the control.

The rheological model described experimental data well ($R^2 = 0.99$; Figure 15 – circles versus solid line), except for the 1.5 M PBS group, because of the reverse trend during recovery (Figure 14A – light grey line). Therefore, model parameters were only reported for 0.015, 0.15, and 0.75 M PBS groups. The fast time constant, τ_1, was on the order of minutes, whereas the slow time constant, τ_2, was on the order of hours. The time constant and stiffness for the fast response were not dependent on osmolarity ($p > 0.3$) (Figure 16A and B). In contrast, the slow time constant decreased as bath osmolarity increased ($p < 0.01$; Figure 16C), whereas the stiffness for the slow response increased with osmolarity ($p < 0.0001$) (Figure 16D).

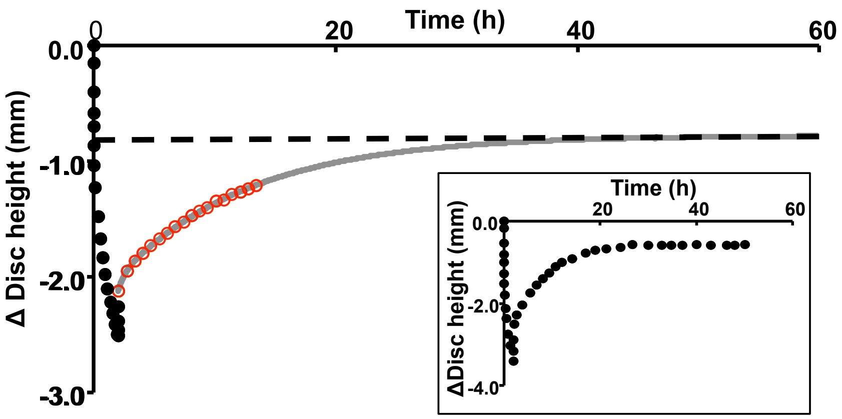

Figure 15: Disc height change from a representative sample. Circles represent experimental data, the grey line represents the model fit, and the dashed black line indicates equilibrium disc height. Inset – A small subset of specimens was allowed to recover for 48 hours, rather than 12 hours, to validate the predicted equilibrium time.

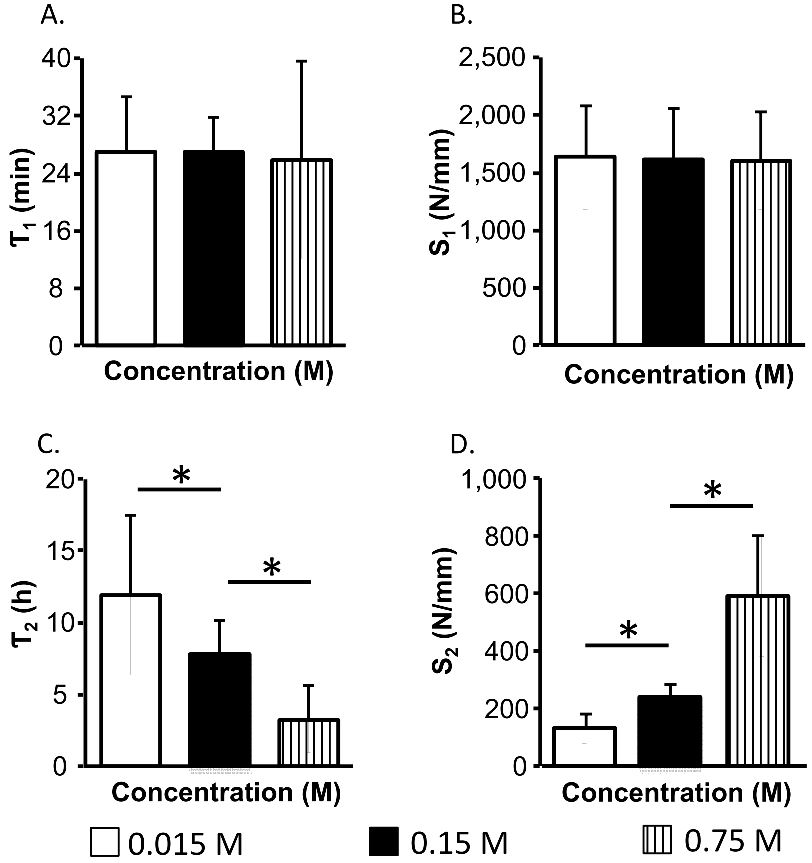

Figure 16: (A-B) Fast response and (C-D) slow response model parameters. τ represents the time constant, which is a function of the dashpot and spring stiffness in the Voigt models, and S_i represents the spring stiffness. *Represents $p \leq 0.05$ with respect to 0.15 M PBS control group.

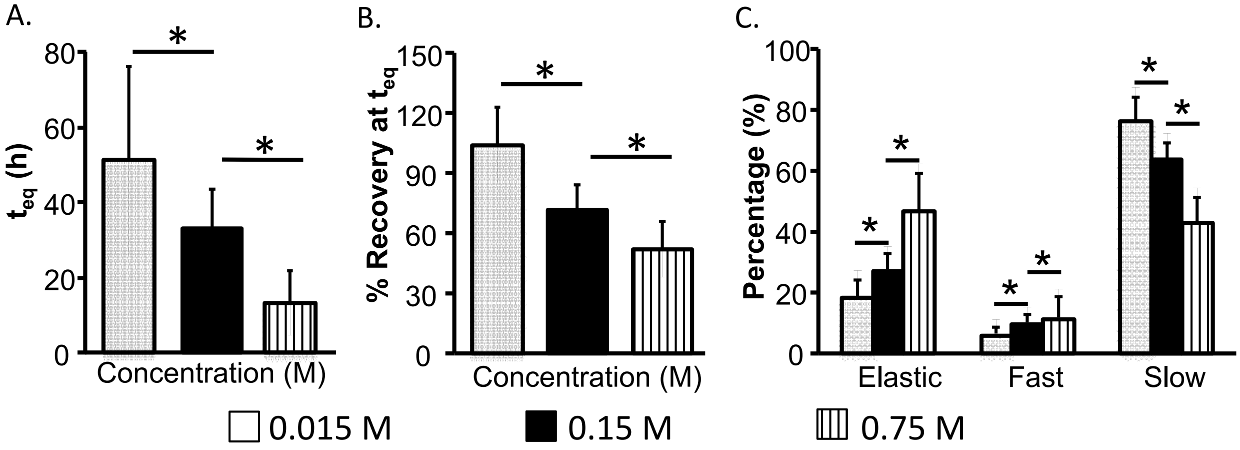

Figure 17: (A) Equilibrium time (t_{eq}) for each osmotic group. (B) Percent recovery at equilibrium (t_{eq}). (C) Contributions of elastic, fast viscous and slow viscous responses shown as a percentage of the total recovery for each group. *Represents $p < 0.05$ with respect to 0.15 M PBS control group.

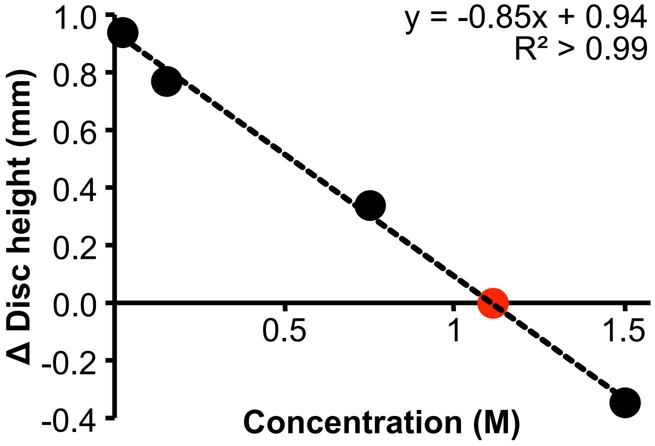

Figure 18: Balance concentration (red dot) for a representative sample. The balance concentration was defined as the x-intercept of a linear regression between the maximum disc height change during recovery and saline osmolarity (see Figure 14).

The rheological model was used to predict equilibrium time and displacement. The predicted equilibrium time and percent recovery using model parameters determined from the 12-hour recovery data agreed well with experimental data from 48-hour recovery tests (unpaired Student t test, $p > 0.33$) (Figure 15 – dashed line vs. inset data). Equilibrium time was 33.0 ± 10.7 hours for the 0.15 M PBS group and was altered with osmotic loading ($p < 0.001$) (Figure 17A). The equilibrium time for the 0.015 M PBS was 51.2 ± 24.9 hours, which was ~1.5X greater than the control group equilibrium time. In contrast, the equilibrium time for the 0.75 M PBS group was 60% lower than the control group equilibrium time. Recovery at equilibrium was dependent on PBS osmolarity ($p < 0.001$). The predicted recovery was 74 ± 15% of the total disc height loss during loading for the 0.15 M PBS group, whereas full recovery was predicted for the 0.015 M PBS group (104 ± 18%) (Figure 17B). The relative contributions of each model parameter were dependent on osmolarity ($p < 0.001$) (Figure 17C). Slow viscous recovery was the primary recovery mode for the hypo-osmotic and control groups (>60%), whereas the elastic recovery was the primary mode for disc height recovery in the hyperosmotic group (~46%). The balance concentration between mechanical loading and osmotic pressure was 1.23 ± 0.16 M PBS (Figure 18).

4.4. Discussion

During bed rest recovery, water is reimbibed into the disc. Full recovery of disc height and water content is important for preserving the mechanical function of healthy discs. In this study, we evaluated the influence of osmotic pressure on disc height recovery after creep to elucidate the effect of fluid-flow dependent recovery mechanisms. External osmotic pressure was created through ion imbalance between the saline solution and negatively charged proteoglycans. The data reported here decouple fluid-flow dependent behavior from fluid-flow independent behavior during recovery. That is, the elastic and short-term viscous recovery responses were independent of osmotic pressure, whereas passive diffusion of water was highly dependent on saline bath osmolarity and was the driving mechanism in long-term recovery.

The rheological model provided a simplified model of the disc to differentiate between the short- and long-term viscous recovery. The physical meaning of short- and long-term recovery responses, which correspond to the fast and slow time constants, is not well understood. However, the model has been successful in noting differences in recovery mechanisms with degeneration and nucleotomy (Johannessen et al., 2006; O'Connell et al., 2011). Previous studies observed significant changes in the fast response as a result of compositional changes in the nucleus pulposus, suggesting that the slow response may be related to fluid flow through the annulus fibrosus. In the current study, osmotic pressure altered the slow response, but not the fast response. Taken together, our findings agree with the notion that the fast response is governed by flow-independent recovery (e.g., immediate or recovery in air), which is related to the intrinsic properties of the disc. Therefore, discs subjected to severe morphological alterations with degeneration or nucleotomy would likely manifest as differences in the fast recovery behavior.

The rate and magnitude of fluid-flow dependent recovery were highly sensitive to the saline osmolarity that, in turn, governed disc height recovery. The increase in water uptake and disc height recovery with hypo-osmotic pressure agrees well with data in the literature (Stokes et al., 2011; Vergroesen et al., 2016). Mechanical loading (Vergroesen et al., 2016) and loading from osmotic pressure during recovery hinder fluid-flow into the disc and disc height recovery (Figure 14A). For example, disc recovery in the 1.5 M PBS group exhibited features of loading after 4 hours of recovery, suggesting a change in fluid-flow direction from inflow to outflow. During diurnal recovery, intradiscal pressure is ~80% lower than the stress measured during standing (Wilke et al., 1999); however, little is known about changes in the tissue environment osmolarity throughout a diurnal loading cycle (Urban and McMullin, 1988). These findings suggest that full disc height recovery can be achieved in vitro through a combination of low osmotic pressure and low mechanical loading.

The osmotic condition that limited disc height recovery to an elastic-only response after creep was approximately 1.2 M PBS. Similarly, data reported by Vergroesen *et al.* demonstrated a balance between osmotic pressure and mechanical loading with respect to the disc's ability to increase water uptake during compression. The balance between mechanical loading and osmotic pressure was near 1.8 MPa (1200 N for caprine discs) (O'Connell et al., 2007b; Y. Zhang et al., 2011), which was half of the balance stress calculated for bovine discs in this study (~3.6 MPa for 1.2 M PBS). Differences between the two studies are likely because of geometrical differences in disc height and volume (disc height: caprine = 3 – 4 mm, bovine = 7 mm) (O'Connell et al., 2007b; Y. Zhang et al., 2011), as the disc area, glycosaminoglycan content, and water composition are comparable between the two species (~600 – 680 mm^2, ~600 µg/mg dry weight) (Beckstein et al., 2008; Detiger et al., 2015; Y. Zhang et al., 2011). Establishing a relationship between disc behavior and external osmotic pressure will be helpful for measuring intradiscal pressure without the use of pressure sensors, which might alter disc mechanics because of annular injuries (Elliott et al., 2008).

The bovine caudal disc is an ideal animal model to study disc mechanics of the healthy human disc, based on similarities in biomechanical composition, disc height, swelling pressure, and mechanical properties (Alini et al., 2008; Demers et al., 2004; O'Connell et al., 2007b; Oshima et al., 1993; Showalter et al., 2012). However, the bovine discs do not exhibit signs of degeneration or aging like the human disc (Demers et al., 2004). Negatively charged proteoglycans of the intervertebral disc play a crucial role in tissue swelling, by attracting water molecules into the disc. The proteoglycan content in the annulus fibrosus is lower in the bovine disc than the human disc (Demers et al., 2004), suggesting that some differences may exist for mechanical properties measured under osmotic loading conditions.

There are some limitations that should be noted. Bone-disc-bone motion segments were used in this study to examine the individual response of a single intervertebral disc to osmotic pressure, which limits our ability to observe differences in stress distribution with surrounding tissues. During testing, creep was not long enough to reach equilibrium; however, loading was intentionally kept short to investigate multiple recovery conditions for each specimen. Each sample was tested multiple times to perform a paired statistical analysis. Although full recovery in disc height was not observed, we did observe complete recovery in disc joint mechanics, which is comparable to data in the literature (MacLean et al., 2007; O'Connell et al., 2011; van der Veen et al., 2005). Disc rehydration behavior depends on many factors (Bezci et al., 2015; O'Connell et al., 2011; Vergroesen et al., 2016). Direct comparison with data reported in the literature is difficult because of variations with animal models, experimental protocols, including recovery with an applied load, removal of endplates and adjacent vertebrae, and level of disc degeneration (Charnley, 1952; Vergroesen et al., 2016, 2015). Therefore, future work will investigate the effect of degeneration on time-dependent recovery mechanics with osmotic pressure.

There are conflicting data in the literature about achieving full disc height recovery *in vitro* (Johannessen et al., 2004; Kingma et al., 2000; Koeller et al., 1984; Solomonow et al., 2000; van der Veen et al., 2007). Incomplete disc height recovery observed in this study for the control group agrees with the results of previous studies (O'Connell et al., 2011; van der Veen et al., 2007); however, the findings reported here demonstrate that osmotic pressure can be used in combination with low mechanical loading to achieve full disc height recovery *in vitro*. In conclusion, osmotic pressure causes significant changes in time-dependent recovery response of healthy discs. This study provides a better understanding of disc rehydration mechanisms and will be important for understanding diurnal recovery of healthy, injured, and degenerated discs.

5. Nonlinear stress-dependent recovery behavior of the intervertebral disc

5.1. Introduction

The intervertebral disc provides spinal stability and mobility while sustaining large mechanical loads. Complex disc mechanics originate from its heterogeneous structure, inherent viscoelasticity, and interstitial fluid-matrix interactions (Cassidy et al., 1990; Costi et al., 2008; Hayes and Bodine, 1978). The disc consists of a gel-like nucleus pulposus surrounded by the annulus fibrosus, which has a multi-layered angle-ply structure. Despite differences in composition and structure, water is the primary constituent of both tissues (> 65% by wet weight) (Antoniou et al., 1996; Iatridis et al., 2007). Moreover, the water content fluctuates by 15 – 25% during a diurnal cycle, with region-dependent differences in water loss (Botsford et al., 1994; Martin et al., 2018; McMillan et al., 1996). Disc mechanical properties are sensitive to hydration, which is altered by changes in tissue porosity, proteoglycan content, or osmotic differential between the tissue and surrounding environment (Bezci et al., 2015; Werbner et al., 2019). Furthermore, load-induced fluid flow enhances the transport of large solutes through the disc (Ferguson et al., 2004; Urban et al., 1982). Thus, maintaining sufficient fluid flow into the disc during low loading periods is essential for maintaining healthy disc function and cell viability.

Measurable changes in disc height during diurnal loading or signal intensity of magnetic resonance images provide an indirect measure of intradiscal fluid movement (Martin et al., 2018). Mechanically, the disc responds to changes in load by undergoing an instantaneous elastic deformation followed by a time-dependent deformation (Kazarian, 1975). Previous *in vitro* studies used various empirical models to describe time-dependent deformation under creep, stress relaxation, and recovery (Bezci and O'Connell, 2018; Burns et al., 1984; Johannessen et al., 2004; Keller et al., 1990, 1987; O'Connell et al., 2011; Riches et al., 2002; Van der Veen et al., 2013; Vergroesen et al., 2018). Although rheological models simplify complex deformations into one-dimensional measurements, they have been useful for evaluating the effects of loading history, hydration, injury, and degeneration on time-dependent behavior (Bezci and O'Connell, 2018; Burns et al., 1984; Campana et al., 2011; Cassidy et al., 1990; Hult et al., 1995; Johannessen et al., 2004; Keller et al., 1990, 1987; Martin et al., 2013; O'Connell et al., 2011; Pollintine et al., 2010; Vergroesen et al., 2018).

Mechanical loading forces water out of the disc during loading. However, fluid flow into the disc during bed rest or low-loading recovery is partially driven by the osmotic difference between the tissue and surrounding environment (Bezci and O'Connell, 2018). As a result, time-dependent deformations in creep occur at a different rate than recovery (MacLean et al., 2007). Recovery tests are often performed under a nominal load to mimic bed rest recovery, which is predicted to be near 0.06 MPa for human discs (~100 N for L4L5 human discs) (Dreischarf et al., 2016; Ferguson et al., 2004; O'Connell et al., 2007b; Schmidt et al., 2016b; Vergroesen et al., 2014; Wilke et al., 1999). Recently, osmotic loading has been used to drive fluid flow in glycosaminoglycan-rich tissues without altering the applied load (Kelly et al., 2013; Vergroesen et al., 2016). Our previous work showed that recovery in a hyperosmotic environment (*i.e.*, 1.5 M saline or 10x standard concentration) resulted in a shift in fluid flow during unloaded recovery

(Bezci and O'Connell, 2018). During recovery in the hyperosmotic environment, fluid flow switched from flowing into the disc, which was noted by an increase in disc height, to flowing out of the disc (observed as a decrease in disc height).

To date, most studies refer to apparent time-dependent behavior as viscoelasticity, although time-dependent disc mechanics have contributions from both inherent fluid-independent viscoelasticity and fluid-dependent poroelasticity (Bezci and O'Connell, 2018). Inherent viscoelasticity is often associated with stretching and sliding motion of collagen fibrils, while poroelasticity is attributed to the flow of mobile water through the porous tissue matrix (Argoubi and Shirazi-Adl, 1996; Oftadeh et al., 2018; Xu et al., 2013). Previous studies suggested that poroelasticity dominates disc mechanics at long time scales, while viscoelastic effects are present at short time scales, providing partial recovery of disc height within minutes of unloading before poroelastic effects come into play (Bezci and O'Connell, 2018; Hsieh et al., 2005; Lu and Hutton, 1998; Vergroesen et al., 2016). This observation has also been noted for other biological tissues, such as brain and articular cartilage (Budday et al., 2017; DiSilvestro et al., 2001; Suh and Disilvestro, 1999; Zhu et al., 1993).

The magnitude of compressive stress applied to the disc varies in magnitude with changes in body posture, body weight, muscle activity, and external loads (Callaghan et al., 1998; Han et al., 2013; Nachemson, 1981; Wilke et al., 1999). For example, stresses on the disc while lifting an object in forward flexed posture are up to four times greater than the stress experienced during standing (Nachemson, 1981; Wilke et al., 1999). In most studies that have evaluated disc recovery behavior, a single load condition has been considered, making it difficult to compare findings across studies (Bezci and O'Connell, 2018; Castro et al., 2014; Choy and Chan, 2015; Johannessen et al., 2004; O'Connell et al., 2011; Riches et al., 2002; van der Veen et al., 2007; Vresilovic et al., 2006). Therefore, the objective of this study was to quantify unloaded disc recovery behavior after creep loading under a wide range of physiologically relevant stresses.

5.2. Materials and methods

5.2.1. Sample preparation

Bovine caudal discs were used based on similarities to non-degenerate human discs with respect to mechanical and biochemical properties (Beckstein et al., 2008; Bezci et al., 2018b; Demers et al., 2004; Showalter et al., 2012). Moreover, bovine caudal discs from the upper tail have large disc areas and heights in comparison to other animal discs, making it an attractive animal model for investigating fluid flow and solute diffusion (Alini et al., 2008). Fresh-frozen ox tails were purchased from a local abattoir, and the surrounding musculature was removed with a scalpel (15 spines; age range = 16 – 18 months). Bone-disc-bone motion segments were prepared from the top two levels of the caudal spine by making parallel cuts through the superior and inferior vertebral bodies with a bone saw (n = 20; levels C1 – C3). Vertebral bodies were embedded in polymetheylmethacrylate (PMMA) dental cement to ensure that the loaded surfaces were parallel with the mid-transverse plane of the disc. Each motion segment was wrapped with a saline-soaked gauze (0.15 M phosphate-buffered saline) and stored at -20°C until testing.

Before testing, specimens were hydrated in 0.15 M phosphate-buffered saline at 4°C for 24 hours and then equilibrated to room temperature for 2 hours to ensure steady-state hydration levels for all samples.

5.2.2. Mechanical testing

First, a preliminary study was performed to determine the repeatability of disc recovery behavior, because previous work demonstrated that creep behavior was not repeatable, even after extended recovery (Bass et al., 1997; O'Connell et al., 2011). A nominal compressive preload (10 N) was applied to ensure contact between the specimen and loading platens. Then, each specimen (n = 8) underwent two cycles of creep-recovery loading, where each cycle consisted of a 24-hour creep at 1200 N, followed by an 18-hour recovery period at 10 N (Figure 19A). Based on the intradiscal pressure of human lumbar discs, the pressure that corresponds to 10 N may be slightly lower than the pressure experienced during bed rest (i.e., lying supine) (Dreischarf et al., 2016; Wilke et al., 1999). Compression testing was performed at room temperature using a servo-hydraulic material testing system equipped with a saline bath to maintain hydration during testing (Figure 19A; MiniBionix 858, MTS Systems Corp., Eden Prairie, MN). The saline solution (0.15 M phosphate-buffered saline) was refreshed at the beginning of each creep and recovery period.

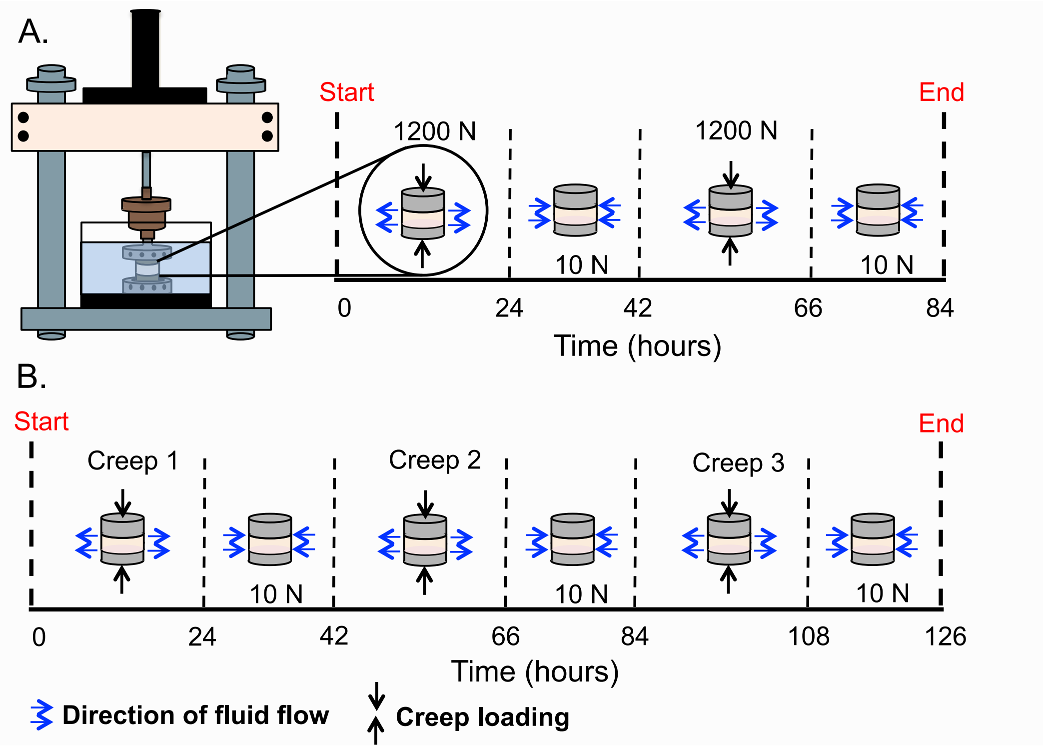

Figure 19: Schematic of experimental study design to evaluate (A) recovery behavior and (B) load-dependent recovery mechanics. Black arrows indicate compression applied to the motion segment. Blue arrows indicate expected fluid flow during each phase.

Once repeatable recovery behavior was confirmed, disc recovery mechanics were evaluated with respect to the applied compressive stress during creep. A nominal preload (10 N) was applied to ensure contact between the specimen and loading platens. Then, specimens underwent three cycles of creep-recovery loading, where each cycle consisted of a 24-hour creep at a pre-assigned load (100, 200, 300, 600, 900, or 1200 N; loading rate = 20 N/s), followed by an 18-hour recovery period at 10 N (Figure 19B; total testing time = 126 hours). The order of loading was randomized for each specimen. Changes in disc height were monitored for an extended period of time during unloaded recovery to improve predictions of the equilibrium recovery behavior (Van der Veen et al., 2013). Total testing time was limited to testing times used in previous studies with long-duration test protocols (Korecki et al., 2007; Vergroesen et al., 2018). A wide range of axial compressive loads was selected to represent the wide range of pressures experienced *in vivo* (*e.g.*, lying supine, relaxed standing, and lifting) (Wilke et al., 1999).

5.2.3. Data analysis

Force and displacement were recorded throughout the test (acquisition rate = 1 Hz). Changes in specimen height (or displacement) during recovery were calculated with respect to the disc height at the end of the previous loading period. Initial recovery rate was calculated from the slope of the displacement-time curve using the first 10 minutes of data. Similarly, the recovery rate at 18 hours was calculated by using the slope of the displacement-time curve using the data from the last hour of the testing. Time-dependent recovery behavior was evaluated by curve fitting displacement data to a 5-parameter rheological model, using a non-linear least-squares fitting algorithm (lsqnonlin function, Equation 2; Matlab, Mathworks, Inc., Natick, MA). In Equation 2, parameters τ_1 and τ_2 denote time constants for the fast (or short-term) and slow (or long-term) recovery responses, respectively. Parameters A_1 and A_2 denote asymptotic displacement limits due to fast and slow recovery responses, respectively. To simplify the model, the elastic response parameter, d_E, was fixed based on the displacement measured at the end of the unloading ramp.

$$d = d_E + A_1(1 - e^{-t/\tau_1}) + A_2(1 - e^{-t/\tau_2}) \tag{2}$$

The rheological model was used to predict equilibrium displacement (d_{eq}) and equilibrium time (t_{eq}) for recovery. Equilibrium time was calculated as the time when displacement reached 95% of the equilibrium displacement. Individual contributions of elastic, fast, and slow responses to disc recovery behavior were calculated as a percentage of equilibrium displacement (*i.e.*, total recovery response).

After mechanical testing, each motion segment was rehydrated in 0.15 M phosphate-buffered saline for an additional 24 hours before removing the disc from the surrounding vertebrae with a scalpel. A digital image of the transverse plane was taken to measure the cross-sectional area. Applied compressive stress was calculated by dividing the applied load by the cross-sectional area.

5.2.4. Statistics

To assess the repeatability of disc recovery behavior, a paired t-test was used to compare model parameters from the two recovery cycles. The relationship between applied creep stress and recovery model parameters was estimated by fitting each parameter to three functions, including linear, logarithmic, and power functions. The function with the lowest Akaike's Information Criterion (AIC) score was selected for further analyses. The AIC score was used to evaluate goodness-of-fit because the coefficient of determination (R^2) has been shown to be inappropriate for nonlinear models (Spiess and Neumeyer, 2010). When a nonlinear relationship was found, data were log-transformed to convert a nonlinear relationship to a linear one. For linear relationships, the coefficient of determination (R^2) was used to determine the strength of the correlation. R^2 values greater than 0.5 were defined as strong correlations, whereas moderate correlations were assumed for $0.3 \leq R^2 < 0.5$. Any R^2 values less than 0.3 were interpreted as weak correlations.

Mixed effects models were performed to evaluate the statistical significance of applied creep stress and creep-recovery cycle number using the restricted maximum likelihood method. Mixed effects models were chosen to incorporate both random (*i.e.*, specimen information) and fixed variables (*i.e.*, applied load and cycle number). The effect of replicate measurements from each disc and the spine that discs were collected from was evaluated by including disc level and associated animal donor number as nested random variables. All statistical analyses were performed using R software, and significance was assumed for $p < 0.05$.

5.3. Results

Force-displacement response during creep and recovery was nonlinear (Figure 20A). Creep behavior reached equilibrium within ~12 hours; however, disc height recovery did not reach equilibrium within the 18-hour period (slope = 0.59 ± 0.02 mm/h >> 0; Figure 20A). The rheological model fitted well to data collected during unloaded recovery (Figure 20B). Model parameters were compared between the two recovery cycles to assess the repeatability of recovery behavior and to ensure that damage did not occur during loading. Unlike the creep response, recovery behavior was highly repeatable with no significant differences in measured elastic and time-dependent displacements or model parameters between the two cycles ($p > 0.48$; Figure 20A).

For all compressive stresses, the recovery displacement-time curve was highly nonlinear, with a gradually decreasing rate of deformation (Figure 21A). The initial recovery rate ranged between 0.5 and 2.25 mm/h, and there was a nonlinear relationship between the recovery rate and the applied creep stress (Figure 21B). After 18 hours of recovery, the recovery rate was less than 0.10 mm/h and the 18-hour recovery period was insufficient to achieve equilibrium (Figure 21A & 21C). There was a slight nonlinear relationship between the initial displacement during recovery (*i.e.*, elastic recovery displacement) and the applied creep stress (Figure 21D). However, there was a stronger nonlinear relationship between time-dependent recovery displacement and the applied creep stress (Figure 21E), resulting in a strong nonlinear relationship between the equilibrium displacement during recovery and the applied creep stress

(Figure 21F). That is, the difference between recovery curves following 0.5 MPa and 1.0 MPa creep was greater than the difference between recovery curves following 1.5 MPa and 2.0 MPa creep (Figure 21A). As expected, cycle number did not impact elastic or time-dependent recovery displacements ($p > 0.5$).

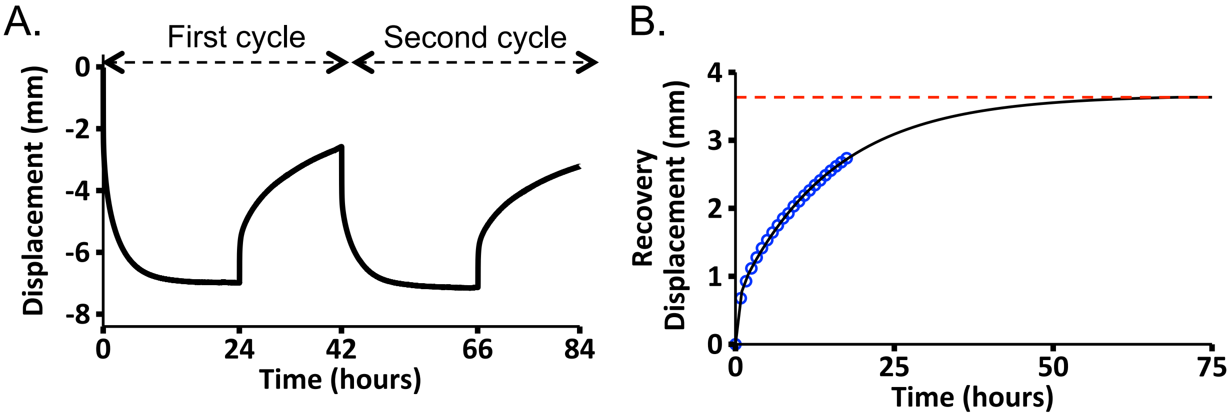

Figure 20: (A) Representative sample showing displacement during two cycles of creep and recovery. (B) Representative sample of axial displacement (or disc height) during recovery. Note that displacement was re-zeroed at the beginning of each loading period. Blue circles represent experimental data (every 50th point shown for clarity), the black line represents the model fit, and the dashed red line indicates equilibrium displacement. Recovery was measured for 18 hours, because preliminary work showed that 18-hour test was sufficient for predicting equilibrium displacement within 10 %.

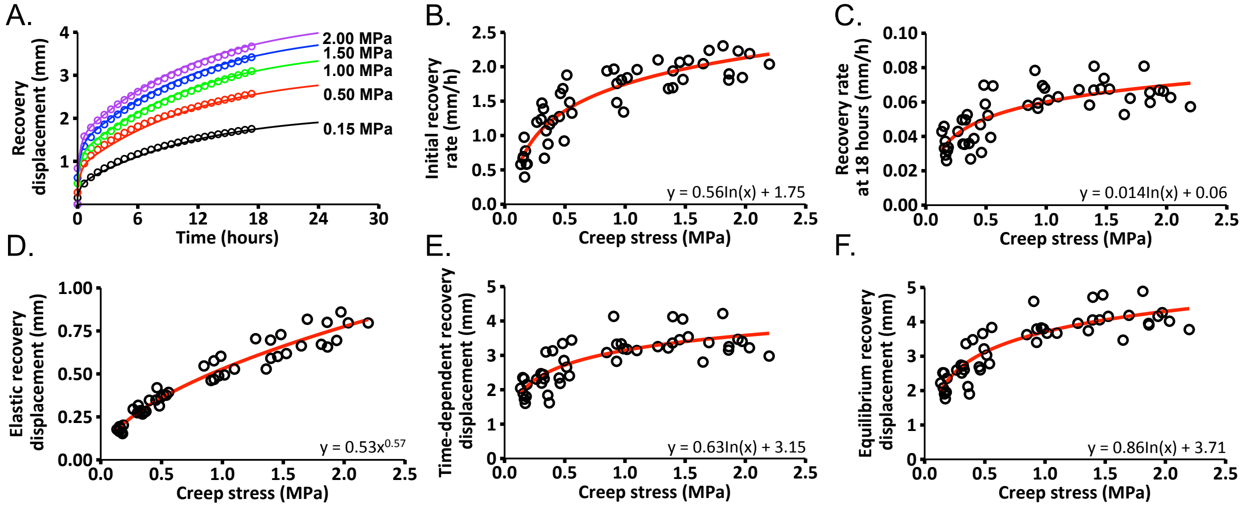

Figure 21: (A) Comparison of experimental recovery data and model predictions for different stress levels. Circles represent experimental data, and curves represent model predictions. Recovery rates at the (B) beginning and (C) end of the recovery period. Recovery displacement (D) measured immediately after unloading (*i.e.* elastic recovery), (E) during the length of the recovery period (*i.e.,* time-dependent recovery displacement), and (F) predicted recovery displacement at equilibrium. Note that the equilibrium recovery displacement is a summation of the elastic and time-dependent recovery displacements. Circles represent experimental data and red lines indicate nonlinear best-fit lines.

The relationship between asymptotic displacement limits for fast and slow recovery responses (*i.e.*, A_1 and A_2, respectively; Equation 2) and applied creep stress was nonlinear and best described with a logarithmic function ($p < 0.001$; Figure 22A-B). The magnitude of A_1 was an order of magnitude lower than the magnitude of A_2. In contrast, time constants associated with fast and slow recovery responses did not depend on applied creep stress ($p \geq 0.08$; Figure 22C-D). The fast time constant was on the order of minutes (range = 10 – 30 minutes), while the slow time constant was on the order of hours (range = 8 – 17 hours; Figure 22C *versus* 22D).

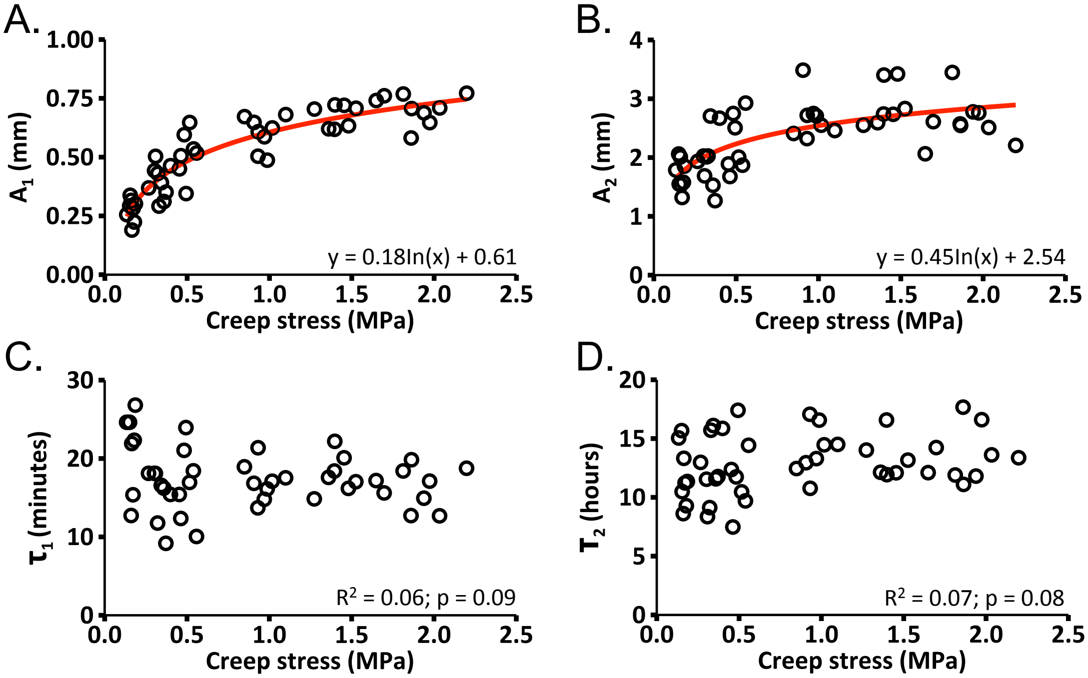

Figure 22: (A-B) Asymptotic limits of displacement due to (A) fast and (B) slow recovery behaviors. (C-D) Time-constants associated with (C) fast and (D) slow recovery behavior. Circles represent experimental data and red lines indicate logarithmic or linear best-fit lines.

In order to account for differences in recovery displacement due to the applied creep stress, the 5-parameter rheological model was modified to incorporate the applied stress (Equation 3), where t represents time (seconds) and σ represents applied stress (MPa) during recovery. Model parameters shown in Equation 3 represent average values for all specimens (*i.e.*, the combination of relationships shown in Figures 21D, 22A, and 22B). The modified 5-parameter rheological model well described disc recovery behavior with a single set of model parameters, regardless of applied stress during loading (Figure 21A – circles versus lines).

$$d = 0.53x^{0.57} + (0.18\ln x + 0.61) * (1 - e^{-t/1176}) + (0.45\ln x + 2.54) * (1 - e^{-t/43200}) \qquad (3)$$

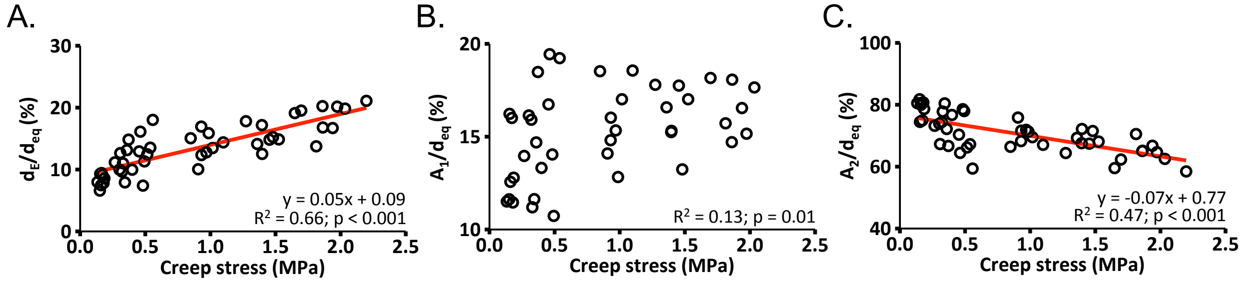

Figure 23: Percent contribution of (A) elastic, (B) fast, and (C) slow responses to equilibrium recovery displacement. Circles represent experimental data and red lines indicate linear best-fit lines.

Equilibrium recovery time was 36 ± 7 hours and did not depend on applied creep stress ($p = 0.08$). However, the contributions of elastic, fast, and slow recovery responses to the overall equilibrium displacement significantly depended on applied creep stress ($p < 0.01$; Figure 23A-C). The contribution of the elastic response to the overall equilibrium displacement was strongly correlated with the applied creep stress ($R^2 = 0.66$; Figure 23A). Similarly, there was a significant, but weak, positive correlation between the contribution of the fast time-dependent response to the overall recovery behavior and applied creep stress ($R^2 = 0.13$; Figure 23B). Disc height recovery associated with slow time-dependent response accounted for more than 50% of the overall recovery displacement, regardless of the applied creep stress. Moreover, there was a moderate negative correlation between the contribution of the slow time-dependent response and applied creep stress ($R^2 = 0.47$; Figure 23C). For low stresses (~0.1 MPa), elastic and fast time-dependent behaviors accounted for ~20% of the overall disc height recovery, whereas slow time-dependent behavior accounted for ~80% of the overall disc height recovery. However, as the applied creep stress increased (*e.g.,* ~2 MPa), the contribution of elastic and fast time-dependent responses increased to ~35%, while the contribution of slow time-dependent response decreased to ~65%.

5.4. Discussion

The objective of this study was to characterize the stress-dependent recovery behavior of the intervertebral disc, based on previous observations that noted differences in disc recovery mechanics with loading history (Hwang et al., 2012; O'Connell et al., 2011; Schmidt et al., 2016b; van der Veen et al., 2007). Repeatable measurements of mechanical properties are important for eliminating confounding effects of loading history in studies that employ repeated-measures test protocols. Hence, we first confirmed that the observed recovery behavior was repeatable before evaluating the effect of loading history on recovery mechanics. We found different time-dependent behaviors between the first and second creep cycles, in agreement with previous findings (O'Connell et al., 2011; van der Veen et al., 2008). Despite differences in creep behaviors, identical recovery responses were observed during the two recovery cycles. Similar observations have been reported for ovine and porcine discs subjected to three creep-recovery cycles with shorter loading and recovery periods (*i.e.,* 15 minutes of loading and 30 minutes of recovery) (van der Veen et al., 2008, 2007). The discrepancy between creep and recovery repeatability may be due to over-hydration of *in vitro* specimens before testing, resulting in greater fluid flow during the first creep cycle, where fluid flow exchange reaches a steady-state response after the third creep-recovery cycle (Dhillon et al., 2001; Velísková et al., 2018).

The intervertebral disc is a composite material that exhibits both poroelastic and viscoelastic behaviors. Differences in the porosity of the nucleus pulposus and annulus fibrous give rise to anisotropy in ion diffusivity and fluid flow throughout the disc (Gu et al., 2004; Jackson et al., 2006; Sélard et al., 2003; Urban et al., 1977). During compression, much of the initial response is absorbed by water in the tissue. However, over time, compression forces fluid to flow out of the tissue, resulting in pore compaction and additional stress being absorbed by the viscoelastic solid (Chagnon et al., 2010). Dehydration during loading has been observed to cause shrinkage of collagen fibers, which may contribute to time-dependent changes in disc mechanics (Andriotis et al., 2018). In addition, fluid flow out of the disc increases fixed charge density and internal osmotic pressure, causing a pressure gradient with the external environment (Gray et al., 1988). The findings from this study suggest that greater osmotic gradients caused by larger compressive loads resulted in an increase in fluid flow rate and magnitude during recovery. This finding also agrees with observations of our previous work, where greater disc height recovery was achieved by performing recovery under a hypo-osmotic condition, which increases the osmotic gradient between the disc and surrounding environment (Bezci and O’Connell, 2018).

We used a five-parameter rheological model, consisting of two exponential terms, to characterize the time-dependent disc recovery behavior. As expected, a bi-exponential model provided a better fit to the experimental data than a single exponential model. The choice of using a bi-exponential model was also based on findings from previous studies that identified changes in short-term (minutes) or long-term (hours) disc recovery mechanics with nucleotomy, degeneration, and osmotic loading (Bezci and O’Connell, 2018; O’Connell et al., 2011; Vresilovic et al., 2006).

Although multiple mechanisms coexist during time-dependent deformation, short-term recovery has been predominantly associated with intrinsic viscoelasticity, rather than fresh fluid being imbibed by the disc through the annulus (Bezci and O’Connell, 2018; Broberg, 1993; O’Connell et al., 2011; van der Veen et al., 2005). In our previous work, altering the external osmotic loading environment only influenced the long-term recovery behavior, where fluid exchange with the surrounding environment is slower than the viscoelastic recovery of the solid matrix or fluid redistribution within the disc (Bezci and O’Connell, 2018). Moreover, previous studies did not observe any increase in nucleus pulposus pressure and fluid content during the first 30 minutes of recovery, which is comparable to the time constant of the short-term recovery response reported here (Reitmaier et al., 2012; van der Veen et al., 2005). Lastly, tests on desiccated discs showed that creep and recovery were possible without water movement (Koeller et al., 1984), which was further supported by our findings that discs exhibited a nonlinear recovery response in air, without any signs of dehydration over an 18-hour recovery period (Figure S1). Collectively, these findings suggest that recovery response on the order of minutes is largely driven by the viscoelastic response of the solid matrix. In contrast, long-term time-dependent recovery behavior has contributions from both intrinsic viscoelasticity and fluid flow.

Asymptotic displacement limits for short- and long-term recovery responses increased with creep stress, while associated time constants and predicted equilibrium time were insensitive to creep stress. Our finding was in agreement with observations for rat discs, where recovery time constant did not change with creep stress (from 0.5 MPa to 2.0 MPa) (MacLean et al., 2007). However, the initial recovery rate, associated with short-term recovery, was ~4 times greater following compression at 2.0 MPa than compression at 0.1 MPa. The increased rate of initial recovery following larger compressive forces may allow for greater recovery to occur within the same time frame as recovery following low compressive stresses. This finding has potential clinical importance, as it suggests 8 hours of bed rest might be sufficient for discs to achieve identical hydration levels, regardless of loading history.

The instantaneous and time-dependent recovery deformations were nonlinearly related to compressive stress, highlighting the nonlinear "viscoelastic" behavior of the intervertebral disc. The nonlinear viscoelastic mechanical behavior was expected based on observations on tendons, ligaments, and vascular tissues (Hingorani et al., 2004; Peña et al., 2011; Provenzano et al., 2001; Troyer and Puttlitz, 2011). Changes in recovery deformation were more pronounced at low compressive stresses, but the increase in recovery deformation diminished after compression at higher stresses (*e.g.*, recovery response following 1 MPa of creep). This complex behavior cannot be comprehensively described by commonly used linear or quasi-linear viscoelastic formulations with constant model parameters. This work showed that a modified five-parameter rheological model with stress-dependent coefficients was adequate for describing recovery behavior following a wide range of compressive stresses (Equation 3).

The relative contributions of elastic and time-dependent responses to disc height recovery were sensitive to load magnitude. Elastic and fast time-dependent responses represented 20 – 40% of the total recovery deformation. However, the relative contribution of the elastic response increased, while the relative contribution of slow time-dependent response decreased linearly with increasing creep stress. This finding suggests that tissue elasticity may become more important for disc height recovery from loading at larger compressive stresses. Increased loading on the spine, such as in professions that require sustained heavy loads (*e.g.,* factory workers or military personnel), might alter disc recovery behavior and limit the convective transfer of nutrients and metabolites necessary for cellular function.

This study is not without its limitations. First, we chose to use a 5-parameter rheological model to conduct a quantitative assessment of early and late stages of recovery and to make comparisons between tests with different loading magnitudes. However, an ideal constitutive model should describe multiple loading and recovery phenomena with a single set of model parameters. Second, we only investigated recovery behavior under static compression. However, physiological loading is more complex, including dynamic and six degrees of freedom loading (Amin et al., 2016; Bezci et al., 2018a). However, previous work observed similar time-dependent behaviors between dynamic and static loading conditions (van der Veen et al., 2007). Hence, overall trends reported in this study for static loads are expected to be similar to the trends observed for dynamic loads. Lastly, disc mechanics are sensitive to many factors, including loading rate, loading duration, hydration state, spinal level, specimen age, and degeneration (Bezci et al., 2015; Keller et al., 1987; Kemper et al., 2007; Newell et al., 2017; Przybyla et al., 2007). Our study design aimed to minimize the impact of these factors, but differences in test protocols (*e.g.*, loading duration) between this study and previous studies made it difficult to directly compare results, which remains to be a significant challenge in the field (MacLean et al., 2007; van der Veen et al., 2007).

In conclusion, both short- and long-term time-dependent recovery behaviors strongly depend on loading history, in particular, the magnitude of applied compression. The findings of this study highlight the complexity of load-dependent fluid flow kinematics during recovery and support the notion that multiple recovery mechanisms contribute to disc height recovery during low loading periods, such as bed rest. Findings from this work, together with previous findings, suggest that short-term recovery is primarily driven by the viscoelastic response of the solid matrix, while long-term recovery response is driven by both intrinsic viscoelasticity and fluid flow, which is driven by the osmotic gradient between the disc and surrounding environment. To better understand the effect of both recovery mechanisms and fluid redistribution between the nucleus pulposus and annulus fibrosus, more complex three-dimensional models and experimental studies are needed.

5.5. Supplemental material

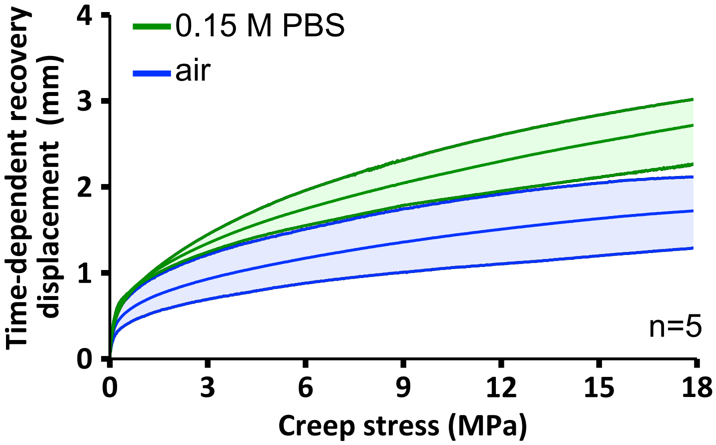

Figure S1: Comparison of time-dependent recovery behavior in 0.15 M PBS (green) and air (blue; n = 5 per condition). Shaded areas represent the difference between the tests that exhibited maximum and minimum displacements during recovery. Discs in both experimental groups were subjected to a 24-hour creep at 1200 N, followed by an 18-hour recovery at 10 N. Creep was performed in 0.15 M PBS, while recovery was allowed in either 0.15 M PBS or air.

6. Time-dependent swelling behavior of the bovine caudal disc

6.1. Introduction

The intervertebral disc is an avascular heterogeneous composite structure, comprised of the nucleus pulposus (NP), a soft hyperelastic material that represents 40-50% of the disc volume, which is circumferentially encapsulated by the stiffer annulus fibrosus (AF) (Iatridis et al., 2007; O'Connell et al., 2007b). Tissue composition varies spatially throughout the disc, with water accounting for 70-85% of the tissue's wet weight (Antoniou et al., 1996; Cortes et al., 2014; Iatridis et al., 2007). Moreover, both tissues have a tendency to absorb water and increase its volume by more than 50% (Bezci et al., 2019, 2015; Urban and Maroudas, 1981). The NP has higher water content and swelling capacity than the AF, and previous studies have associated differences in water content and swelling capacity to the higher concentration of negatively charged glycosaminoglycans (GAGs) in the NP (Bezci et al., 2015; Perie et al., 2006; Urban et al., 1979). Previous tissue-level experiments either examined relative differences in swelling capacity of the two disc regions at a single time point or tested explant structures that did not replicate *in situ* boundary conditions (*e.g.,* annular ring versus AF explant) (Bezci et al., 2019, 2015; Cortes et al., 2014; Oftadeh et al., 2018; Tavakoli, 2017; Urban and Maroudas, 1981). Hence, these findings provide limited understanding of the complex fluid-flow kinematics throughout the disc.

Mechanical loading causes complex deformations that induce interstitial fluid redistribution within the disc and fluid flow across the boundaries at the annulus periphery and endplates. Intradiscal pressure increases as disc absorbs water and regains disc height during low loading conditions (Bezci and O'Connell, 2018; Reitmaier et al., 2012; Vergroesen et al., 2014). Direct measurement of fluid distribution within the disc is challenging. Hence, recent research used quantitative magnetic resonance imaging to measure regional changes in intradiscal water content with diurnal loading. Joint-level *in vitro* studies monitor disc height or intradiscal pressure to indirectly determine the direction, magnitude, and rate of fluid flow during physiological loading conditions. These studies observed differences in fluid-flow kinematics with osmotic loading, loading conditions (*i.e.*, mode, magnitude, rate and frequency), age, and degeneration (Bezci and O'Connell, 2018; MacLean et al., 2007; O'Connell et al., 2011; van der Veen et al., 2007). However, these observations were limited to the changes for the entire bone-disc-bone motion segment, providing a lack of understanding of mechanisms for complex intradiscal fluid flow behavior during recovery. Recent advancements in image-processing algorithms have made optical, non-contact measurement techniques appealing for investigating local tissue strains.

Swelling capacity and swelling-induced tissue deformations highly depend on the boundary conditions (Yang and O'Connell, 2019). Healthy discs hydrated after removal of the endplates and vertebral bodies experience a 50-60% increase in tissue weight, and the relative effect of the endplate boundary condition decreases with degeneration due to decreased swelling capacities of both the NP and inner AF (Jim et al., 2011; Yang and O'Connell, 2019). The effect of boundary condition is greater for tissue explants, where testing NP-only specimens results in significant increases in tissue weight under stress-free boundary conditions (Bezci et al., 2015).

Specifically, the swelling ratio, defined as the increase in tissue weight (or volume) due to swelling divided by the initial weight (or volume), decreases linearly from 1.85 at the disc center (*i.e.,* 185% increase in NP tissue weight) to 0.5 in the outer AF (Bezci et al., 2019).

Fluctuations in water content due to diurnal loading or compositional changes with degeneration play an important role in intradiscal strain distributions during loading (Botsford et al., 1994; Martin et al., 2018). Low tissue permeability hinders fluid flow, making disc height recovery a slow time-dependent process that is dependent on loading history and the osmotic differential between the tissue and surrounding environment (Bezci and O'Connell, 2018; O'Connell et al., 2011; Schmidt et al., 2016b). As a result, discs *in vivo* and *in vitro* can achieve different levels of hydration, which affect relative joint stiffness (Bezci et al., 2015; Schmidt et al., 2016b). Despite numerous joint-level studies that investigated the time-dependent fluid-flow behavior, there is limited information about swelling-induced intradiscal strain distributions with respect to swelling time and boundary conditions. Therefore, the objective of this study was to investigate time-dependent swelling behavior of the intervertebral disc *ex situ.*

6.2. Materials and methods

Two separate experiments were performed to evaluate time-dependent swelling behavior of the intervertebral disc *ex situ*. The first objective was to investigate free-swelling behavior of the whole disc and disc subcomponents separately (*i.e.*, AF- or NP-only explants; Figure 24A). The second objective was to evaluate the effect of swelling boundary conditions on in-plane strain distributions of intact discs and discs with the NP removed (annular rings; Figure 24B). The first group consisted of AF rings in contact with saline at the outer periphery and at the center of the annular ring (Figure 24B – left, blue arrows). The second group included AF rings in contact with saline solution only at the outer periphery. Finally, the third group included intact discs in contact with saline at the outer periphery.

Fresh-frozen bovine tails were obtained from a local abattoir (13 spines, age: 16-18 months) and defrosted in 0.15 M phosphate-buffered saline solution (PBS) at room temperature. Following the removal of surrounding musculature and ligaments, bovine discs were isolated from the adjacent vertebrae with a scalpel and only the top three levels were used for testing (C2 – C4). Discs were visually examined for signs of damage (damage observed in 4 / 42 discs). Intact, healthy discs were selected, wrapped with a saline-soaked gauze and stored frozen at -20°C.

6.2.1. Free-swelling Experiment

Prior to testing, discs were thawed at room temperature. NP sections were harvested from the disc center with a biopsy punch (diameter = 10 mm; Figure 24A). Residual NP tissue was removed from the AF ring with a scalpel. Free-swelling behaviors of the intact discs, AF rings, and cylindrical NP explants were investigated by immersing samples in 0.15 M PBS for 16 hours (n = 7 per group). To quantify swelling, tissue wet-weight was measured before swelling. Specimens were weighed every 15 minutes during the first two hours of swelling and weighed hourly after the initial two-hour period. Before measuring sample weight, excess surface water was removed by gently blotting the tissue with a kimwipe.

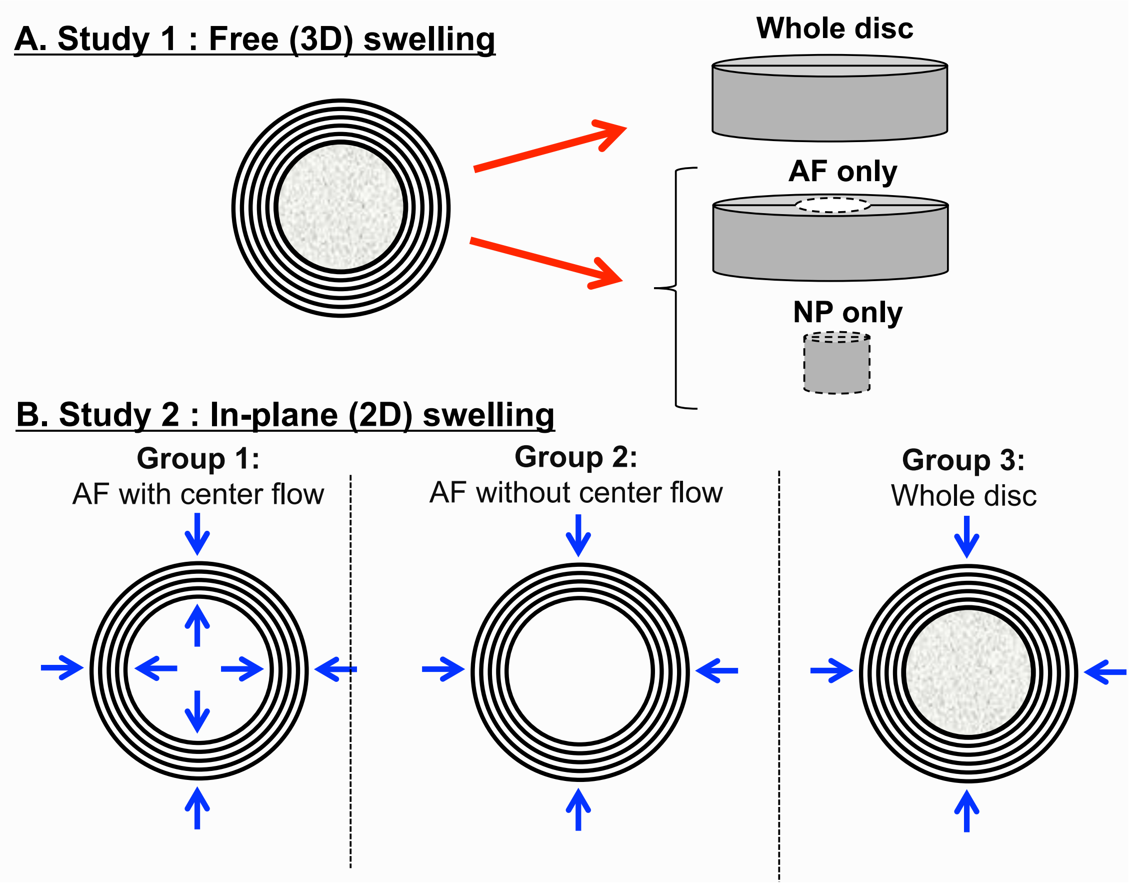

Figure 24: Study design for (A) free (3D) and (B) in-plane (2D) swelling experiments. Blue arrows represent expected fluid flow due to contact from saline solution.

The swelling ratio (Q) was calculated the change in tissue weight during swelling with respect to initial wet weight divided by the initial wet weight and reported as a percent (*i.e.*, Q = 100 x (m_i – m_o)/m_o). A stretched exponential function was used to describe swelling ratio as a function of time (Equation 4), where model parameter Q_{eq} represents equilibrium swelling ratio (unitless), τ is the time constant (hours), and β is the stretch parameter to describe nonlinearity (unitless; bounded between 0 and 1) (Van der Veen et al., 2013).

$$Q(t) = Q_{eq}(1 - e^{-(t/\tau)^{\beta}}) \tag{4}$$

6.2.2. In-plane (2D) Swelling Experiment

For 2D in-plane swelling experiments, parallel surfaces were created with a temperature-controlled freezing stage microtome (n = 8-9 per group; Leica SM2400, Leica Biosystems Inc., IL, USA). After obtaining parallel surfaces, sample height was measured using a digital caliper and specimens were thawed at room temperature for speckle patterning. For AF ring specimens, the NP was removed with a scalpel. To facilitate the digital image correlation (DIC) analysis, India ink was airbrushed onto the top surface to create a speckle pattern (Figure 25). A nozzle diameter of 0.3 mm was chosen to obtain an average speckle size exceeding the image pixel size by a factor of 3 – 5 (Lionello and Cristofolini, 2014; Zhou et al., 2016).

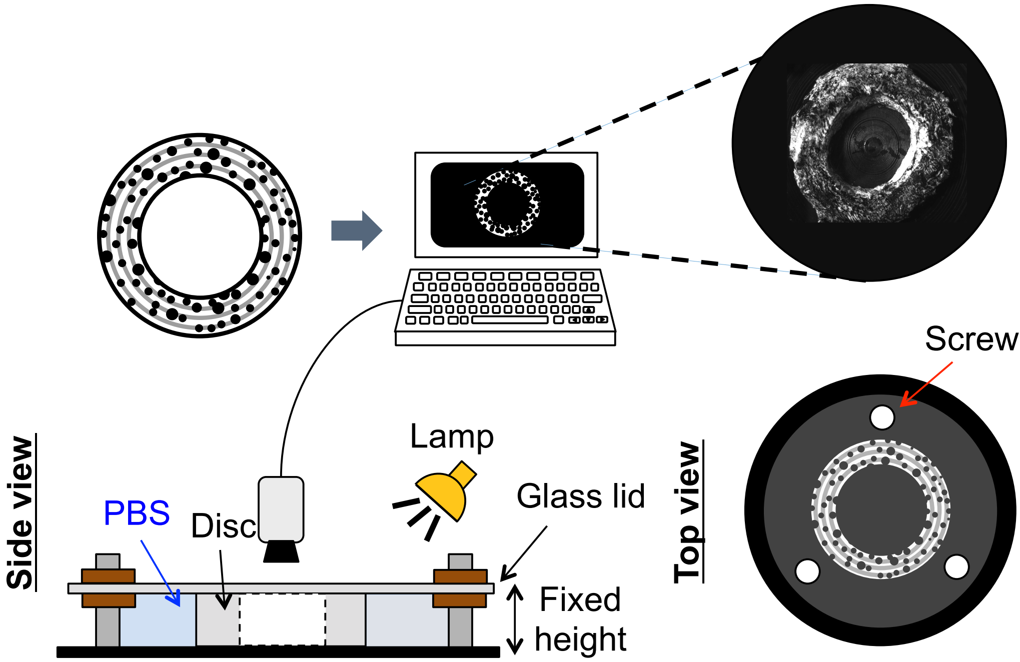

Figure 25: Schematic of experimental set-up for in-plane (2D) swelling experiments. A speckle pattern was applied to the top surface of the whole discs and AF rings before submerging them in saline for 16 hours. Disc height was fixed to avoid out-of-plane motion.

2D planar swelling experiments were performed in a custom-built swelling chamber filled with 0.15 M PBS (Figure 25). An adjustable lamp was used for illumination during testing. To perform 2D strain analyses, swelling in the z-direction (out-of-plane motion) was restricted with a transparent glass lid (thickness = 2.45 mm, mass = ~20 g; Figure 25 – side view). Screws to affix the glass lid were evenly spaced and the height of the lid was secured using nuts (120° apart; Figure 25 – top view).

A digital monochrome camera equipped with a 75 mm lens was used to acquire images for 16 hours (Fujifilm, USA, 1 frame/minute; 1920x1200 pixels, Grasshopper3 USB3, Model: GS3-U3-23S6M-C; FLIR Systems, Inc., USA). DIC analysis was performed using commercial software to calculate in-plane displacements (Δx and Δy) and Lagrangian strains (ε_{xx}, ε_{yy}, and ε_{xy}) (subset size = 111 pixels, step size = 5 pixels, incremental correlation; Vic-2D, Correlated Solutions Inc., Columbia SC). DIC data were post-processed using a custom-written MATLAB algorithm (Mathworks Inc, Natick MA). First, the disc edge and the boundary between the NP and AF were manually selected (O'Connell et al., 2007b). Based on the boundary selection, disc center and cross-sectional area were calculated and DIC data for pixels located outside of the disc edge were discarded from further analysis. To remove any outliers, principal strains that were ±3 standard deviations away from the mean were eliminated (~5%). Next, radial displacement was calculated for each pixel by calculating the difference between the final and initial radial locations with respect to the origin, which was defined as the disc center. Strain components (ε_{xx}, ε_{yy}, and ε_{xy}) were transformed from Cartesian to polar coordinates using the rotation of axes (radial strain: ε_{rr}, circumferential strain: $\varepsilon_{\theta\theta}$, and shear strain: $\varepsilon_{r\theta}$).

Test specimens were digitally segmented to identify the region-specific differences in swelling behavior. In all three experimental groups, the AF was divided into three concentric rings with equal thickness to describe region-dependent strains in the inner AF (IAF), middle AF (MAF) and outer AF (OAF). For intact discs, the NP was analyzed as a single region of interest. Mean radial and circumferential strain values were calculated for each region.

6.2.3. Water content analysis

6.2.3.1. Gravimetric water content measurement

After swelling experiments were completed, test specimens were freeze-dried in a lyophilizer for 72 hours to measure specimen dry weight. For intact discs in free-swelling experiments, the NP was separated from the AF using a scalpel. The NP explants and AF rings obtained from the intact discs were weighed to measure swollen tissue weight and freeze-dried separately to make comparisons with the water content measurements for tissue explants. Water content of the test specimens in this study was calculated as the difference between the swollen wet weight and dry weight normalized by dry weight. For specimens in the 2D swelling experiment, a 4 mm biopsy punch was used to obtain cylindrical tissue samples from the inner NP (INP) and the outer NP (ONP). Additionally, AF tissue strips with dimensions of 4 mm x 2 mm along the sample thickness were acquired from the inner AF and outer AF. The AF was separated into two regions for biochemical analysis, instead of three as in the swelling analyses, to compare post-swelling water content measurements with pre-swelling water content data previously reported by our laboratory (Bezci et al., 2019). Water content of the test specimens was calculated as the difference between the initial wet weight (WW) and dry weight (DW) normalized by initial wet weight or dry weight to compare results across data reported in the literature. Duplicate measurements for each NP or AF region were averaged for statistical analysis.

6.2.3.2. Raman-based water content measurement

Three NP and AF tissue samples were randomly chosen from the first study for qualitative assessment of swelling capacity using Raman spectroscopy (excitation at 632.8 nm; Horiba Jobin Yvon Labram spectrometer with Olympus BX41 confocal microscope). Raman spectra of each sample were collected in triplets over a frequency range of 2800 – 3800 cm^{-1}, and average spectra were calculated for the swollen NP and AF tissues. Representative spectra for swollen tissue samples were compared to spectra for bovine NP and AF samples before swelling (Bezci et al., 2019). Spectra were normalized to have the same intensity signal at 2945 cm^{-1}, which corresponded to the strongest CH vibrational line.

6.2.4. Statistics

All statistical analyses were performed in R (R Project for Statistical Computing, Vienna, Austria), with significance assumed for $p < 0.05$. For Study 1, time-dependent changes in the swelling ratio were reported for the 16-hour period. Swelling ratios of the intact disc, AF, and NP specimens were compared using a one-way analysis of variance (ANOVA). Pairwise comparisons were made between the NP and the AF, and between the AF and the whole disc. For Study 2, the average disc height and area were calculated for each experimental group and compared using a one-way ANOVA to ensure comparable disc geometry across groups. Mean strain values were calculated at 2, 8 and 16 hours of swelling. For each experimental group, a two-way ANOVA was performed to determine the effect of swelling time and region on swelling-induced strains. Additionally, a separate two-way ANOVA was conducted to assess the influence of the fluid boundary conditions on tissue strain for each annular region (factors = fluid boundary condition and annular region = IAF, MAF, and OAF). Whenever significance was detected, a Tukey post-hoc analysis was performed to compare groups.

Post-swelling water contents of the inner and outer NP were compared with previous pre-swelling water content data using an unpaired Student's t-test. Separate one-way ANOVA analyses were conducted for each AF region to assess differences in post-swelling water content across four different testing conditions. The Bonferroni correction method was used to account for multiple comparisons.

6.3. Results

6.3.1. Free-swelling experiment

Swelling ratio (Q) changed nonlinearly with time for all tissue types, and the majority of swelling was observed during the first 4 hours (Figure 26A). After 16 hours of free swelling, the final swollen weight of NP explants was 200% greater than the initial wet weight, while the final AF weight was 60% greater than the initial wet weight. Importantly, AF rings retained their ring shape during swelling. However, the additional boundary constraint of the AF onto the NP caused significant deformations along the axial direction during swelling, resulting in a disc that resembled a sewing thimble (Figure 26B).

The final water contents of the NP explants after swelling were 21.6 ± 2.9 g/g DW, which were 2.5 times higher than the values measured for the water content of the NP in intact discs (i.e., 8.5 ± 1.3 g/g DW). The final water content of the AF in intact discs was 30% lower than the water content of the AF rings (4.35 ± 0.26 g/g DW).

There was a significant difference in model parameters that described NP explant swelling compared to parameters that described AF swelling behavior ($p < 0.001$; Figure 26C). Specifically, the equilibrium swelling ratio (Q_{eq}) of NP explants was 2.7X greater than the AF Q_{eq} ($p < 0.001$; Figure 26C). Similarly, Q_{eq} of intact discs was 70% of the NP and was not statistically different from AF explants ($p = 0.4$). The time constant (τ) was lower for the NP than the AF, suggesting a higher swelling rate for the NP ($p < 0.001$). Due to the variation in τ for the whole disc, no significant differences were observed between the intact disc and tissue explants. The stretch parameter (β) for NP explants and intact discs was 20-40% greater than β for AF rings ($p < 0.03$)

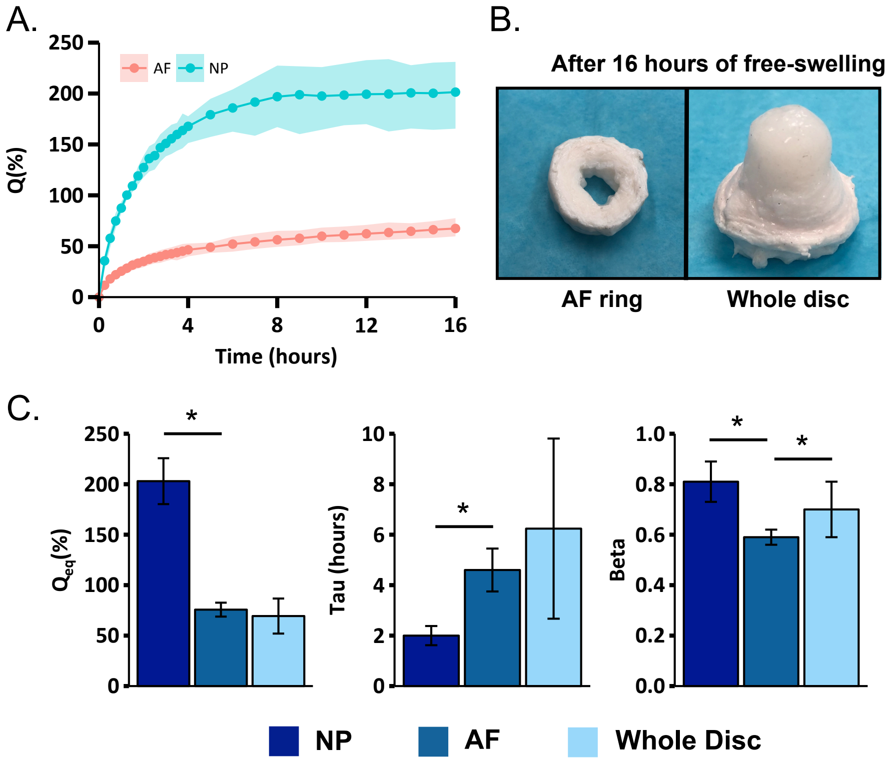

Figure 26: (A) AF (red) and NP (blue) swelling ratio throughout the 16-hour free swelling period. Shaded area represents the range (minimum to maximum) of experimental data. (B) Representative images of a swollen AF ring and intact disc. (C) Parameters for the stretched exponential function. Comparisons are made between the NP and the AF, and between the AF and whole disc. * Represents $p < 0.05$. Error bars represent one standard deviation.

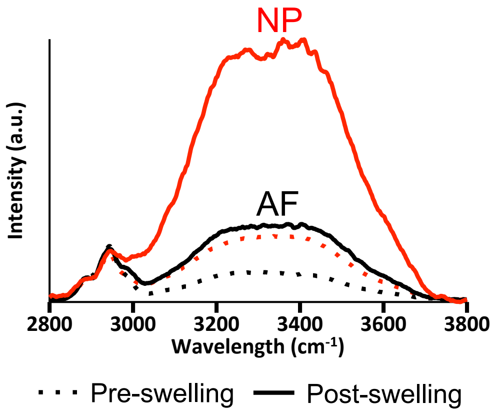

Figure 27: Comparison of Raman specta pre- (dashed lines) and post-swelling (solid lines) for the nucleus pulposus (NP; red lines) and annulus fibrosus (AF; black lines).

Raman spectra showed that the signal intensity for wavelengths above ~3000 cm^{-1} increased with swelling in both the NP and AF (Figure 27; solid versus dotted lines). Similar to observations from gravimetric measurements, change in signal intensity was greater for the NP than the AF (Figure 27; red versus black lines). After swelling, water spectrum (>3000 cm^{-1}) for the AF was similar to the spectrum for the NP before swelling.

6.3.2. In-plane (2D) Swelling Experiment

Discs used for the three experimental groups were comparable in height and area ($p > 0.5$, height = 5.40 ± 0.68 mm, area = 473 ± 58 mm^2). For AF rings, removed NP tissue corresponded to 51 ± 3% of the total area.

For AF rings with fluid flow from both the center and periphery, there was a nonlinear relationship between radial and circumferential strains with swelling time (Figure 28A-B; Group 1). In general, radial strains were an order of magnitude greater than circumferential strains. All AF regions experienced positive radial strains during swelling, with the magnitude of radial strains being highest in the inner AF for all time points ($p < 0.001$ for region; Figure 28A & 28C). There was a significant increase in average radial strains with swelling time for all AF regions ($p \leq 0.014$). After 16 hours, mean radial strain was approximately 0.65 mm/mm (or 65%) in the inner AF and 0.10 mm/mm (or 10%) for the outer AF (Figure 28C). Negative circumferential strains were observed in the inner AF, while positive circumferential strains were observed in the outer AF. Circumferential strains in the middle and inner AF did not change after 2 hours of swelling ($p \geq 0.2$) and after 8 hours in the outer AF. After 16 hours of swelling, the average circumferential strain was slightly compressive (-0.04 mm/mm or -4%) in the inner AF and slightly tensile (< 0.02 mm/mm or 2%) in the middle and outer AF (Figure 28D).

Restricting fluid flow to only the AF periphery greatly altered swelling behavior (Figure 28C-D *versus* Figure 29A-B). Similar to the AF rings in Group 1, radial and circumferential strains for AF rings in Group 2 increased with time. As expected, the greatest changes in swelling behavior was observed in the inner AF, where radial strains decreased from 0.65 mm/mm in Group 1 to ~0.07 mm/mm when fluid was absent (90% decrease; Figure 28C versus 29A). Therefore, peak radial and circumferential strains in Group 2 occurred in the outer AF (Figure 29A-B). The behavior of circumferential strains with respect to annular region was not affected by the change in fluid flow. That is, circumferential strains in the inner AF were slightly negative, while circumferential strains in the outer AF were positive (Figure 29B). Radial and circumferential strains in the outer AF were stable after 2 hours of swelling ($p \geq 0.09$). In contrast, inner AF radial and circumferential strains at 16 hours were greater than strains measured after 2 hours of swelling ($p < 0.05$).

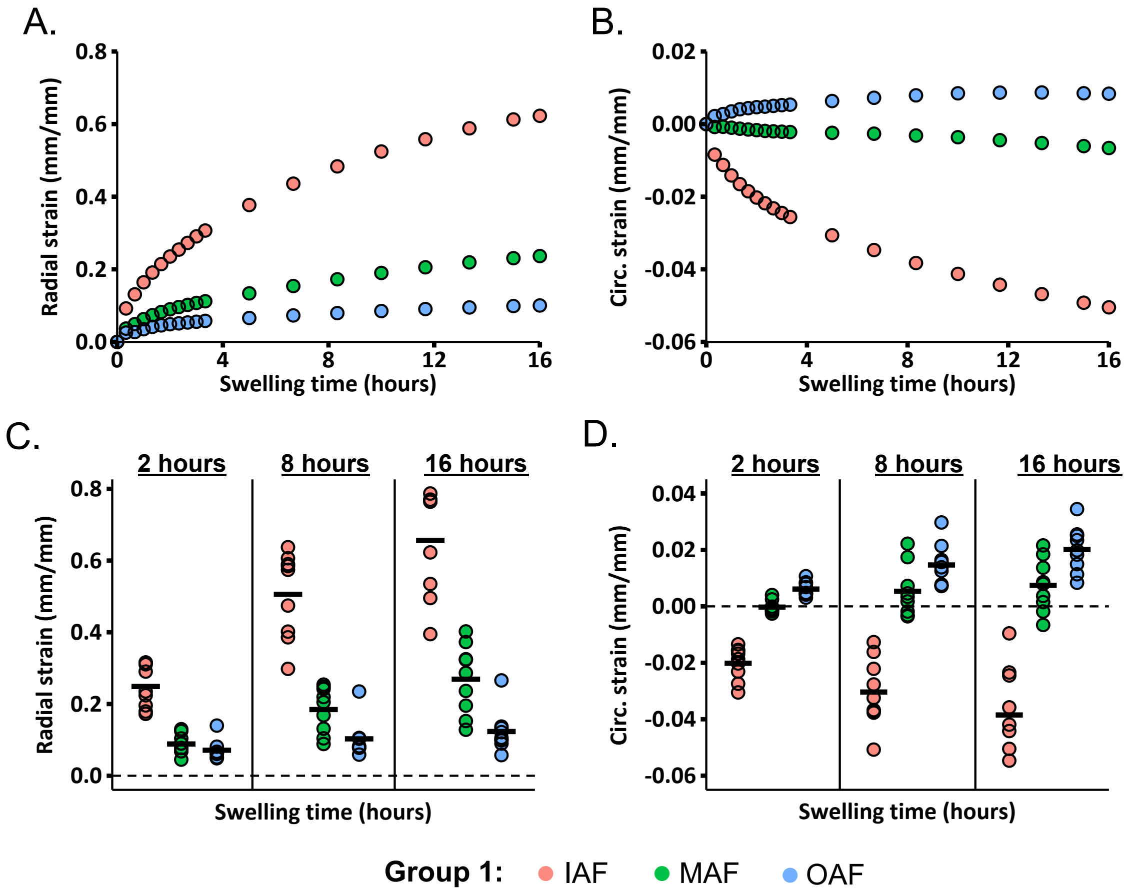

Figure 28: Results for AF rings with fluid flow from the periphery and center. (A) Radial and (B) circumferential strains during the 16-hour swelling period shown for a representative test specimen. (C) Radial and (D) circumferential direction strains after 2, 8, and 16 hours of swelling (n = 8 per group). Red, green, and blue dots represent data for the inner (IAF), middle (MAF), and outer (OAF) annulus fibrosus, respectively. Black lines indicate mean values and dashed lines represent zero strain.

For intact discs (Group 3), strain analysis was initially performed on three separate AF regions to identify spatial differences within the AF; however, no significant differences were observed for circumferential or radial strains (two-way ANOVA, $p > 0.1$). Therefore, AF data were pooled and reported for each time point (Figure 30). Within 2 hours of swelling, the NP experienced negligible radial and circumferential strains (< 0.01 mm/mm or 1%), but the magnitude of radial and circumferential strains continued to increase throughout 16-hour swelling period (Figure 30 – red dots). After 16 hours, average NP radial strain was 0.08 mm/mm and the average circumferential strain was 0.04 mm/mm. In the AF, radial strains were consistent after 8 hours of swelling (~0.06 mm/mm; Figure 30A – blue dots). In contrast, circumferential strains in the AF increased throughout the 16-hour swelling period, with a two-fold increase between 8 and 16 hours (Figure 30B – blue dots). Circumferential strains in the AF of intact discs were 2 to 5 times greater than strains measured in AF rings (Figure 30B *versus* Figure 28D & 29B).

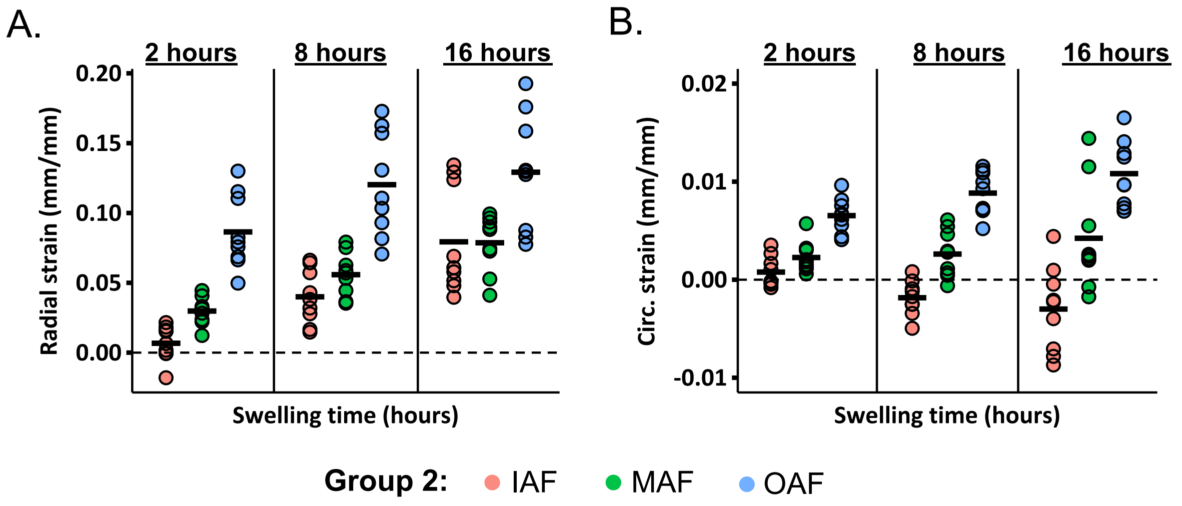

Figure 29: (A) Radial and (B) circumferential strain measurements for AF rings without fluid flow from the center. Data was collected throughout the 16 hour swelling period and analyzed at 2, 8 and 16 hours (n = 9 per group). Red, green and blue colors represent data from the inner (IAF), middle (MAF) and outer (OAF) annulus fibrosus, respectively. Black lines indicate the mean values, and the dashed line represents zero strain.

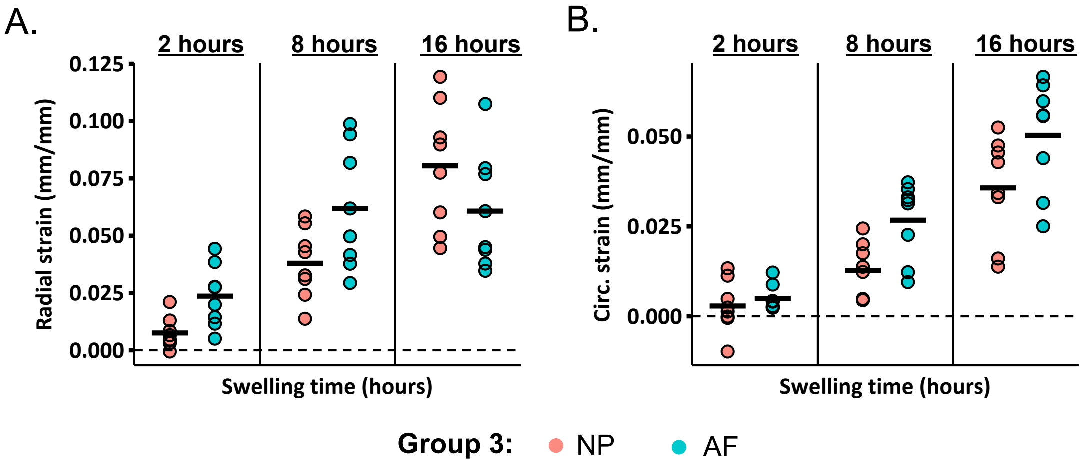

Figure 30: (A) Radial and (B) circumferential strain measurements for intact discs. Data was collected throughout the 16 hour swelling period, and analyzed at 2, 8 and 16 hours (n = 8 per group). Red dots represent data from the nucleus pulposus (NP) and blue dots represents data from the annulus fibrosus (AF). Black lines indicate the mean values and the dashed line represents zero strain.

Similar trends were observed for water content normalized by wet and dry weights for most disc regions (Figure 31A *versus* 31B). Swelling capacity of the inner AF was highly sensitive to the fluid boundary condition (Figure 31 – IAF). As expected, inner AF swelling capacity was greatest with direct access to fluid and was influenced by interactions with the NP and outer AF (Figure 31 – blue bar *versus* yellow or red bars). Interestingly, post-swelling water contents of the inner and outer AF from Group 2 were not significantly different than pre-swelling water content (Figure 31 – green *versus* red bars). For intact discs, both inner and outer

NP absorbed water and increased tissue mass during swelling (Figure 31A&B – green *versus* yellow bars).

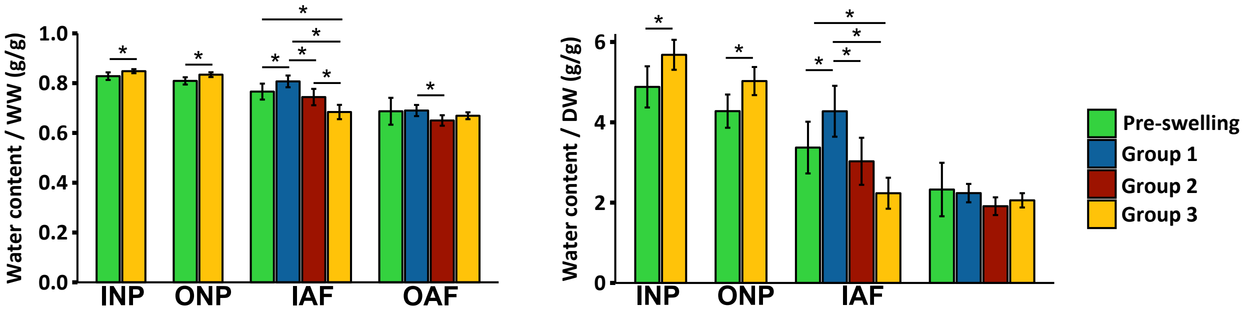

Figure 31: Mean and standard deviation of pre- and post-swelling water content normalized by wet (left) and dry (right) weights. Pre-swelling measurements (green bars) represent data from our previous work (Bezci et al., 2019). Blue bars indicate the water content measurements for the AF rings with fluid flow from the center, and red bars represent water content measurements for the AF rings without fluid flow from the center. Yellow bars represent water content measurements for intact discs. * Represents $p < 0.05$. Error bars represent one standard deviation.

6.4. Discussion

This study aimed to characterize the time-dependent swelling behavior of the intervertebral disc, rather than solely providing equilibrium properties after an extended swelling period. To achieve this, the first study monitored time-dependent changes in tissue mass to compare differences in the swelling capacities of NP and AF explants under free swelling conditions. As expected, this study observed large differences in free swelling behaviors of the NP and AF tissue explants. However, observations from the first study and previous work that measured AF residual strains after swelling were limited to bulk tissue properties, disregarding complex *in situ* fluid flow between the NP and AF (Michalek et al., 2012). To improve our understanding of localized changes during swelling, the second study quantified swelling-induced strains throughout the AF and intact discs. Positive radial strains were observed for all three experimental groups, suggesting radial thickening of intact discs or AF layers as a result of tissue swelling. Circumferential strains were more complex, with small or negative strains observed in the inner AF. Negative circumferential strains observed in the inner AF indicated circumferential shortening due to inward movement of the tissue. In contrast, circumferential strains in the middle and outer AF were positive, suggesting circumferential lengthening at the outer AF periphery.

NP explants experienced a higher swelling rate and equilibrium swelling capacity than AF explants. Specifically, there was a 200% increase in the NP tissue mass, agreeing with previous values reported for the NP, and a 70% increase in the AF tissue mass under free swelling conditions (Bezci et al., 2019, 2015). The difference between NP and AF swelling behaviors was also observed through relative changes in the Raman signal intensity (wavelengths > 3000 cm^{-1}) of each tissue before and after swelling. This relative difference was expected based on previous observations that noted a decrease in tissue swelling capacity with decreases in GAG content from disc center to the outer periphery and with disc degeneration (Bezci et al., 2019, 2015; Urban and Maroudas, 1981; Werbner et al., 2019). However, the AF swelling capacity measured here was ~25% lower than previously measured values, most likely due to differences in boundary conditions, and 20% lower than expected values based on relative differences in NP and AF GAG contents (NP GAG = 319 ± 62 mg/g DW, AF GAG = 129 ± 36 mg/g DW) (Bezci et al., 2019, 2015). The discrepancy between expected and measured values for the AF swelling capacity is partially due to the highly organized, dense collagen fiber architecture in the AF, where collagen fibers counteract the swelling pressure generated by the proteoglycans and limit AF tissue swelling (Yang and O'Connell, 2019). Moreover, degradation of AF GAGs has shown to have limited impact on water content (90% GAG loss resulted in 10% decrease in water content), suggesting that AF porosity may be the primary mechanism for AF fluid flow rather than negatively charged GAGs (Werbner et al., 2019). Lastly, the highly organized fiber architecture in the AF provided shape stability during swelling, whereas NP explants swelled into amorphous blobs when removed from its *in situ* boundary conditions, possibly due to the random orientation of collagen fibers in the NP (Inoue, 1981).

Tissue swelling capacity was sensitive to changes in physical boundary conditions. Based on the water content measurements of the NP and the AF in free-swelling experiments, the swelling capacity of the NP decreased by 60% due to the boundary constraint imposed by the surrounding AF (i.e., from 21.6 ± 2.9 g/g DW to 8.5 ± 1.4 g/g DW). Additional boundary constraint due to fixed axial deformations further decreased the NP swelling capacity by 15% (i.e., to 5.35 g/g DW). Similarly, the swelling capacity of the AF decreased by 30% with the presence of the NP (i.e., from 4.35 ± 0.26 g/g DW to 3.1 ± 0.3 g/g DW) under free swelling conditions. The water content of the AF in intact discs (pooled averages of the inner and outer AF) was reduced by an additional 20% when axial deformation due to tissue swelling was restricted. These findings explain lower strain magnitudes reported here compared to computational results (Yang and O'Connell, 2019). During low loading recovery (e.g., bed rest recovery) the disc height increases due to fluid flow into the disc and poroelastic recovery of the solid matrix (Bezci and O'Connell, 2018). Therefore, recovery of the solid matrix increases disc volume, allowing NP and AF tissues to swell further (Schroeder et al., 2006). These two mechanisms, poroelastic recovery and fluid flow recovery, act as a feedback loop until disc reaches the equilibrium hydration level.

Recent computational modeling using triphasic mixture theory to describe non-fibrous solid matrix of the intervertebral disc tissues demonstrated that radial changes in tissue swelling ratio are largely driven by spatial variations in GAG composition (Yang and O'Connell, 2019). Specifically, simulations of intact discs under swelling conditions predicted relatively uniform radial, axial, and circumferential strains (comparable to conditions in Group 3). Findings from this study agree with those observations, as initial analysis found no differences in AF strains; hence, pooled results were presented in Figure 7. Similarly, previous computational work showed a linear decrease in tensile radial strains from the inner AF to the outer AF in annular rings with fluid exchange permitted at both the inner and outer AF boundaries (comparable to conditions in Group 1). Moreover, circumferential strains were shown to be compressive in the inner AF and tensile in the outer AF, which was confirmed by the findings for Group 1 in this study (Figure 5). Findings from this study provide strong supportive data for computational model validation, which is often a significant challenge in computational modeling (Zhou et al., 2019). Importantly, previous work suggests that radial distribution of GAGs in the AF acts to create radius-dependent residual strains, which is important for maintaining a homeostatic strain distribution with intradiscal pressure from the NP (Bezci et al., 2019; Yang and O'Connell, 2019). Future work will focus on how changes in fluid distribution coupled with age and degenerative changes impact intradiscal deformations.

Besides physical boundary constraints, restricting fluid flow only to the outer periphery further reduced the swelling capacity of the annular rings, especially in the inner AF. Specifically, largest radial strain was observed for the outer AF for AF rings with fluid flow permitted only on the outer periphery; however, there was no statistically significant increase in AF water content throughout the thickness. In contrast, the inner AF water content increased by 21% when fluid flow was allowed to occur simultaneously on the inner and outer tissue surfaces, resulting in peak radial and circumferential strains in the inner AF, not in the outer AF. More importantly, circumferential strain was negative in the inner AF and positive in the outer AF, agreeing with previous findings (Duclos and Michalek, 2017; Michalek et al., 2012). For AF rings, negative circumferential strains coupled with positive radial strains in the inner AF suggest that the inner AF moved inwards during swelling. Higher GAG content in the inner AF allowed it to swell by a larger amount and with faster rate than the outer AF (Bezci et al., 2019). However, large differences in the strain distributions between the two AF-ring groups might imply that boundary effects have a much stronger influence on AF tissue swelling than inhomogeneous GAG distribution.

NP pressurization during swelling restricted AF swelling capacity and resulted in uniform strain distribution throughout the AF. After 2 hours of swelling, the NP experienced negligible radial and circumferential strains (< 0.01 mm/mm or 1%), suggesting that fluid flow takes longer than 2 hours to reach the disc center. After 16 hours of swelling, the radial strains in the outer AF was ~0.1 mm/mm (or 10%), which was 50% lower than the radial strains in the outer AF of annular (Group 3 versus Group 1 or 2). In contrast, the AF in intact discs experienced greater circumferential strains than the AF in annular ring specimens. Taken together, the decrease in radial strains and increase in circumferential strains in the AF of intact discs are likely due to the increase intradiscal pressure as the NP absorbs water and increases its volume. Importantly, AF strain distribution reported here was similar to previous observations on blood vessels, which have a uniform residual strain distribution throughout wall thickness when pressurized (Chuong and Eason, 1986). Residual strains in cardiovascular tissues are thought to be important for maintaining homeostasis during growth and remodeling (Cardamone et al., 2009; Fung, 1991; Rachev and Greenwald, 2003). Similarly, loss of NP pressurization due to degradation of proteoglycans in the NP and inner AF leads to morphological changes in disc properties commonly reported for degenerated discs, including a reduced disc height and inward bulging of the inner AF (Yang and O'Connell, 2019).

Because of the lack of vasculature in the disc, fluid flow *in vivo* primarily occurs either through the AF or through the cartilaginous endplates (Urban et al., 1977). The boundary constraints used in this study did not simulate physiological conditions, as fluid flow for the intact discs in this study was only allowed to occur through the AF periphery and axial deformations were fixed to prevent out-of-plane motion during swelling. However, the main purpose of this study was not to replicate *in vivo* fluid flow, but to provide mechanistic insights into the role of physical and fluid-based boundary constraints on time-dependent swelling behavior. Lastly, data collected from this study was partially used to validate finite element model predictions recently reported by our laboratory. Although trends observed between the computational model and experimental findings were comparable, it should be noted that there were differences in strain magnitudes. These differences may be due in part to comparing finite element predictions for human discs with experimental measurements on bovine discs, as human lumbar and bovine caudal discs differ in geometric shape and composition (O'Connell et al., 2007b), which are properties that impact swelling properties and, therefore, residual strains. Furthermore, differences in axial-direction boundary conditions likely affected strain magnitudes (Yang and O'Connell, 2019). That is, model simulations were allowed to deform freely in the axial direction, but experimental data were collected with fixed physical boundary condition in the axial direction to prevent out-of-plane tissue swelling.

Despite these limitations, we observed nonlinear increases in tissue mass and strains with swelling. These observations are similar to the nonlinear disc height recovery behavior of disc joints under low loading conditions (Bezci and O'Connell, 2018; MacLean et al., 2007; Schmidt et al., 2016b; van der Veen et al., 2005). In conclusion, tissue swelling is a slow time-dependent process that is strongly modulated by tissue-specific biochemical properties and physical boundary constraints. Specifically, the swelling capacity of the NP is largely reduced when swelling is restricted to occur only in the radial direction or constrained by the surrounding AF. The swelling ratio of intact discs was observed to be similar to the swelling ratio of the NP explants, suggesting that radial constraint from the AF might have a greater impact on the NP swelling capacity than restricting fluid flow to occur only through the AF. Furthermore, the presence of the NP in the intact discs (Group 3) reduced peak radial strains in the AF and resulted in uniform strain distribution throughout the AF.

7. Conclusions and future work

The overall goal of this dissertation was to enhance the current understanding of disc height recovery and fluid flow behavior during low loading conditions that simulate bed rest. The findings of this study highlight the complexity of load-dependent fluid flow kinematics during recovery and provide substantial insight into the factors that influence fluid flow into the disc.

Chapter 3 used traditional and novel measurement techniques to characterize radial variations in biochemical composition of bovine caudal discs. The swelling ratio, collagen content, and DNA content were constant throughout the NP, but the water content and water-to-protein ratio of the inner NP were greater than the values measured for the outer NP. This finding suggests that NP is more heterogeneous than previously thought. Findings from this study provided a much better understanding of the intervertebral disc as a composite material, and were useful for explaining the observations in the latter studies.

Chapter 4 explored the effect of external osmotic pressure on disc recovery mechanics by examining the relative changes in disc height recovery with alterations in the osmolarity of the surrounding environment. Disc degeneration is noted by complex changes in disc composition including decreased tissue hydration, GAG content, and irregular collagen architecture. Osmotic loading was used to alter disc hydration without changing disc composition and applied external loading, allowing us to separate changes in disc mechanics due to hydration from changes in biochemical composition and structure. This study explored the relative contribution of two concurrent mechanisms to time-dependent recovery mechanics. Short-term recovery, which is associated with changes on the order of minutes, was found to be insensitive to external osmotic pressure and, hence, was primarily attributed to intrinsic viscoelasticity. In contrast, the rate and magnitude of long-term recovery were sensitive to changes in external osmotic pressure. That is, hyperosmotic pressure hindered fluid flow into the disc, and in turn, limited disc height recovery. The findings from this study helped us to explain our previous findings that noted increased apparent compressive stiffness with hyperosmotic loading (Bezci et al., 2015).

Chapter 5 evaluated the time-dependent recovery behavior of the intervertebral disc under a wide range of compressive loads to characterize the impact of loading history on short-term and long-term recovery mechanics. The motivation behind this study was previous findings that reported differences in recovery mechanics with loading characteristics (i.e., duration, rate, and magnitude). However, these studies did not report any functional relationships between recovery mechanics and compressive stress applied during loading. In contrast, this study developed functional relationships to make predictions for disc recovery behavior following loading at a wide range of compressive loads. This study observed an increase in the recovery rate and magnitude during recovery following higher compressive stresses. However, recovery time did not depend on compressive stress, suggesting that increased recovery rate following larger compressive forces may allow for greater disc height recovery to occur within the same time frame as recovery following low compressive stresses. This finding has potential clinical importance, as it suggests that 8 hours of bed rest might be sufficient for discs to achieve identical hydration levels, regardless of loading history.

Chapter 6 investigated the time-dependent swelling behavior of the intervertebral disc, rather than solely reporting equilibrium swelling properties after an extended swelling period. This study first examined the relative differences in the swelling capacities of the NP and the AF explants under free swelling conditions. Our results indicated that the NP had higher swelling ratio and equilibrium swelling capacity than the AF due to higher GAG content. To better understand region-specific changes during swelling, the second experiment characterized the distribution of swelling-induced strains throughout the AF rings and intact discs. AF rings had a highly heterogeneous strain distribution, which included negative circumferential strains in the inner AF and positive circumferential strains in the outer AF. The NP limited the AF swelling capacity by pushing the AF outwards radially as it swelled. NP pressurization during swelling also reduced peak radial strains in the AF and resulted in uniform strain distribution throughout the AF. This finding has clinical significance as NP pressurization might increase fiber engagement during loading, which might reduce the risk of herniation.

There are some potential areas of future research that can expand on the findings reported in this dissertation. Both joint-level and tissue-level experiments reported in this dissertation had limitations. Observations from joint-level studies were limited to the changes for the entire disc joints, without providing a quantitative analysis of fluid redistribution within the disc during recovery. Although tissue-level swelling experiments provided mechanistic insights into the spatial distributions of swelling-induced strains, they poorly simulated complex, physiological in vivo fluid flow. Research is currently moving towards the use of more advanced imaging tools to image the complex tissue structures in the spine and to provide quantitative, non-invasive measures of biochemical composition. Future work can use magnetic resonance imaging to develop a high-resolution three-dimensional mapping of fluid flow during recovery. Furthermore, changes in water content were only evaluated in axial compression to simplify the analysis; however, *in vivo* deformations are very complex because of multidirectional loads acting on the spine. Future work should incorporate combined loading modalities to mimic physiological loading conditions closely. These studies should span over a wide range of loads since our findings noted significant differences in fluid flow kinematics with loading history.

In conclusion, this dissertation provided substantial insight into the mechanisms of fluid flow in the intervertebral disc. Joint-level studies (Chapters 4-5) examined the role of osmotic loading and load magnitude on time-dependent recovery mechanics. Tissue-level experiments (Chapter 6) examined the effect of physical and fluid-based boundary conditions on the time-dependent swelling behavior of the intact discs and AF rings. Together, these chapters explored factors that influence the slow, time-dependent fluid flow behavior in the intervertebral disc and highlighted the need for investigating complex fluid-solid interactions in the tissue.

8. References

Adams, M.A., Dolan, P., Hutton, W.C., 1987. Diurnal variations in the stresses on the lumbar spine. Spine (Phila. Pa. 1976). https://doi.org/10.1097/00007632-198703000-00008

Adams, M.A., McNally, D.S., Dolan, P., 1996. "Stress" distributions inside intervertebral discs. The effects of age and degeneration. J. Bone Jt. Surg. - Ser. B. https://doi.org/10.1302/0301-620X78B6.1287

Adams, M.A., Roughley, P.J., 2006. What is intervertebral disc degeneration, and what causes it? Spine (Phila. Pa. 1976). https://doi.org/10.1097/01.brs.0000231761.73859.2c

Adams, P., Muir, H., 1976. Qualitative changes with age of proteoglycans of human lumbar discs. Ann. Rheum. Dis. https://doi.org/10.1136/ard.35.4.289

Agee, K.A., Prakki, A., Abu-Haimed, T., Naguib, G.H., Nawareg, M.A., Tezvergil-Mutluay, A., Scheffel, D.L.S., Chen, C., Jang, S.S., Hwang, H., Brackett, M., Grégoire, G., Tay, F.R., Breschi, L., Pashley, D.H., 2015. Water distribution in dentin matrices: Bound vs. unbound water. Dent. Mater. https://doi.org/10.1016/j.dental.2014.12.007

Aktaş, N., Tülek, Y., Gökalp, H.Y., 1997. Determination of differences in free and bound water contents of beef muscle by DSC under various freezing conditions. J. Therm. Anal. https://doi.org/10.1007/bf01979033

Albro, M.B., Bergholt, M.S., St-Pierre, J.P., Vinals Guitart, A., Zlotnick, H.M., Evita, E.G., Stevens, M.M., 2018. Raman spectroscopic imaging for quantification of depth-dependent and local heterogeneities in native and engineered cartilage. npj Regen. Med. https://doi.org/10.1038/s41536-018-0042-7

Alini, M., Eisenstein, S.M., Ito, K., Little, C., Kettler, A.A., Masuda, K., Melrose, J., Ralphs, J., Stokes, I., Wilke, H.J., 2008. Are animal models useful for studying human disc disorders/degeneration? Eur. Spine J. https://doi.org/10.1007/s00586-007-0414-y

Amin, D.B., Lawless, I.M., Sommerfeld, D., Stanley, R.M., Ding, B., Costi, J.J., 2016. The effect of six degree of freedom loading sequence on the in-vitro compressive properties of human lumbar spine segments. J. Biomech. https://doi.org/10.1016/j.jbiomech.2016.09.009

Andriotis, O.G., Desissaire, S., Thurner, P.J., 2018. Collagen Fibrils: Nature's Highly Tunable Nonlinear Springs. ACS Nano. https://doi.org/10.1021/acsnano.8b00837

Antoniou, J., Steffen, T., Nelson, F., Winterbottom, N., Hollander, A.P., Poole, R.A., Aebi, M., Alini, M., 1996. The human lumbar intervertebral disc: Evidence for changes in the biosynthesis and denaturation of the extracellular matrix with growth, maturation, ageing, and degeneration. J. Clin. Invest. https://doi.org/10.1172/JCI118884

Argoubi, M., Shirazi-Adl, A., 1996. Poroelastic creep response analysis of a lumbar motion segment in compression. J. Biomech. https://doi.org/10.1016/0021-9290(96)00035-8

Ayad, S., Abedin, M.Z., Weiss, J.B., Grundy, S.M., 1982. Characterisation of another short-chain disulphide-bonded collagen from cartilage, vitreous and intervertebral disc. FEBS Lett. https://doi.org/10.1016/0014-5793(82)80875-2

Ayotte, D.C., Ito, K., Tepic, S., 2001. Direction-dependent resistance to flow in the endplate of the intervertebral disc: An ex vivo study. J. Orthop. Res. https://doi.org/10.1016/S0736-0266(01)00038-9

Bass, E.C., Duncan, N.A., Hariharan, J.S., Dusick, J., Ulrich Bueff, H., Lotz, J.C., 1997. Frozen storage affects the compressive creep behaviour of the porcine intervertebral disc. Spine (Phila. Pa. 1976). https://doi.org/10.1097/00007632-199712150-00009

Beard, H.K., Roberts, S., O'Brien, J.P., 1981. Immunofluorescent staining for collagen and proteoglycan in normal and scoliotic intervertebral discs. J. Bone Jt. Surg. - Ser. B. https://doi.org/10.1302/0301-620x.63b4.6170646

Beckstein, J.C., Sen, S., Schaer, T.P., Vresilovic, E.J., Elliott, D.M., 2008. Comparison of animal discs used in disc research to human lumbar disc: Axial compression mechanics and glycosaminoglycan content. Spine (Phila. Pa. 1976). https://doi.org/10.1097/BRS.0b013e318166e001

Bezci, S.E., Eleswarapu, A., Klineberg, E.O., O'Connell, G.D., 2018a. Contribution of facet joints, axial compression, and composition to human lumbar disc torsion mechanics. J. Orthop. Res. https://doi.org/10.1002/jor.23870

Bezci, S.E., Klineberg, E.O., O'Connell, G.D., 2018b. Effects of axial compression and rotation angle on torsional mechanical properties of bovine caudal discs. J. Mech. Behav. Biomed. Mater. https://doi.org/10.1016/j.jmbbm.2017.09.022

Bezci, S.E., Nandy, A., O'Connell, G.D., 2015. Effect of hydration on healthy intervertebral disk mechanical stiffness. J. Biomech. Eng. https://doi.org/10.1115/1.4031416

Bezci, S.E., O'Connell, G.D., 2018. Osmotic Pressure Alters Time-dependent Recovery Behavior of the Intervertebral Disc. Spine (Phila. Pa. 1976). https://doi.org/10.1097/BRS.0000000000002354

Bezci, S.E., Werbner, B., Zhou, M., Malollari, K.G., Dorlhiac, G., Carraro, C., Streets, A., O'Connell, G.D., 2019. Radial variation in biochemical composition of the bovine caudal intervertebral disc. JOR SPINE. https://doi.org/10.1002/jsp2.1065

Bonifacio, A., Sergo, V., 2010. Effects of sample orientation in Raman microspectroscopy of collagen fibers and their impact on the interpretation of the amide III band. Vib. Spectrosc. https://doi.org/10.1016/j.vibspec.2010.04.004

Bonner, W.M., Jonsson, H., Malanos, C., Bryant, M., 1975. Changes in the lipids of human articular cartilage with age. Arthritis Rheum. https://doi.org/10.1002/art.1780180505

Boos, N., Nerlich, A.G., Wiest, I., Von Der Mark, K., Aebi, M., 1997. Immunolocalization of type X collagen in human lumbar intervertebral discs during ageing and degeneration. Histochem. Cell Biol. https://doi.org/10.1007/s004180050187

Boos, N., Weissbach, S., Rohrbach, H., Weiler, C., Spratt, K.F., Nerlich, A.G., 2002. Classification of age-related changes in lumbar intervertebral discs: 2002 Volvo award in basic science. Spine (Phila. Pa. 1976). https://doi.org/10.1097/00007632-200212010-00002

Botsford, D.J., Esses, S.I., Ogilvie-Harris, D.J., 1994. In vivo diurnal variation in intervertebral disc volume and morphology. Spine (Phila. Pa. 1976). https://doi.org/10.1097/00007632-199404150-00012

Bozec, L., Odlyha, M., 2011. Thermal denaturation studies of collagen by microthermal analysis and atomic force microscopy. Biophys. J. https://doi.org/10.1016/j.bpj.2011.04.033

Brinjikji, W., Luetmer, P.H., Comstock, B., Bresnahan, B.W., Chen, L.E., Deyo, R.A., Halabi, S., Turner, J.A., Avins, A.L., James, K., Wald, J.T., Kallmes, D.F., Jarvik, J.G., 2015. Systematic literature review of imaging features of spinal degeneration in asymptomatic populations. Am. J. Neuroradiol. https://doi.org/10.3174/ajnr.A4173

Broberg, K.B., 1993. Slow deformation of intervertebral discs. J. Biomech. https://doi.org/10.1016/0021-9290(93)90012-4

Brooks, J., 1934. Bound water in muscle. J. Gen. Physiol. https://doi.org/10.1085/jgp.17.6.783

Budday, S., Sommer, G., Holzapfel, G.A., Steinmann, P., Kuhl, E., 2017. Viscoelastic parameter identification of human brain tissue. J. Mech. Behav. Biomed. Mater. https://doi.org/10.1016/j.jmbbm.2017.07.014

Burns, M.L., Kaleps, I., Kazarian, L.E., 1984. Analysis of compressive creep behavior of the vertebral unit subjected to a uniform axial loading using exact parametric solution equations of Kelvin-solid models-Part I. Human intervertebral joints. J. Biomech. https://doi.org/10.1016/0021-9290(84)90129-5

Callaghan, J.P., Gunning, J.L., McGill, S.M., 1998. The relationship between lumbar spine load and muscle activity during extensor exercises. Phys. Ther. https://doi.org/10.1093/ptj/78.1.8

Campagnola, P.J., Millard, A.C., Terasaki, M., Hoppe, P.E., Malone, C.J., Mohler, W.A., 2002. Three-dimensional high-resolution second-harmonic generation imaging of endogenous structural proteins in biological tissues. Biophys. J. https://doi.org/10.1016/S0006-3495(02)75414-3

Campana, S., Charpail, E., de Guise, J.A., Rillardon, L., Skalli, W., Mitton, D., 2011. Relationships between viscoelastic properties of lumbar intervertebral disc and degeneration grade assessed by MRI. J. Mech. Behav. Biomed. Mater. https://doi.org/10.1016/j.jmbbm.2011.01.007

Cannella, M., Arthur, A., Allen, S., Keane, M., Joshi, A., Vresilovic, E., Marcolongo, M., 2008. The role of the nucleus pulposus in neutral zone human lumbar intervertebral disc mechanics. J. Biomech. https://doi.org/10.1016/j.jbiomech.2008.04.037

Cardamone, L., Valentín, A., Eberth, J.F., Humphrey, J.D., 2009. Origin of axial prestretch and residual stress in arteries. Biomech. Model. Mechanobiol. https://doi.org/10.1007/s10237-008-0146-x

Cassidy, J.J., Hiltner, A., Baer, E., 1989. Hierarchical structure of the intervertebral disc. Connect. Tissue Res. https://doi.org/10.3109/03008208909103905

Cassidy, J.J., Silverstein, M.S., Hiltner, A., Baer, E., 1990. A water transport model for the creep response of the intervertebral disc. J. Mater. Sci. Mater. Med. https://doi.org/10.1007/BF00839072

Castro, A.P.G., Paul, C.P.L., Detiger, S.E.L., Smit, T.H., van Royen, B.J., Pimenta Claro, J.C., Mullender, M.G., Alves, J.L., 2014. Long-term creep behavior of the intervertebral disk: Comparison between bioreactor data and numerical results. Front. Bioeng. Biotechnol. https://doi.org/10.3389/fbioe.2014.00056

Chae, Y., Protsenko, D., Lavernia, E.J., Wong, B.J.F., 2009. Effect of water content on enthalpic relaxations in porcine septal cartilage, in: Journal of Thermal Analysis and Calorimetry. https://doi.org/10.1007/s10973-007-8782-4

Chagnon, A., Aubin, C.É., Villemure, I., 2010. Biomechanical influence of disk properties on the load transfer of healthy and degenerated disks using a poroelastic finite element model. J. Biomech. Eng. https://doi.org/10.1115/1.4002550

Chan, D.D., Khan, S.N., Ye, X., Curtiss, S.B., Gupta, M.C., Klineberg, E.O., Neu, C.P., 2011. Mechanical deformation and glycosaminoglycan content changes in a rabbit annular puncture disc degeneration model. Spine (Phila. Pa. 1976). https://doi.org/10.1097/BRS.0b013e3181f8be52

Charnley, J., 1952. THE IMBIBITION OF FLUID AS A CAUSE OF HERNIATION OF THE NUCLEUS PULPOSUS. Lancet. https://doi.org/10.1016/S0140-6736(52)92428-8

Cheng, J.X., Xie, X.S., 2004. Coherent anti-Stokes Raman scattering microscopy: Instrumentation, theory, and applications. J. Phys. Chem. B. https://doi.org/10.1021/jp035693v

Chow, D.H.K., Luk, K.D.K., Evans, J.H., Leong, J.C.Y., 1996. Effects of short anterior lumbar interbody fusion on biomechanics of neighboring unfused segments. Spine (Phila. Pa.

1976). https://doi.org/10.1097/00007632-199603010-00004

Choy, A.T.H., Chan, B.P., 2015. A structurally and functionally biomimetic biphasic scaffold for intervertebral disc tissue engineering. PLoS One. https://doi.org/10.1371/journal.pone.0131827

Chuong, C.J., Eason, G., 1986. On residual stresses in arteries. J. Biomech. Eng. https://doi.org/10.1115/1.3138600

Cortes, D.H., Jacobs, N.T., DeLucca, J.F., Elliott, D.M., 2014. Elastic, permeability and swelling properties of human intervertebral disc tissues: A benchmark for tissue engineering. J. Biomech. https://doi.org/10.1016/j.jbiomech.2013.12.021

Costi, J.J., Hearn, T.C., Fazzalari, N.L., 2002. The effect of hydration on the stiffness of intervertebral discs in an ovine model. Clin. Biomech. https://doi.org/10.1016/S0268-0033(02)00035-9

Costi, J.J., Stokes, I.A., Gardner-Morse, M.G., Iatridis, J.C., 2008. Frequency-dependent behavior of the intervertebral disc in response to each of six degree of freedom dynamic loading: Solid phase and fluid phase contributions. Spine (Phila. Pa. 1976). https://doi.org/10.1097/BRS.0b013e31817bb116

Daemen, S., Van Polanen, N., Hesselink, M.K.C., 2018. The effect of diet and exercise on lipid droplet dynamics in human muscle tissue. J. Exp. Biol. https://doi.org/10.1242/jeb.167015

Demers, C.N., Antoniou, J., Mwale, F., 2004. Value and limitations of using the bovine tail as a model for the human lumbar spine. Spine (Phila. Pa. 1976). https://doi.org/10.1097/01.brs.0000147744.74215.b0

Detiger, S.E.L., Holewijn, R.M., Hoogendoorn, R.J.W., van Royen, B.J., Helder, M.N., Berger, F.H., Kuijer, J.P.A., Smit, T.H., 2015. MRI T2* mapping correlates with biochemistry and histology in intervertebral disc degeneration in a large animal model. Eur. Spine J. https://doi.org/10.1007/s00586-014-3498-1

Dhillon, N., Bass, E.C., Lotz, J.C., 2001. Effect of frozen storage on the creep behavior of human intervertebral discs, in: Spine. https://doi.org/10.1097/00007632-200104150-00011

DiSilvestro, M.R., Zhu, Q., Wong, M., Jurvelin, J.S., Suh, J.K.F., 2001. Biphasic poroviscoelastic simulation of the unconfined compression of articular cartilage: I - Simultaneous prediction of reaction force and lateral displacement. J. Biomech. Eng. https://doi.org/10.1115/1.1351890

Dreischarf, M., Shirazi-Adl, A., Arjmand, N., Rohlmann, A., Schmidt, H., 2016. Estimation of loads on human lumbar spine: A review of in vivo and computational model studies. J. Biomech. https://doi.org/10.1016/j.jbiomech.2015.12.038

Drost, M.R., Willems, P., Snijders, H., Huyghe, J.M., Janssen, J.D., Huson, A., 1995. Confined compression of canine annulus fibrosus under chemical and mechanical loading. J. Biomech. Eng. https://doi.org/10.1115/1.2794197

Duclos, S.E., Michalek, A.J., 2017. Residual strains in the intervertebral disc annulus fibrosus suggest complex tissue remodeling in response to in-vivo loading. J. Mech. Behav. Biomed. Mater. https://doi.org/10.1016/j.jmbbm.2017.02.010

Elliott, D.M., Yerramalli, C.S., Beckstein, J.C., Boxberger, J.I., Johannessen, W., Vresilovic, E.J., 2008. The effect of relative needle diameter in puncture and sham injection animal models of degeneration. Spine (Phila. Pa. 1976). https://doi.org/10.1097/BRS.0b013e318166e0a2

Emanuel, K.S., Mader, K.T., Peeters, M., Kingma, I., Rustenburg, C.M.E., Vergroesen, P.P.A., Sammon, C., Smit, T.H., 2018. Early changes in the extracellular matrix of the degenerating intervertebral disc, assessed by Fourier transform infrared imaging. Osteoarthr. Cartil. https://doi.org/10.1016/j.joca.2018.06.003

Evans, C.L., Potma, E.O., Puoris'haag, M., Côté, D., Lin, C.P., Xie, X.S., 2005. Chemical imaging of tissue in vivo with video-rate coherent anti-Strokes Raman scattering microscopy. Proc. Natl. Acad. Sci. U. S. A. https://doi.org/10.1073/pnas.0508282102

Eyre, D.R., Muir, H., 1977. Quantitative analysis of types I and II collagens in human intervertebral discs at various ages. BBA - Protein Struct. https://doi.org/10.1016/0005-2795(77)90211-2

Eyre, D.R., Muir, H., 1976. Types I and II collagens in intervertebral disc. Interchanging radial distributions in annulus fibrosus. Biochem. J. https://doi.org/10.1042/bj1570267

Farfan, H.F., Cossette, J.W., Robertson, G.H., Wells, R. V., Kraus, H., 1970. The effects of torsion on the lumbar intervertebral joints: the role of torsion in the production of disc degeneration. J. Bone Joint Surg. Am. https://doi.org/10.2106/00004623-197052030-00006

Farndale, R.W., Buttle, D.J., Barrett, A.J., 1986. Improved quantitation and discrimination of sulphated glycosaminoglycans by use of dimethylmethylene blue. BBA - Gen. Subj. https://doi.org/10.1016/0304-4165(86)90306-5

Farndale, R.W., Sayers, C.A., Barrett, A.J., 1982. A direct spectrophotometric microassay for sulfated glycosaminoglycans in cartilage cultures. Connect. Tissue Res. https://doi.org/10.3109/03008208209160269

Ferguson, S.J., Ito, K., Nolte, L.P., 2004. Fluid flow and convective transport of solutes within the intervertebral disc. J. Biomech. https://doi.org/10.1016/S0021-9290(03)00250-1

Finlayson, R., Woods, S.J., 1975. Lipid in the Achilles' tendon. A comparative study. Atherosclerosis. https://doi.org/10.1016/0021-9150(75)90050-7

Flach, C.R., Moore, D.J., 2013. Infrared and Raman imaging spectroscopy of ex vivo skin. Int. J. Cosmet. Sci. https://doi.org/10.1111/ics.12020

Franklin, L., Hull, E.W., 1966. Lipid content of the intervertebral disc. Clin. Chem.

Fratzl, P., Weinkamer, R., 2007. Nature's hierarchical materials. Prog. Mater. Sci. https://doi.org/10.1016/j.pmatsci.2007.06.001

Frost, B.A., Camarero-Espinosa, S., Johan Foster, E., 2019. Materials for the spine: Anatomy, problems, and solutions. Materials (Basel). https://doi.org/10.3390/ma12020253

Fujiwara, A., Tamai, K., Yamato, M., An, H.S., Yoshida, H., Saotome, K., Kurihashi, A., 1999. The relationship between facet joint osteoarthritis and disc degeneration of the lumbar spine: An MRI study. Eur. Spine J. https://doi.org/10.1007/s005860050193

Fung, Y.C., 1991. What are the residual stresses doing in our blood vessels? Ann. Biomed. Eng. https://doi.org/10.1007/BF02584301

Galante, J.O., 1967. Tensile Properties of the Human Lumbar Annulus Fibrosus. Acta Orthop. Scand. https://doi.org/10.3109/ort.1967.38.suppl-100.01

Galbusera, F., Van Rijsbergen, M., Ito, K., Huyghe, J.M., Brayda-Bruno, M., Wilke, H.J., 2014. Ageing and degenerative changes of the intervertebral disc and their impact on spinal flexibility. Eur. Spine J. https://doi.org/10.1007/s00586-014-3203-4

Gardner-Morse, M.G., Stokes, I.A., 2003. Physiological axial compressive preloads increase motion segment stiffness, linearity and hysteresis in all six degrees of freedom for small displacements about the neutral posture. J. Orthop. Res. https://doi.org/10.1016/S0736-0266(02)00199-7

Gellhorn, A.C., Katz, J.N., Suri, P., 2013. Osteoarthritis of the spine: The facet joints. Nat. Rev. Rheumatol. https://doi.org/10.1038/nrrheum.2012.199

Ghosh, P., Bushell, G.R., Taylor, T.F.K., Akeson, W.H., 1977. Collagens, elastin and noncollagenous protein of the intervertebral disk. Clin. Orthop. Relat. Res. https://doi.org/10.1097/00003086-197711000-00014

Gniadecka, M., Nielsen, O.F., Christensen, D.H., Wulf, H.C., 1998a. Structure of water, proteins, and lipids in intact human skin, hair, and nail. J. Invest. Dermatol. https://doi.org/10.1046/j.1523-1747.1998.00146.x

Gniadecka, M., Nielsen, O.F., Wessel, S., Heidenheim, M., Christensen, D., Wulf, H.C., 1998b. Water and protein structure in photoaged and chronically aged skin. J. Invest. Dermatol. https://doi.org/10.1046/j.1523-1747.1998.00430.x

Gray, M.L., Pizzanelli, A.M., Grodzinsky, A.J., Lee, R.C., 1988. Mechanical and physicochemical determinants of the chondrocyte biosynthetic response. J. Orthop. Res. https://doi.org/10.1002/jor.1100060602

Gu, W.Y., Yao, H., Vega, A.L., Flagler, D., 2004. Diffusivity of ions in agarose gels and intervertebral disc: Effect of porosity. Ann. Biomed. Eng. https://doi.org/10.1007/s10439-004-7823-4

Gullbrand, S.E., Peterson, J., Mastropolo, R., Roberts, T.T., Lawrence, J.P., Glennon, J.C., DiRisio, D.J., Ledet, E.H., 2015. Low rate loading-induced convection enhances net transport into the intervertebral disc in vivo. Spine J. https://doi.org/10.1016/j.spinee.2014.12.003

Gunning, J.L., Callaghan, J.P., McGill, S.M., 2001. Spinal posture and prior loading history modulate compressive strength and type of failure in the spine: A biomechanical study using a porcine cervical spine model. Clin. Biomech. https://doi.org/10.1016/S0268-0033(01)00032-8

Ha, K.Y., Schendel, M.J., Lewis, J.L., Ogilvie, J.W., 1993. Effect of immobilization and configuration on lumbar adjacent-segment biomechanics. J. Spinal Disord. Tech. https://doi.org/10.1097/00024720-199304000-00002

Haefeli, M., Kalberer, F., Saegesser, D., Nerlich, A.G., Boos, N., Paesold, G., 2006. The course of macroscopic degeneration in the human lumbar intervertebral disc. Spine (Phila. Pa. 1976). https://doi.org/10.1097/01.brs.0000222032.52336.8e

Han, K.S., Rohlmann, A., Zander, T., Taylor, W.R., 2013. Lumbar spinal loads vary with body height and weight. Med. Eng. Phys. https://doi.org/10.1016/j.medengphy.2012.09.009

Hardingham, T.E., Muir, H., 1972. The specific interaction of hyaluronic acid with cartilage proteoglycans. BBA - Gen. Subj. https://doi.org/10.1016/0304-4165(72)90160-2

Haughton, V.M., Rogers, B., Elizabeth Meyerand, M., Resnick, D.K., 2002. Measuring the axial rotation of lumbar vertebrae in vivo with MR imaging. Am. J. Neuroradiol.

Hayes, W.C., Bodine, A.J., 1978. Flow-independent viscoelastic properties of articular cartilage matrix. J. Biomech. https://doi.org/10.1016/0021-9290(78)90075-1

Hingorani, R. V., Provenzano, P.P., Lakes, R.S., Escarcega, A., Vanderby, R., 2004. Nonlinear viscoelasticity in rabbit medial collateral ligament. Ann. Biomed. Eng. https://doi.org/10.1023/B:ABME.0000012751.31686.70

Hollander, A.P., Heathfield, T.F., Webber, C., Iwata, Y., Bourne, R., Rorabeck, C., Poole, A.R., 1994. Increased damage to type II collagen in osteoarthritic articular cartilage detected by a new immunoassay. J. Clin. Invest. https://doi.org/10.1172/JCI117156

Holzapfel, G.A., Schulze-Bauer, C.A.J., Feigl, G., Regitnig, P., 2005. Single lamellar mechanics of the human lumbar anulus fibrosus. Biomech. Model. Mechanobiol. https://doi.org/10.1007/s10237-004-0053-8

Hong, C.H., Park, J.S., Jung, K.J., Kim, W.J., 2010. Measurement of the Normal Lumbar Intervertebral Disc Space using Magnetic Resonance Imaging. Asian Spine J. https://doi.org/10.4184/asj.2010.4.1.1

Hsieh, A.H., Wagner, D.R., Cheng, L.Y., Lotz, J.C., 2005. Dependence of mechanical behavior of the murine tail disc on regional material properties: A parametric finite element study. J. Biomech. Eng. https://doi.org/10.1115/1.2073467

Huang, Z., Delparastan, P., Burch, P., Cheng, J., Cao, Y., Messersmith, P.B., 2019. Injectable dynamic covalent hydrogels of boronic acid polymers cross-linked by bioactive plant-derived polyphenols, in: Transactions of the Annual Meeting of the Society for Biomaterials and the Annual International Biomaterials Symposium. https://doi.org/10.1039/C8BM00453F

Hult, E., Ekström, L., Kaigle, A., Holm, S., Hansson, T., 1995. In vivo measurement of spinal column viscoelasticity—an animal model. Proc. Inst. Mech. Eng. Part H J. Eng. Med. https://doi.org/10.1243/PIME_PROC_1995_209_326_02

Hwang, D., Gabai, A.S., Yu, M., Yew, A.G., Hsieh, A.H., 2012. Role of load history in intervertebral disc mechanics and intradiscal pressure generation. Biomech. Model. Mechanobiol. https://doi.org/10.1007/s10237-011-0295-1

Iatridis, J.C., MacLean, J.J., O'Brien, M., Stokes, I.A.F., 2007. Measurements of proteoglycan and water content distribution in human lumbar intervertebral discs. Spine (Phila. Pa. 1976). https://doi.org/10.1097/BRS.0b013e318067dd3f

Inoue, H., 1981. Three-dimensional architecture of lumbar intervertebrai discs. Spine (Phila. Pa. 1976). https://doi.org/10.1097/00007632-198103000-00006

Jackson, A., Yao, H., Brown, M.D., Yong Gu, W., 2006. Anisotropic ion diffusivity in intervertebral disc: An electrical conductivity approach. Spine (Phila. Pa. 1976). https://doi.org/10.1097/01.brs.0000245842.02717.1b

Jay Lipson, S., Muir, H., 1981. Experimental intervertebral disc degeneration. morphologic and proteoglycan changes over time. Arthritis Rheum. https://doi.org/10.1002/art.1780240103

Jim, B., Steffen, T., Moir, J., Roughley, P., Haglund, L., 2011. Development of an intact intervertebral disc organ culture system in which degeneration can be induced as a prelude to studying repair potential. Eur. Spine J. https://doi.org/10.1007/s00586-011-1721-x

Johannessen, W., Cloyd, J.M., O'Connell, G.D., Vresilovic, E.J., Elliott, D.M., 2006. Trans-endplate nucleotomy increases deformation and creep response in axial loading. Ann. Biomed. Eng. https://doi.org/10.1007/s10439-005-9070-8

Johannessen, W., Vresilovic, E.J., Wright, A.C., Elliott, D.M., 2004. Intervertebral disc mechanics are restored following cyclic loading and unloaded recovery. Ann. Biomed. Eng. https://doi.org/10.1023/B:ABME.0000007792.19071.8c

Johnston, S.L., Campbell, M.R., Scheuring, R., Feiveson, A.H., 2010. Risk of herniated nucleus pulposus among U.S. astronauts. Aviat. Sp. Environ. Med. https://doi.org/10.3357/ASEM.2427.2010

Johnstone, B., Bayliss, M.T., 1995. The large proteoglycans of the human intervertebral disc: Changes in their biosynthesis and structure with age5 topography5 and pathology. Spine (Phila. Pa. 1976). https://doi.org/10.1097/00007632-199503150-00008

Kannus, P., Jozsa, L., 1991. Histopathological changes preceding spontaneous rupture of a tendon: A controlled study of 891 patients. J. Bone Jt. Surg. - Ser. A. https://doi.org/10.2106/00004623-199173100-00009

Kazarian, L.E., 1975. Creep characteristics of the human spinal column. Orthop. Clin. North Am.

Keller, T.S., Hansson, T.H., Holm, S.H., Pope, M.M., Spengler, D.M., 1988. In vivo creep behavior of the normal and degenerated porcine intervertebral disk: A preliminary report. J. Spinal Disord.

Keller, T.S., Holm, S.H., Hansson, T.H., Spengler, D.M., 1990. The dependence of intervertebral disc mechanical properties on physiologic conditions. Spine (Phila. Pa. 1976). https://doi.org/10.1097/00007632-199008010-00004

Keller, T.S., Spengler, D.M., Hansson, T.H., 1987. Mechanical behavior of the human lumbar spine. I. Creep analysis during static compressive loading. J. Orthop. Res. https://doi.org/10.1002/jor.1100050402

Kelly, T.A.N., Roach, B.L., Weidner, Z.D., Mackenzie-Smith, C.R., O'Connell, G.D., Lima, E.G., Stoker, A.M., Cook, J.L., Ateshian, G.A., Hung, C.T., 2013. Tissue-engineered articular cartilage exhibits tension-compression nonlinearity reminiscent of the native cartilage. J. Biomech. https://doi.org/10.1016/j.jbiomech.2013.05.017

Kemper, A.R., McNally, C., Duma, S.M., 2007. The influence of strain rate on the compressive stiffness properties of human lumbar intervertebral discs, in: Biomedical Sciences Instrumentation.

Kingma, I., Van Dien, J.H., Nicolay, K., Maat, J.J., Weinans, H., 2000. Monitoring water content in deforming intervertebral disc tissue by finite element analysis of MRI data. Magn. Reson. Med. https://doi.org/10.1002/1522-2594(200010)44:4<650::AID-MRM21>3.0.CO;2-0

Koeller, W., Funke, F., Hartmann, F., 1984. Biomechanical behavior of human intervertebral discs subjected to long lasting axial loading. Biorheology. https://doi.org/10.3233/BIR-1984-21502

Korecki, C.L., MacLean, J.J., Iatridis, J.C., 2007. Characterization of an in vitro intervertebral disc organ culture system. Eur. Spine J. https://doi.org/10.1007/s00586-007-0327-9

Kraemer, J., 1985. Dynamic characteristics of the vertebral column, effects of prolonged loading. Ergonomics. https://doi.org/10.1080/00140138508963117

Kudo, K., Ishida, J., Syuu, G., Sekine, Y., Ikeda-Fukazawa, T., 2014. Structural changes of water in poly(vinyl alcohol) hydrogel during dehydration. J. Chem. Phys. https://doi.org/10.1063/1.4862996

Lee, C.K., 1988. Accelerated degeneration of the segment adjacent to a lumbar fusion. Spine (Phila. Pa. 1976). https://doi.org/10.1097/00007632-198803000-00029

Lehmann, T.R., Spratt, K.F., Tozzi, J.E., Weinstein, J.N., Reinarz, S.J., El-Khoury, G.Y., Colby, H., 1987. Long-term follow-up of lower lumbar fusion patients. Spine (Phila. Pa. 1976). https://doi.org/10.1097/00007632-198703000-00004

Lim, N.S.J., Hamed, Z., Yeow, C.H., Chan, C., Huang, Z., 2011. Early detection of biomolecular changes in disrupted porcine cartilage using polarized Raman spectroscopy. J. Biomed. Opt. https://doi.org/10.1117/1.3528006

Lionello, G., Cristofolini, L., 2014. A practical approach to optimizing the preparation of speckle patterns for digital-image correlation. Meas. Sci. Technol. https://doi.org/10.1088/0957-0233/25/10/107001

Liu, X., Krishnamoorthy, D., Lin, L., Xue, P., Zhang, F., Chi, L., Linhardt, R.J., Iatridis, J.C., 2018. A method for characterising human intervertebral disc glycosaminoglycan disaccharides using liquid chromatography-mass spectrometry with multiple reaction monitoring. Eur. Cells Mater. https://doi.org/10.22203/eCM.v035a09

Lu, X.L., Mow, V.C., 2008. Biomechanics of articular cartilage and determination of material properties. Med. Sci. Sports Exerc. https://doi.org/10.1249/mss.0b013e31815cb1fc

Lu, Y.M., Hutton, W.C., 1998. The effect of fluid loss on the viscoelastic behavior of the lumbar intervertebral disc in compression. J. Biomech. Eng. https://doi.org/10.1115/1.2834306

Lu, Y.M., Hutton, W.C., Gharpuray, V.M., 1996. Do bending, twisting, and diurnal fluid changes in the disc affect the propensity to prolapse? A viscoelastic finite element model. Spine (Phila. Pa. 1976). https://doi.org/10.1097/00007632-199611150-00006

Luoma, K., Riihimäki, H., Luukkonen, R., Raininko, R., Viikari-Juntura, E., Lamminen, A., 2000. Low back pain in relation to lumbar disc degeneration. Spine (Phila. Pa. 1976). https://doi.org/10.1097/00007632-200002150-00016

Lyons, G., Eisenstein, S.M., Sweet, M.B.E., 1981. Biochemical changes in intervertebral disc degeneration. BBA - Gen. Subj. https://doi.org/10.1016/0304-4165(81)90476-1

MacLean, J.J., Owen, J.P., Iatridis, J.C., 2007. Role of endplates in contributing to compression behaviors of motion segments and intervertebral discs. J. Biomech. https://doi.org/10.1016/j.jbiomech.2005.11.013

Malko, J.A., Hutton, W.C., Fajman, W.A., 2002. An in vivo mri study of the changes in volume (and fluid content) of the lumbar intervertebral disc after overnight bed rest and during an 8-hour walking protocol. J. Spinal Disord. Tech. https://doi.org/10.1097/00024720-200204000-00012

Malko, J.A., Mutton, W.C., Fajman, W.A., 1999. An in vivo magnetic resonance imaging study of changes in the volume (and fluid content) of the lumbar intervertebral discs during a simulated diurnal load cycle, in: Spine. https://doi.org/10.1097/00007632-199905150-00016

Manoharan, R., Wang, Y., Feld, M.S., 1996. Histochemical analysis of biological tissues using Raman spectroscopy. Spectrochim. Acta - Part A Mol. Spectrosc. https://doi.org/10.1016/0584-8539(95)01573-6

Marchand, F., Ahmed, A.M., 1990. Investigation of the laminate structure of lumbar disc anulus fibrosus. Spine (Phila. Pa. 1976). https://doi.org/10.1097/00007632-199005000-00011

Martin, J.T., Gorth, D.J., Beattie, E.E., Harfe, B.D., Smith, L.J., Elliott, D.M., 2013. Needle puncture injury causes acute and long-term mechanical deficiency in a mouse model of intervertebral disc degeneration. J. Orthop. Res. https://doi.org/10.1002/jor.22355

Martin, J.T., Oldweiler, A.B., Spritzer, C.E., Soher, B.J., Erickson, M.M., Goode, A.P., DeFrate, L.E., 2018. A magnetic resonance imaging framework for quantifying intervertebral disc deformation in vivo: Reliability and application to diurnal variations in lumbar disc shape. J. Biomech. https://doi.org/10.1016/j.jbiomech.2018.01.045

McCann, M.R., Séguin, C.A., 2016. Notochord cells in intervertebral disc development and degeneration. J. Dev. Biol. https://doi.org/10.3390/jdb4010003

McMillan, D.W., Garbutt, G., Adams, M.A., 1996. Effect of sustained loading on the water content of intervertebral discs: Implications for disc metabolism. Ann. Rheum. Dis. https://doi.org/10.1136/ard.55.12.880

McNally, D.S., Adams, M.A., 1992. Internal intervertebral disc mechanics as revealed by stress profilometry. Spine (Phila. Pa. 1976). https://doi.org/10.1097/00007632-199201000-00011

Melrose, J., Ghosh, P., Taylor, T.K.F., 2001. A comparative analysis of the differential spatial and temporal distributions of the large (aggrecan, versican) and small (decorin, biglycan, fibromodulin) proteoglycans of the intervertebral disc. J. Anat. https://doi.org/10.1017/S0021878200007202

Melrose, J., Ghosh, P., Taylor, T.K.F., 1994. Proteoglycan heterogeneity in the normal adult ovine intervertebral disc. Matrix Biol. https://doi.org/10.1016/0945-053X(94)90030-2

Michalek, A.J., Buckley, M.R., Bonassar, L.J., Cohen, I., Iatridis, J.C., 2009. Measurement of local strains in intervertebral disc anulus fibrosus tissue under dynamic shear: Contributions of matrix fiber orientation and elastin content. J. Biomech. https://doi.org/10.1016/j.jbiomech.2009.06.047

Michalek, A.J., Gardner-Morse, M.G., Iatridis, J.C., 2012. Large residual strains are present in the intervertebral disc annulus fibrosus in the unloaded state. J. Biomech. https://doi.org/10.1016/j.jbiomech.2012.01.042

Mikawa, Y., Hamagami, H., Shikata, J., Yamamuro, T., 1986. Elastin in the human intervertebral disk - A histological and biochemical study comparing it with elastin in the human yellow ligament. Arch. Orthop. Trauma. Surg. https://doi.org/10.1007/BF00449940

Miles, C.A., Ghelashvili, M., 1999. Polymer-in-a-box mechanism for the thermal stabilization of collagen molecules in fibers. Biophys. J. https://doi.org/10.1016/S0006-3495(99)77476-X

Murata, M., Morio, Y., Kuranobu, K., 1994. Lumbar disc degeneration and segmental instability: a comparison of magnetic resonance images and plain radiographs of patients with low back pain. Arch. Orthop. Trauma Surg. https://doi.org/10.1007/BF00426175

Nachemson, A., 1963. the influence of spinal movements on the lumbar intradiscal pressure and on the tensile stresses in the annulus fibrosus. Acta Orthop. https://doi.org/10.3109/17453676308999846

Nachemson, A.L., 1981. Disc pressure measurements. Spine (Phila. Pa. 1976). https://doi.org/10.1097/00007632-198101000-00020

Nagata, H., Schendel, M.J., Transfeldt, E.E., Lewis, J.L., 1993. The effects of immobilization of long segments of the spine on the adjacent and distal facet force and lumbosacral motion. Spine (Phila. Pa. 1976). https://doi.org/10.1097/00007632-199312000-00017

Nerlich, A.G., Schaaf, R., Wälchli, B., Boos, N., 2007. Temporo-spatial distribution of blood vessels in human lumbar intervertebral discs. Eur. Spine J. https://doi.org/10.1007/s00586-006-0213-x

Nerlich, A.G., Schleicher, E.D., Boos, N., 1997. Immunohistologic markers for age-related changes of human lumbar intervertebral discs. Spine (Phila. Pa. 1976). https://doi.org/10.1097/00007632-199712150-00001

Newell, N., Little, J.P., Christou, A., Adams, M.A., Adam, C.J., Masouros, S.D., 2017. Biomechanics of the human intervertebral disc: A review of testing techniques and results. J. Mech. Behav. Biomed. Mater. https://doi.org/10.1016/j.jmbbm.2017.01.037

O'Connell, G.D., Jacobs, N.T., Sen, S., Vresilovic, E.J., Elliott, D.M., 2011. Axial creep loading and unloaded recovery of the human intervertebral disc and the effect of degeneration. J. Mech. Behav. Biomed. Mater. https://doi.org/10.1016/j.jmbbm.2011.02.002

O'Connell, G.D., Johannessen, W., Vresilovic, E.J., Elliott, D.M., 2007a. Human internal disc strains in axial compression measured noninvasively using magnetic resonance imaging. Spine (Phila. Pa. 1976). https://doi.org/10.1097/BRS.0b013e31815b75fb

O'Connell, G.D., Leach, J.K., Klineberg, E.O., 2015. Tissue Engineering a Biological Repair Strategy for Lumbar Disc Herniation. Biores. Open Access. https://doi.org/10.1089/biores.2015.0034

O'Connell, G.D., Vresilovic, E.J., Elliott, D.M., 2007b. Comparison of animals used in disc research to human lumbar disc geometry. Spine (Phila. Pa. 1976). https://doi.org/10.1097/01.brs.0000253961.40910.c1

Ochia, R.S., Inoue, N., Renner, S.M., Lorenz, E.P., Lim, T.H., Andersson, G.B.J., An, H.S., 2006. Three-dimensional in vivo measurement of lumbar spine segmental motion. Spine (Phila. Pa. 1976). https://doi.org/10.1097/01.brs.0000231435.55842.9e

Oftadeh, R., Connizzo, B.K., Nia, H.T., Ortiz, C., Grodzinsky, A.J., 2018. Biological connective tissues exhibit viscoelastic and poroelastic behavior at different frequency regimes: Application to tendon and skin biophysics. Acta Biomater. https://doi.org/10.1016/j.actbio.2018.01.041

Oshima, H., Ishihara, H., Urban, J.P.G., Tsuji, H., 1993. The use of coccygeal discs to study intervertebral disc metabolism. J. Orthop. Res. https://doi.org/10.1002/jor.1100110304

Padalkar, M. V., Spencer, R.G., Pleshko, N., 2013. Near infrared spectroscopic evaluation of water in hyaline cartilage. Ann. Biomed. Eng. https://doi.org/10.1007/s10439-013-0844-0

Palanca, M., Tozzi, G., Cristofolini, L., 2016. The use of digital image correlation in the biomechanical area: A review. Int. Biomech. https://doi.org/10.1080/23335432.2015.1117395

Parenteau-Bareil, R., Gauvin, R., Berthod, F., 2010. Collagen-based biomaterials for tissue engineering applications. Materials (Basel). https://doi.org/10.3390/ma3031863

Park, W.M., Kim, K., Kim, Y.H., 2015. Changes in range of motion, intradiscal pressure, and facet joint force after intervertebral disc and facet joint degeneration in the cervical spine. J. Mech. Sci. Technol. https://doi.org/10.1007/s12206-015-0633-9

Parkes, M., Cann, P., Jeffers, J., 2017. Real-time observation of fluid flows in tissue during stress relaxation using Raman spectroscopy. J. Biomech. https://doi.org/10.1016/j.jbiomech.2017.06.004

Pattappa, G., Li, Z., Peroglio, M., Wismer, N., Alini, M., Grad, S., 2012. Diversity of intervertebral disc cells: Phenotype and function. J. Anat. https://doi.org/10.1111/j.1469-7580.2012.01521.x

Pearce, R.H., Grimmer, B.J., Adams, M.E., 1987. Degeneration and the chemical composition of the human lumbar intervertebral disc. J. Orthop. Res. https://doi.org/10.1002/jor.1100050206

Peña, J.A., Martínez, M.A., Peña, E., 2011. A formulation to model the nonlinear viscoelastic properties of the vascular tissue. Acta Mech. https://doi.org/10.1007/s00707-010-0378-6

Périé, D., Korda, D., Iatridis, J.C., 2005. Confined compression experiments on bovine nucleus pulposus and annulus fibrosus: Sensitivity of the experiment in the determination of compressive modulus and hydraulic permeability. J. Biomech. https://doi.org/10.1016/j.jbiomech.2004.10.002

Perie, D.S., MacLean, J.J., Owen, J.P., Iatridis, J.C., 2006. Correlating material properties with tissue composition in enzymatically digested bovine annulus fibrosus and nucleus pulposus tissue. Ann. Biomed. Eng. https://doi.org/10.1007/s10439-006-9091-y

Pezzotti, G., Boffelli, M., Miyamori, D., Uemura, T., Marunaka, Y., Zhu, W., Ikegaya, H., 2015. Raman spectroscopy of human skin: looking for a quantitative algorithm to reliably estimate human age. J. Biomed. Opt. https://doi.org/10.1117/1.jbo.20.6.065008

Pfirrmann, C.W.A., Metzdorf, A., Zanetti, M., Hodler, J., Boos, N., 2001. Magnetic resonance classification of lumbar intervertebral disc degeneration. Spine (Phila. Pa. 1976). https://doi.org/10.1097/00007632-200109010-00011

Pollintine, P., Van Tunen, M.S.L.M., Luo, J., Brown, M.D., Dolan, P., Adams, M.A., 2010. Time-dependent compressive deformation of the ageing spine: Relevance to spinal stenosis. Spine (Phila. Pa. 1976). https://doi.org/10.1097/BRS.0b013e3181b0ef26

Pooni, J.S., Hukins, D.W.L., Harris, P.F., Hilton, R.C., Davies, K.E., 1986. Comparison of the structure of human intervertebral discs in the cervical, thoracic and lumbar regions of the spine. Surg. Radiol. Anat. https://doi.org/10.1007/BF02427846

Provenzano, P., Lakes, R., Keenan, T., Vanderby, R., 2001. Nonlinear ligament viscoelasticity. Ann. Biomed. Eng. https://doi.org/10.1114/1.1408926

Przybyla, A.S., Skrzypiec, D., Pollintine, P., Dolan, P., Adams, M.A., 2007. Strength of the cervical spine in compression and bending. Spine (Phila. Pa. 1976). https://doi.org/10.1097/BRS.0b013e318074c40b

Rabinowitz, J.L., Gregg, J.R., Nixon, J.E., Schumacher, H.R., 1979. Lipid composition of the tissues of human knee joints. I. Observations in normal joints (articular cartilage, meniscus, ligaments, synovial fluid, synovium, intra-articular fat pad and bone marrow). Clin. Orthop. Relat. Res. https://doi.org/10.1097/00003086-197909000-00041

Rachev, A., Greenwald, S.E., 2003. Residual strains in conduit arteries. J. Biomech. https://doi.org/10.1016/S0021-9290(02)00444-X

Raj, P.P., 2008. Intervertebral disc: Anatomy-physiology-pathophysiology-treatment. Pain Pract. https://doi.org/10.1111/j.1533-2500.2007.00171.x

Ranjit, S., Dvornikov, A., Stakic, M., Hong, S.H., Levi, M., Evans, R.M., Gratton, E., 2015. Imaging Fibrosis and Separating Collagens using Second Harmonic Generation and Phasor Approach to Fluorescence Lifetime Imaging. Sci. Rep. https://doi.org/10.1038/srep13378

Reddy, G.K., Enwemeka, C.S., 1996. A simplified method for the analysis of hydroxyproline in biological tissues. Clin. Biochem. https://doi.org/10.1016/0009-9120(96)00003-6

Reiser, K.M., Bratton, C., Yankelevich, D.R., Knoesen, A., Rocha-Mendoza, I., Lotz, J., 2007. Quantitative analysis of structural disorder in intervertebral disks using second harmonic generation imaging: comparison with morphometric analysis. J. Biomed. Opt. https://doi.org/10.1117/1.2812631

Reitmaier, S., Shirazi-Adl, A., Bashkuev, M., Wilke, H.J., Gloria, A., Schmidt, H., 2012. In vitro and in silico investigations of disc nucleus replacement. J. R. Soc. Interface. https://doi.org/10.1098/rsif.2012.0016

Riches, P.E., Dhillon, N., Lotz, J., Woods, A.W., McNally, D.S., 2002. The internal mechanics of the intervertebral disc under cyclic loading. J. Biomech. https://doi.org/10.1016/S0021-9290(02)00070-2

Roberts, S., Evans, H., Trivedi, J., Menage, J., 2006. Histology and pathology of the human intervertebral disc, in: Journal of Bone and Joint Surgery - Series A. https://doi.org/10.2106/00004623-200604002-00003

Rodriguez, L.G., Lockett, S.J., Holtom, G.R., 2006. Coherent anti-stokes raman scattering microscopy: A biological review. Cytom. Part A. https://doi.org/10.1002/cyto.a.20299

Rohlmann, A., Zander, T., Schmidt, H., Wilke, H.J., Bergmann, G., 2006. Analysis of the influence of disc degeneration on the mechanical behaviour of a lumbar motion segment using the finite element method. J. Biomech. https://doi.org/10.1016/j.jbiomech.2005.07.026

Roos, Y.H., 1986. Phase Transitions and Unfreezable Water Content of Carrots, Reindeer Meat and White Bread Studied using Differential Scanning Calorimetry. J. Food Sci. https://doi.org/10.1111/j.1365-2621.1986.tb13911.x

Roughley, P.J., 2004. Biology of intervertebral disc aging and degeneration: Involvement of the extracellular matrix. Spine (Phila. Pa. 1976). https://doi.org/10.1097/01.brs.0000146101.53784.b1

Roughley, P.J., Melching, L.I., Heathfield, T.F., Pearce, R.H., Mort, J.S., 2006. The structure and degradation of aggrecan in human intervertebral disc, in: European Spine Journal. https://doi.org/10.1007/s00586-006-0127-7

Samouillan, V., Delaunay, F., Dandurand, J., Merbahi, N., Gardou, J.-P., Yousfi, M., Gandaglia, A., Spina, M., Lacabanne, C., 2011. The Use of Thermal Techniques for the Characterization and Selection of Natural Biomaterials. J. Funct. Biomater. https://doi.org/10.3390/jfb2030230

Sato, K., Kikuchi, S., Yonezawa, T., 1999. In vivo intradiscal pressure measurement in healthy individuals and in patients with ongoing back problems. Spine (Phila. Pa. 1976). https://doi.org/10.1097/00007632-199912010-00008

Schlegel, J.D., Smith, J.A., Schleusener, R.L., 1996. Lumbar motion segment pathology adjacent to thoracolumbar, lumbar, and lumbosacral fusions, in: Spine. https://doi.org/10.1097/00007632-199604150-00013

Schmidt, H., Schilling, C., Reyna, A.L.P., Shirazi-Adl, A., Dreischarf, M., 2016a. Fluid-flow dependent response of intervertebral discs under cyclic loading: On the role of specimen preparation and preconditioning. J. Biomech. https://doi.org/10.1016/j.jbiomech.2015.10.029

Schmidt, H., Shirazi-Adl, A., Schilling, C., Dreischarf, M., 2016b. Preload substantially influences the intervertebral disc stiffness in loading-unloading cycles of compression. J. Biomech. https://doi.org/10.1016/j.jbiomech.2016.05.006

Schroeder, Y., Sivan, S., Wilson, W., Merkher, Y., Huyghe, J.M., Maroudas, A., Baaijens, F.P.T., 2007. Are disc pressure, stress, and osmolarity affected by intra- and extrafibrillar fluid exchange? J. Orthop. Res. https://doi.org/10.1002/jor.20443

Schroeder, Y., Wilson, W., Huyghe, J.M., Baaijens, F.P.T., 2006. Osmoviscoelastic finite element model of the intervertebral disc, in: European Spine Journal. https://doi.org/10.1007/s00586-006-0110-3

Sélard, É., Shirazi-Adl, A., Urban, J.P.G., 2003. Finite element study of nutrient diffusion in the human intervertebral disc. Spine (Phila. Pa. 1976). https://doi.org/10.1097/01.BRS.0000087210.93541.23

Sengupta, D.K., Fan, H., 2014. The basis of mechanical instability in degenerative disc disease: A cadaveric study of abnormal motion versus load distribution. Spine (Phila. Pa. 1976). https://doi.org/10.1097/BRS.0000000000000292

Sharabi, M., Levi-Sasson, A., Wolfson, R., Wade, K.R., Galbusera, F., Benayahu, D., Hans-Joachim, W., Haj-Ali, R., 2019. The Mechanical Role of the Radial Fiber Network Within the Annulus Fibrosus of the Lumbar Intervertebral Disc: A Finite Elements Study. J. Biomech. Eng. https://doi.org/10.1115/1.4041769

Sharma, R.R., Pollock, K., Hubel, A., McKenna, D., 2014. Mesenchymal stem or stromal cells: A review of clinical applications and manufacturing practices. Transfusion. https://doi.org/10.1111/trf.12421

Shoulders, M.D., Raines, R.T., 2009. Collagen Structure and Stability. Annu. Rev. Biochem. https://doi.org/10.1146/annurev.biochem.77.032207.120833

Showalter, B.L., Beckstein, J.C., Martin, J.T., Beattie, E.E., Orías, A.A.E., Schaer, T.P., Vresilovic, E.J., Elliott, D.M., 2012. Comparison of animal discs used in disc research to human lumbar disc: Torsion mechanics and collagen content. Spine (Phila. Pa. 1976). https://doi.org/10.1097/BRS.0b013e31824d911c

Sivan, S., Merkher, Y., Wachtel, E., Ehrlich, S., Maroudas, A., 2006. Correlation of swelling pressure and intrafibrillar water in young and aged human intervertebral discs. J. Orthop. Res. https://doi.org/10.1002/jor.20144

Skaggs, D.L., Weidenbaum, M., Latridis, J.C., Ratcliffe, A., Mow, V.C., 1994. Regional variation in tensile properties and biochemical composition of the human lumbar anulus fibrosus. Spine (Phila. Pa. 1976). https://doi.org/10.1097/00007632-199406000-00002

Smith, L.J., Byers, S., Costi, J.J., Fazzalari, N.L., 2008. Elastic fibers enhance the mechanical integrity of the human lumbar anulus fibrosus in the radial direction. Ann. Biomed. Eng. https://doi.org/10.1007/s10439-007-9421-8

Smith, L.J., Fazzalari, N.L., 2006. Regional variations in the density and arrangement of elastic fibres in the anulus fibrosus of the human lumbar disc. J. Anat. https://doi.org/10.1111/j.1469-7580.2006.00610.x

Solomonow, M., He Zhou, B., Baratta, R. V., Lu, Y., Zhu, M., Harris, M., 2000. Biexponential recovery model of lumbar viscoelastic laxity and reflexive muscular activity after prolonged cyclic loading. Clin. Biomech. https://doi.org/10.1016/S0268-0033(99)00062-5

Spiess, A.N., Neumeyer, N., 2010. An evaluation of R2as an inadequate measure for nonlinear models in pharmacological and biochemical research: A Monte Carlo approach. BMC Pharmacol. https://doi.org/10.1186/1471-2210-10-6

Stevens, R.L., Ewins, R.J.F., Revell, P.A., Muir, H., 1979. Proteoglycans of the intervertebral disc. Homology of structure with laryngeal proteoglycans. Biochem. J. https://doi.org/10.1042/bj1790561

Stokes, I.A.F., Iatridis, J.C., 2004. Mechanical conditions that accelerate intervertebral disc degeneration: Overload versus immobilization. Spine (Phila. Pa. 1976). https://doi.org/10.1097/01.brs.0000146049.52152.da

Stokes, I.A.F., Laible, J.P., Gardner-Morse, M.G., Costi, J.J., Iatridis, J.C., 2011. Refinement of elastic, poroelastic, and osmotic tissue properties of intervertebral disks to analyze behavior in compression. Ann. Biomed. Eng. https://doi.org/10.1007/s10439-010-0140-1

Suh, J.K., Disilvestro, M.R., 1999. Biphasic poroviscoelastic behavior of hydrated biological soft tissue. J. Appl. Mech. Trans. ASME. https://doi.org/10.1115/1.2791079

Talari, A.C.S., Movasaghi, Z., Rehman, S., Rehman, I.U., 2015. Raman spectroscopy of biological tissues. Appl. Spectrosc. Rev. https://doi.org/10.1080/05704928.2014.923902

Tang, R., Samouillan, V., Dandurand, J., Lacabanne, C., Nadal-Wollbold, F., Casas, C., Schmitt, A.-M., 2017. Thermal and vibrational characterization of human skin. J. Therm. Anal. Calorim. https://doi.org/10.1007/s10973-016-5384-z

Tavakoli, J., 2017. Region–media coupling in characterization and modelling of the disc annulus single lamella swelling. Med. Biol. Eng. Comput. https://doi.org/10.1007/s11517-016-1609-3

Téllez Soto, C.A., Medeiros-Neto, L.P., dos Santos, L., Santos, A.B.O., Ferreira, I., Singh, P., Canevari, R.A., Martin, A.A., 2018. Infrared and confocal Raman spectroscopy to differentiate changes in the protein secondary structure in normal and abnormal thyroid tissues. J. Raman Spectrosc. https://doi.org/10.1002/jrs.5370

Thompson, J.P., Pearce, R.H., Schechter, M.T., Adams, M.E., Tsang, I.K., Bishop, P.B., 1990. Preliminary evaluation of a scheme for grading the gross morphology of the human intervertebral disc. Spine (Phila. Pa. 1976).

Troyer, K.L., Puttlitz, C.M., 2011. Human cervical spine ligaments exhibit fully nonlinear viscoelastic behavior. Acta Biomater. https://doi.org/10.1016/j.actbio.2010.09.003

Tsantrizos, A., Ito, K., Aebi, M., Steffen, T., 2005. Internal strains in healthy and degenerated lumbar intervertebral discs. Spine (Phila. Pa. 1976). https://doi.org/10.1097/01.brs.0000181052.56604.30

Twomey, L., Taylor, J., 1985. Age changes in lumbar intervertebral discs. Acta Orthop.

https://doi.org/10.3109/17453678508993043

Unal, M., Akkus, O., 2018. Shortwave-infrared Raman spectroscopic classification of water fractions in articular cartilage ex vivo. J. Biomed. Opt. https://doi.org/10.1117/1.jbo.23.1.015008

Unal, M., Yang, S., Akkus, O., 2014. Molecular spectroscopic identification of the water compartments in bone. Bone. https://doi.org/10.1016/j.bone.2014.07.021

Urban, J.P.G., Holm, S., Maroudas, A., Nachemson, A., 1982. Nutrition of the intervertebral disc. Effect of fluid flow on solute transport. Clin. Orthop. Relat. Res. https://doi.org/10.1097/00003086-198210000-00039

Urban, J.P.G., Holm, S., Maroudas, A., Nachemson, A., 1977. Nutrition of the intervertebral disk. An in vivo study of solute transport. Clin. Orthop. Relat. Res. https://doi.org/10.1097/00003086-197711000-00012

Urban, J.P.G., Maroudas, A., 1981. Swelling of the intervertebral disc in vitro. Connect. Tissue Res. https://doi.org/10.3109/03008208109160234

Urban, J.P.G., Maroudas, A., Bayliss, M.T., Dillon, J., 1979. Swelling pressures of proteoglycans at the concentrations found in cartilaginous tissues. Biorheology. https://doi.org/10.3233/BIR-1979-16609

Urban, J.P.G., McMullin, J.F., 1988. Swelling pressure of the lumbar intervertebral discs: Influence of age, spinal level, composition, and degeneration. Spine (Phila. Pa. 1976). https://doi.org/10.1097/00007632-198802000-00009

Urban, J.P.G., Roberts, S., 2003. Degeneration of the intervertebral disc. Arthritis Res. Ther. https://doi.org/10.1186/ar629

van den Akker, G.G.H., Koenders, M.I., van de Loo, F.A.J., van Lent, P.L.E.M., Blaney Davidson, E., van der Kraan, P.M., 2017. Transcriptional profiling distinguishes inner and outer annulus fibrosus from nucleus pulposus in the bovine intervertebral disc. Eur. Spine J. https://doi.org/10.1007/s00586-017-5150-3

Van der Veen, A.J., Bisschop, A., Mullender, M.G., van Dieën, J.H., 2013. Modelling creep behaviour of the human intervertebral disc. J. Biomech. https://doi.org/10.1016/j.jbiomech.2013.05.026

van der Veen, A.J., Mullender, M., Smit, T.H., Kingma, I., van Dieën, J.H., 2005. Flow-related mechanics of the intervertebral disc: the validity of an in vitro model. Spine (Phila. Pa. 1976). https://doi.org/10.1097/01.brs.0000179306.40309.3a

van der Veen, A.J., Mullender, M.G., Kingma, I., van, J.H., Smit, T.H., 2008. Contribution of verftebral bodies, endplates, and intervertebral discs to the compression creep of spinal motion segments. J. Biomech. https://doi.org/10.1016/j.jbiomech.2008.01.010

van der Veen, A.J., van Dieën, J.H., Nadort, A., Stam, B., Smit, T.H., 2007. Intervertebral disc recovery after dynamic or static loading in vitro: Is there a role for the endplate? J. Biomech. https://doi.org/10.1016/j.jbiomech.2006.10.018

Velísková, P., Bashkuev, M., Shirazi-Adl, A., Schmidt, H., 2018. Computational study of the role of fluid content and flow on the lumbar disc response in cyclic compression: Replication of in vitro and in vivo conditions. J. Biomech. https://doi.org/10.1016/j.jbiomech.2017.10.032

Vergroesen, P.P.A., Emanuel, K.S., Peeters, M., Kingma, I., Smit, T.H., 2018. Are axial intervertebral disc biomechanics determined by osmosis? J. Biomech. https://doi.org/10.1016/j.jbiomech.2017.04.027

Vergroesen, P.P.A., Kingma, I., Emanuel, K.S., Hoogendoorn, R.J.W., Welting, T.J., van Royen, B.J., van Dieën, J.H., Smit, T.H., 2015. Mechanics and biology in intervertebral disc degeneration: A vicious circle. Osteoarthr. Cartil. https://doi.org/10.1016/j.joca.2015.03.028

Vergroesen, P.P.A., van der Veen, A.J., Emanuel, K.S., van Dieën, J.H., Smit, T.H., 2016. The poro-elastic behaviour of the intervertebral disc: A new perspective on diurnal fluid flow. J. Biomech. https://doi.org/10.1016/j.jbiomech.2015.11.041

Vergroesen, P.P.A., Van Der Veen, A.J., Van Royen, B.J., Kingma, I., Smit, T.H., 2014. Intradiscal pressure depends on recent loading and correlates with disc height and compressive stiffness. Eur. Spine J. https://doi.org/10.1007/s00586-014-3450-4

Vernon-roberts, B., Pirie, C.J., 1977. Degenerative changes in the intervertebral discs of the lumbar spine and their sequelae. Rheumatology. https://doi.org/10.1093/rheumatology/16.1.13

Vresilovic, E.J., Johannessen, W., Elliott, D.M., 2006. Disc mechanics with trans-endplate partial nucleotomy are not fully restored following cyclic compressive loading and unloaded recovery. J. Biomech. Eng. https://doi.org/10.1115/1.2354210

Werbner, B., Spack, K., O'Connell, G.D., 2019. Bovine annulus fibrosus hydration affects rate-dependent failure mechanics in tension. J. Biomech. https://doi.org/10.1016/j.jbiomech.2019.04.008

Wilke, H.J., Neef, P., Caimi, M., Hoogland, T., Claes, L.E., 1999. New in vivo measurements of pressures in the intervertebral disc in daily life. Spine (Phila. Pa. 1976). https://doi.org/10.1097/00007632-199904150-00005

Williams, J.R., Natarajan, R.N., Andersson, G.B.J., 2007. Inclusion of regional poroelastic material properties better predicts biomechanical behavior of lumbar discs subjected to dynamic loading. J. Biomech. https://doi.org/10.1016/j.jbiomech.2006.09.022

Wilson, W., Van Donkelaar, C.C., Van Rietbergen, B., Huiskes, R., 2005. A fibril-reinforced poroviscoelastic swelling model for articular cartilage. J. Biomech. https://doi.org/10.1016/j.jbiomech.2004.07.003

Wolthuis, R., van Aken, M., Fountas, K., Robinson, J.S., Bruining, H.A., Puppels, G.J., 2001. Determination of water concentration in brain tissue by Raman spectroscopy. Anal. Chem. https://doi.org/10.1021/ac0101306

Wu, J.J., Eyre, D.R., Slayter, H.S., 1987. Type VI collagen of the intervertebral disc. Biochemical and electron-microscopic characterization of the native protein. Biochem. J. https://doi.org/10.1042/bj2480373

Xu, B., Li, H., Zhang, Y., 2013. Understanding the viscoelastic behavior of collagen matrices through relaxation time distribution spectrum. Biomatter. https://doi.org/10.4161/biom.24651

Yang, B., O'Connell, G.D., 2019. Intervertebral disc swelling maintains strain homeostasis throughout the annulus fibrosus: A finite element analysis of healthy and degenerated discs. Acta Biomater. https://doi.org/10.1016/j.actbio.2019.09.035

Yao, H., Gu, W.Y., 2007. Three-dimensional inhomogeneous triphasic finite-element analysis of physical signals and solute transport in human intervertebral disc under axial compression. J. Biomech. https://doi.org/10.1016/j.jbiomech.2006.10.001

Yu, J., Peter, C., Roberts, S., Urban, J.P.G., 2002. Elastic fibre organization in the intervertebral discs of the bovine tail. J. Anat. https://doi.org/10.1046/j.1469-7580.2002.00111.x

Yu, J., Tirlapur, U., Fairbank, J., Handford, P., Roberts, S., Winlove, P.C., Cui, Z., Urban, J., 2007. Microfibrils, elastin fibres and collagen fibres in the human intervertebral disc and bovine tail disc. J. Anat. https://doi.org/10.1111/j.1469-7580.2007.00707.x

Zhang, Q., Andrew Chan, K.L., Zhang, G., Gillece, T., Senak, L., Moore, D.J., Mendelsohn, R., Flach, C.R., 2011. Raman microspectroscopic and dynamic vapor sorption characterization of hydration in collagen and dermal tissue. Biopolymers. https://doi.org/10.1002/bip.21618

Zhang, Y., Drapeau, S., An, H.S., Markova, D., Lenart, B.A., Anderson, D.G., 2011. Histological features of the degenerating intervertebral disc in a goat disc-injury model. Spine (Phila. Pa. 1976). https://doi.org/10.1097/BRS.0b013e3181f60b39

Zhou, B., Ravindran, S., Ferdous, J., Kidane, A., Sutton, M.A., Shazly, T., 2016. Using digital image correlation to characterize local strains on vascular tissue specimens. J. Vis. Exp. https://doi.org/10.3791/53625

Zhou, M., Bezci, S.E., O'Connell, G.D., 2019. Multiscale composite model of fiber-reinforced tissues with direct representation of sub-tissue properties. Biomech. Model. Mechanobiol. https://doi.org/10.1007/s10237-019-01246-x

Zhu, T., Ai, T., Zhang, W., Li, T., Li, X., 2015. Segmental quantitative MR imaging analysis of diurnal variation of water content in the lumbar intervertebral discs. Korean J. Radiol. https://doi.org/10.3348/kjr.2015.16.1.139

Zhu, W., Mow, V.C., Koob, T.J., Eyre, D.R., 1993. Viscoelastic shear properties of articular cartilage and the effects of glycosidase treatments. J. Orthop. Res. https://doi.org/10.1002/jor.1100110602

Zimmerman, M.C., Vuono-Hawkins, M., Parsons, J.R., Carter, F.M., Gutteling, E., Lee, C.K., Langrana, N.A., 1992. The mechanical properties of the canine lumbar disc and motion segment. Spine (Phila. Pa. 1976). https://doi.org/10.1097/00007632-199202000-00016